Multifunctional fibre metal laminates with improved load bearing capability

Vom Promotionsausschuss der
Technischen Universität Hamburg

zur Erlangung des akademischen Grades

Doktor-Ingenieur (Dr.-Ing.)

genehmigte Dissertation

von
Björn Bosbach

aus
Langenhagen

2018

Vorsitzender des Prüfungsausschusses:	Prof. Dr.-Ing. Benedikt Kriegesmann
Gutachter:	Prof. Dr.-Ing. habil. Bodo Fiedler
	Prof. Dr.-Ing. Wolfgang Hintze
Tag der mündlichen Prüfung:	19.10.2018

Technisch-Wissenschaftliche Schriftenreihe

Herausgeber:

Prof. Dr.-Ing. habil. Bodo Fiedler

Anschrift:

Technische Universität Hamburg
Institut für Kunststoffe und Verbundwerkstoffe
Denickestraße 15
21073 Hamburg

Band 33:

Multifunctional fibre metal laminates with improved load bearing capability

Björn Bosbach

1. Auflage

Hamburg 2018

ISSN 2625-6029

Bibliographische Information der Deutschen Nationalbibliothek:

Die deutsche Nationalbibliothek verzeichnet diese Publikation in der Deutschen Nationalbibliothek; detaillierte Informationen sind im Internet über http://www.dnb.de abrufbar.

Holzhacken ist deshalb so beliebt,
weil man bei dieser Tätigkeit den Erfolg sofort sieht.

Albert Einstein (1879-1955)

Kurzfassung

Um die Lastübertragung einer Bolzenverbindung aus Faser-Kunststoff-Verbunden (FKV) zu erhöhen, ist eine lokale Erhöhung der Laminatdicke erforderlich. Dies führt neben einem höheren Gewicht und Platzbedarf zur sekundären Biegung der Struktur. Darüber hinaus sind diese FKV anfällig für Schäden, wie Schichtablösung oder Zwischenfaserbruch, die z.B. nach einem Schlagschaden entstehen können. Diese Art von Schäden ist visuell schwierig zu erkennen und führt häufig zu einem Versagen des FKV. Die Überwachung von solchen Schäden wäre daher im Betrieb sinnvoll, um die Zuverlässigkeit von Strukturbauteilen zu erhöhen. Zur Verbesserung der mechanischen Eigenschaften werden häufig Fasermetalllaminate (FML) aus dünnen Blechen und FKV verwendet. Die unzureichende Metalloberflächenbehandlung führt jedoch oft zu einer frühen Schichtablösung und einem daraus folgenden Versagen des Verbundes.

Zur Steigerung der mechanischen Eigenschaften sowie der Lebensdauer einer Bolzenverbindung im Vergleich zu herkömmlichen glasfaserverstärkten Kunststoffen (GFK) werden im Rahmen dieser Arbeit multifunktionelle FML mit permeablen und oberflächenbehandelten Metalllagen untersucht. Die Laminate werden im Harzinjektionsverfahren hergestellt. Es zeigt sich, dass die FML ein hohes Potential für strukturelle Anwendungen bieten. Die statisch und zyklisch getesteten Augen- und Bolzenverbindungen sowie die Restdruckfestigkeit nach einem Schlagschaden können im Vergleich zu einem herkömmlichen GFK deutlich gesteigert werden. Die Vorbehandlung der Metalllagen durch chemisches Ätzen führt zu einer dreidimensionalen mechanischen Verankerungsstruktur mit einer stark verbesserten Lagenanbindung zwischen der Metalloberfläche und der Matrix. Die Bruchflächen zeigen, dass die adhäsive Bindung zwischen der strukturierten Oberfläche des Aluminiums und der Matrix unter verschiedenen Lastfällen unbeschädigt bleibt. Zusätzlich kann für FML durch einen neuen Ansatz gezeigt werden, dass Schäden durch einfache Kapazitätsmessung zwischen den einzelnen Metalllagen ohne die Notwendigkeit zusätzlicher Sensoren in-situ detektiert werden können.

Abstract

The relative weakness of the load bearing capability under static and fatigue loading rules the design of fibre reinforced polymer (FRP) structures. Increasing the bearing capability needs a locally increased laminate thickness, which results in higher weight and constructed space as well as secondary bending of the structure. Furthermore, these composites are susceptible to inherent damages, e.g. after an impact, resulting in delamination and inter-fibre failures. Such damages are difficult to detect and often lead to catastrophic failure of the composite. In-situ monitoring of damage development is a promising approach to increase the reliability and durability of structural components. Improving the mechanical properties resulted in hybrid composites of thin metal sheets and FRPs. However, insufficient metal surface treatment often leads to early delamination and failure of the composite.

The subject of this work is the investigation of multifunctional fibre metal laminates (FML) with permeable and surface treated metal plies to improve the mechanical performance and bolted joint fatigue life compared to conventional glass fibre reinforced polymers. The laminates are manufactured by resin transfer moulding. As result the FMLs show a high potential for structural applications leading to drastically increased mechanical properties for static and fatigue pin- and bolt-bearing, and compression after impact in comparison to a conventional GFRP laminate. The pre-treatment of the metal plies by chemical etching leads to a three-dimensional mechanical interlocking surface structure with highly improved inter-ply bonding between the metal surface and the resin. The fracture surface demonstrates that the adhesive bond between the nanoscale sculptured surface structure of the aluminium and the matrix remains intact under various loading conditions. Furthermore, a new approach of health monitoring of FMLs is investigated. Damages can be detected in-situ by standard capacitance measurements between the single metal plies, without the need of additional sensors.

Table of Content

List of Abbreviations

Symbol	Description
AA	Aluminium Alloy
AE	Acoustic Emission
Al / Al*	Aluminium / Aluminium (nanoscale sculpured)
CAI	Compression After Impact
CC	Compliance Calibration
CFRP	Carbon Fibre Reinforced Polymer
DCB	Double Cantilever Beam
DNS	Double-Notched Shear
DSC	Differential Scanning Calorimetry
ENF	End-Notched Flexure
FML	Fibre Metal Laminate
FRP	Fibre Reinforced Polymer
GF	Glass Fibre
GFRP	Glass Fibre Reinforced Polymer
GLARE	Glass Laminate Aluminium Reinforced Epoxy
IFF	Inter-Fibre Failure
ILSS	Inter-Laminar Shear Strength
NCF	Non-Crimp Fabric
PES	Polyether Sulfones
PTFE	Polytetrafluoroethylene
RTM	Resin Transfer Moulding
SEM	Scanning Electron Microscope
SHM	Structural Health Monitoring
UD	Unidirectional
WMF	Woven Metallic Fabric

1 Introduction

Fibre reinforced polymers (FRP) are extensively used in various industries such as aircraft, wind power and the automotive industry. Here, they are exposed to a variety of operating conditions and mechanical loads, especially fatigue loading.

One of the biggest challenges in the field of FRPs is to adequately transmit the mechanical loads into the FRP structure. For structural components this is usually done by using bolted joints [1–4]. In general, the load capacity of a bolted joint is enhanced by locally increasing the laminate thickness and corresponding ply drop off to the nominal thickness. However, this procedure increases the weight and also causes secondary bending of the structure due to the associated eccentricities [5].

Furthermore, these high performance structural composites are constructed of fibre layers that are susceptible to inherent damages, such as delamination or matrix cracking [6]. These types of damages, which may occur during the manufacturing process as well as in service after e.g. an impact, can deteriorate the mechanical properties [6–11]. Such damages are difficult to detect and often lead to catastrophic failure of the composite [7].

In-situ monitoring of damage development could be a useful tool to increase the reliability and durability of structural components. Hence, in recent years, structural health monitoring (SHM) of composites has gained importance and different types of sensors for damage detection have been developed [12–19].

For the failure mechanisms and the performance of FRP, the choice of fibre and matrix types, the lay-up, the properties of the composite constituents and in particular the inter-ply bonding, which is affected by surface pre-treatment of the constituents, play an important role [7].

1.1 Motivation

A need for improved material properties resulted in development of hybrid composites of stacked thin metal sheets and FRPs. Most of these FMLs are manufactured by prepreg-autoclave technology [5,8,11,20]. The manufacturing of FMLs with the single-stage resin transfer moulding (RTM)-process is mainly unexplored. FMLs combine the superior fatigue and fracture characteristics of FRPs with the ductility and durability offered by many metals. In fact, it has been shown that the interaction between both materials results in a redistribution of stresses at the crack tip, delaying crack growths as well as positively affecting both fracture mechanical behaviour and fatigue life of the components [21–23]. Under impact loading, FMLs perform excellently because they are less susceptible to the formation of large areas of internal damages compared to conventional composite laminates. After a low-velocity impact the presence of a metal sheet in the outer layer of a FML offers certain ductility and its plastic deformation provides permanent damage that increases detectability [6,9,24,25]. Vlot [8] reported that impact damages in aircrafts are usually located around the doors, in the cargo compartments, on the nose or at the tail of the aircraft.

The most common hybrid composite is GLARE (glass laminate aluminium reinforced epoxy), which is used for the upper fuselage skin structures of the Airbus A380. These areas are particularly stressed by low-frequency cyclic axial fatigue loads. This FML consists of GFRP and thin rolled aluminium alloys with a thickness range between 0.2 mm and 0.5 mm resulting in high fatigue, impact, corrosion, and flame resistance [11,26]. Furthermore, thin metal plies are widely used in e.g. the aerospace industry to protect the aeroplane against lightning strikes [27]. Locally embedding of metal sheets into the composite in areas of bolted joints is proven to be an effective method of increasing the joint efficiency. At the same time it avoids laminate thickening and provides high bearing and shear capabilities [5,28]. The bearing performance increases almost linearly with increasing the metal volume fraction [5].

However, the inter-laminar strength of the metal-matrix interface in conventional laminates is still limited leading to delamination between the metal and the adjacent composite layer [29–32]. Increasing the inter-ply bonding between the metal and the matrix improves the resistance to crack growth at an inter-laminar interface and prevents early delamination, resulting in higher mechanical performance.

1.2 Objectives

Resulting from the challenges pointed out above, in this work a multifunctional hybrid composite of glass fibre reinforced polymer (GFRP) and aluminium (Al) plies is being developed aim to

1. Reach maximum inter-laminar properties to prevent adhesive failure of the interfacial metal-matrix bond.
2. Show the potential for structural applications by reaching high fatigue bearing capability as well as high resistance under impact and CAI loading in comparison to a conventional GFRP laminate.
3. Combine mechanical and electrical tests in order to present the SHM potential of FMLs by detecting damages without additional sensors.

Partial results of the present work have been published in journal articles and proceedings [33–40].

2 Theoretical and scientific background

2.1 Structure and properties of fibre metal laminates

2.1.1 Glass fibre

Glass fibres (GF) are widely-used as reinforcement in high-performance composite applications due to the combination of good properties and low cost. The major material of GF is silica (SiO_2), mixed with other oxides. The typical manufacturing process is melt spinning, usually resulting in GF diameters in the range 10-20 µm in composite applications. The atoms form a three-dimensional network but with amorphous structure and without orientation, which leads to isotropic properties of the GF. The fracture mechanic of GFs behaves brittle. A failure is caused by the most critical defect in the volume. The properties are characterised by corrosion resistance, excellent tolerance to high temperature, radar transparency, insulating against electricity and a good compatibility with metallic materials. In FRPs, mostly E-glass fibres are used [41–43]. Table 2.1 shows the material properties of an E-glass fibre.

Table 2.1: Properties of an E-glass fibre [44].

Properties (units)	E-glass fibre
E-Modulus $E_{\|\|,\perp}$ / GPa	~ 73
Tensile strength $R_{m\|\|,\perp}$ / MPa	~ 2400
Strain at failure ε_F / %	~ 4.8
Coeff. of thermal exp. α_T / 10^{-6}·K^{-1}	~ 5.0
Density ρ / g/cm^3	~ 2.6
Dielectric constant ε_0	~ 6.4 - 6.7

2.1.2 Metal alloys

A metal is a solid material that is typically isotropic with good electrical and thermal conductivity. The deformation behaviour of metals under loading is initially reversible elastic until reaching the offset yield strength and afterwards ductile (irreversible plastic). Due to the tightly packed crystal lattice of the metallic structure most metals have a high density (e.g. stainless steel ~ 7.8 - 8.0 g/cm^3) [45]. In the industry, for structural parts metal alloys are mostly used due to e.g. increased mechanical properties and corrosion resistance compared to pure metals. One example is the aluminium alloy AA2024-T3 (AlCuMg2), which is used for most types of GLARE [26,46,47]. An aluminium alloy is formed by adding individual elements such as silicon (Si), iron (Fe), copper (Cu), manganese (Mn), magnesium (Mg), chromium (Cr), zinc (Zn) and titanium (Ti) [48,49]. Silicon provides good resistance against corrosion. Copper and manganese increase the strength. Magnesium increases the strength and hardness as well as the corrosion resistance. Zinc also increases the strength and hardness. The post-processing of the alloy by precipitation hardening (e.g. T1-T6) significantly increases the strength. Table 2.2 shows the material properties of AA2024, AA5754, and AA6082.

Table 2.2: Properties of aluminium alloys [48,50].

Properties (units)	AA2024	AA5754	AA6082
E-Modulus E / GPa	~ 73	~ 70	~ 70
Yield strength $R_{p0.2}$ / MPa	~ 60 - 290	~ 80 - 180	~ 50 - 260
Tensile strength R_m / MPa	~ 180 - 440	~ 180 - 260	~ 110 - 320
Strain at failure ε_F / %	~ 2 - 12	~ 3 - 15	~ 6 - 15
Coeff. of thermal exp. α_T / 10^{-6}·K^{-1}	~ 24	~ 24	~ 24
Density ρ / g/cm^3	~ 2.77	~ 2.66	~ 2.70

The main responsibilities of Al plies in FMLs are [25]: (1) stable extension before fracture, (2) providing high residual strength, (3) good fatigue performance, (4) yielding at high loads, (5) short crack performance, and (6) high blunt notch strength (defined as the strength of a structure containing a hole [46]).

The higher stiffness and strength of 7000 grade Al plies, e.g. AA7475-T6, which is used for GLARE leads to smaller permanent deflection but the brittle nature provides less energy absorption and favourable damage resistance compared to AA2024-T3 based GLARE [51].

2.1.3 Thermoset polymer matrix

For the matrix system the thermoset epoxy is often used for structural applications in various industries such as aircraft, wind power and the automotive industry. It is characterised by its good adhesion and corrosion protection, chemical resistance, good toughness and heat resistance. Furthermore, in comparison to other thermosets it has a high strength and fatigue resistance as well as good electrically insulating properties. Epoxy resin systems are composed of resin and hardener molecules that react with each other, even at low temperatures. The reaction mechanism is a polyaddition in which two functional groups of adjacent monomer units combine [43,52].

2.1.4 Reinforcement - matrix interaction

The inter-ply bonding between the reinforcement constituents, which is affected by the surface pre-treatment, plays an important role for the failure mechanisms of a composite [7]. Increasing the adhesive bonding between the constituent and the matrix improves the resistance to crack growth and prevents early delamination, resulting in higher mechanical performance [7]. Coupling agents such as silane are often used to increase the interfacial adhesion of the fibre-matrix bond [53]. Allaer et al. [54] investigated the in-plane mechanical properties of unidirectional (UD) stainless steel fibre-epoxy laminates under quasi-static tensile, compression and shear loading experimentally. Fracture surfaces showed no presence of matrix adherents on the steel fibres, indicating low fibre-matrix interfacial strength. Callens et al. [55] studied the influence of silanisation as adhesion promoter in UD and cross-ply stainless steel fibre-epoxy composites. Silanisation led to greater toughness, higher strain-to-failure and dissipated energy values as well as increased interfacial strength, which delayed the formation of matrix cracks and hindered their growth, compared to conventional laminates.

However, the fracture surface showed a mixed-mode of adhesive and cohesive failure, although adhesion predominated.

2.1.5 Surface treatment of aluminium alloys – state of the art

Conventional methods to improve the adhesion of aluminium alloys (AA) to polymers involve chemical surface structuring techniques with acids, e.g. chromic, or alkalines like sodium hydroxide [56]. In general, chemical etching processes are used to replace the weakly and naturally formed surface oxide with a uniform and solid oxide layer [57,58]. In addition, these processes clean and activate the surface by material removal and influence the micro and macro roughness, often resulting in preferential dissolution of the grain boundaries, which leads to a weakening of the near-surface microstructure. Anodising is conventionally conducted in acidic electrolytes, e.g. chromic or phosphoric [59] forming oxide layers on the Al surface with a thickness up to several micrometres and significantly increased surface roughness [60]. These oxide layers tend to show effects of crazing under thermal and mechanical stress, which weakens the mechanical stability of the oxide layer [61]. Critchlow et al. [62] summarised numerous surface pre-treatments for AA to enhance the interfacial metal-matrix bond. A common surface pre-treatment in the aerospace industry to improve the interfacial bonding of e.g. AA2024-T3-epoxy involves the process steps: 1. alkali degreasing, 2. pickling in chromic-sulfuric acid, 3. chromic acid anodising, and 4. priming with Cytec BR-127 (modified epoxy phonolic primer for corrosion-inhibiting) [6].

2.1.6 Failure mechanisms of FRP subjected to compression

The failure mechanisms of FRPs are divided into three modes [63]; at the microscopic level (1) fibre breakage and (2) inter-fibre failure (IFF), and on the macroscopic level mainly (3) delamination (large-area separation of two individual layers). Under longitudinal tension, the primary failure is dependent on the fracture strain of the fibre, respectively of the matrix.

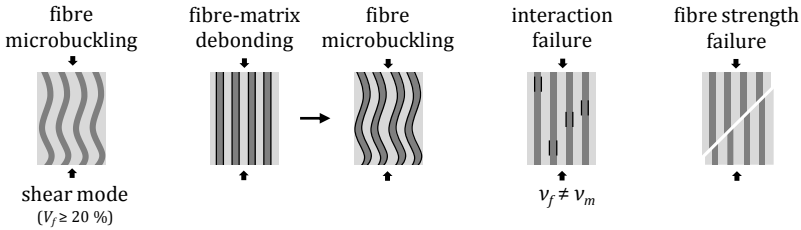

Figure 2.1: Failure modes for unidirectional composites under compression according to [64].

In contrast, failure under longitudinal compression occurs due to loss of stability of the fibre [64] (Figure 2.1); (1) fibre microbuckling in the shear mode ($V_f \geq 20$ %), (2) fibre-matrix debonding followed by microbuckling, (3) interaction failure due to the different poisson ratio ($\nu_f \neq \nu_m$) of the fibre and matrix, and (4) fibre strength failure.

2.2 Adhesion and cohesion

The bonding forces within an adhesive are distinguished as the strength of the boundary layer (adhesion forces) and the strength of the adhesive layer (cohesion forces). Since the adhesion processes are based on sorption phenomena, their consideration is of importance. Jenckel et al. [65] studied the adsorption of macromolecules on the surface (schematically in Figure 2.2). It was shown, that only certain segments of the chain molecules are bound by adsorption forces at the interface. Applied to adhesive layers, this means that the other parts of the chains initially extend into the liquid adhesive. The chains have the form of loops without sorption bonds. Upon curing, these non-adsorbed chain regions shape under the formation of intermolecular forces the solid adhesive layer.

Figure 2.2: Adsorption of macromolecules on the surface (schematic) according to [65].

The adhesion determines the efficacy of load transfer from a stiff component (e.g. high modulus fibre or metal) to the more ductile matrix. The adhesion is affected by many variables, such as physical and chemical forces, absorption or mechanical interlocking. The effective connection of the adhesive layer and the component (adhesion forces) is among other aspects based on the penetration of the liquid adhesive into the pores, capillaries or undercuts, in which the adhesive layer "anchored" during the curing (Figure 2.3a). Smooth, slightly roughened surfaces or small bond energies between the component and the adhesive layer often leads to an adhesive failure (Figure 2.3a) or a mixed-mode failure of adhesion and cohesion (Figure 2.3b). Therefore, the surface of fibres or metals should be pre-treated to increase the adhesive bonding. In cases where the surface pre-treatment process results in high adhesion (adhesive forces > cohesive forces), the cohesive strength is the decisive criterion for designing the adhesive bond (Figure 2.3c). The cohesion (inner strength) is the action of attractive forces between atoms and molecules within the substance. Defects in the adhesive layers reduce the strength level by the formation of internal stresses and may cause cracks under loading [66].

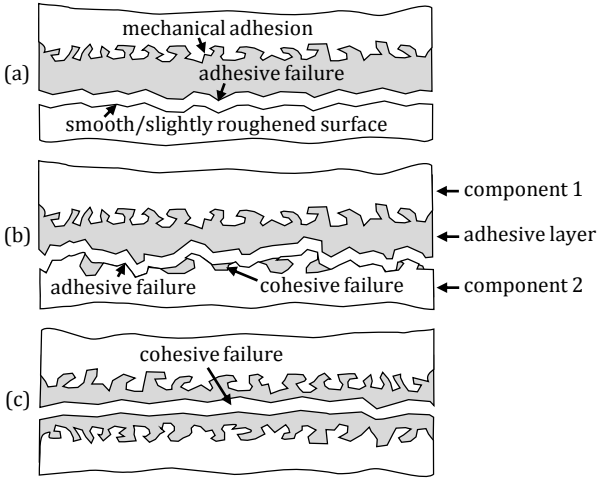

Figure 2.3: Schematic: (a) Mechanical adhesion and adhesive failure between two components; (b) Mixed-mode of adhesive and cohesive failure; (c) Cohesive failure.

2.3 Mechanical properties

2.3.1 Inter-laminar shear strength

Delamination is one of the major degradation mechanisms in FRP laminates and occurs due to low inter-laminar strength. Different experimental testing methods have been established to estimate the inter-laminar shear strength (ILSS). In general, the ILSS is defined as the shear strength at rupture, where the plane of fracture is located between the layers along the reinforcement of the composite structure. Matsuyamab et al. [67] measured the inter-laminar shear strength of carbon fibre-reinforced carbon matrix composites using three-point bending of a short beam [68] and double-notch shear (DNS) testing [69]. DNS testing results in a well-defined single shear failure and leads into a consistent and conservative inter-laminar shear strength. Chiao et al. [70] announced the difficulty in cutting the notches accurately to the prescribed depth of DNS specimens. Shokrieh et al. [71] characterised the inter-laminar shear strength of UD graphite-epoxy under static and fatigue compression and therefore verified the DNS testing [69], using the proper specimen geometry, as simple and reliable testing method. Inducing pure in-plane shear of a DNS specimen requires a 90°-loading direction, which leads to a tensile matrix failure prior to inter-laminar shear failure under tension. The matrix strength in compression is higher than in tension. Therefore, compression is suggested. To prevent out-of-plane deformation of the specimen a supporting jig can be used. According to ASTM D-3846-08 [69], failure in shear of the DNS specimen occurs between the two notches being machined halfway through the specimen thickness. In contrast to ASTM D-2344, it allows reliable testing of parallel and non-parallel FRP specimens.

2.3.2 Inter-laminar fracture toughness

The resistance of an inter-laminar interface to crack growth is evaluated by determining the fracture toughness. Standard testing methods of double cantilever beam (DCB) and end notched flexure (ENF) are used to determine the critical energy release rates G_{Ic} (opening mode I) and G_{IIc} (shear mode II).

Different experimental studies have indicated that the most conservative toughness values are produced by testing UD $[0]_n$ laminates in which the delamination propagates along the fibre direction between the plies. The 0°-plies in these laminates often produce fibre bridging, which influences the toughness values [72–75]. It was shown, that a crack in laminates with multidirectional plies may have a tendency to propagate through neighbouring plies as well [76–80]. Bridging mechanisms increase the toughness as the crack grows, leading to a crack resistance curve (*R*-curve) [72–75,81]. Materials with rising *R*-curve behaviour can be characterised by the value at the initiation of the crack growth [82]. However, the initiation toughness considers only the onset of crack growth, without information on the shape of the *R*-curve. Hence, the *R*-curve diagram (e.g. energy release rate vs. crack size) is required.

Laminates with a delamination crack off the mid plane, which is common in structural components, lead to a mix of fracture modes at the crack tip. The resulting energy release rate G is a superposition of mode I and mode II loading. The corresponding proportion of the respective loading can be determined by the mode-mixity G_I/G and G_{II}/G (where $G = G_I + G_{II}$) [83–86]. Bieniaś et al. [87] studied the inter-laminar fracture toughness of multidirectional, asymmetrical, nonhomogeneous FMLs by the ENF method. The laminates with a crack interface of an Al ply (thickness: 0.5 mm) and 0°-FRP layer resulted in significant predominance of fracture mode II. Calculating the energy release rates of all laminates by the enhanced beam theory [86] and compliance calibration method [88] led to similar results.

Nairn [89] evaluated the influence of residual stresses on the mode I delamination toughness of FRPs. A laminate containing layers of different thermal expansion coefficients that is cured at high temperature and afterwards rapidly cooled to room temperature develops residual stresses. This would lead to an initial curvature of the laminate. Thus, the thermally induced curvature contributes to delamination toughness by doing external work as the crack grows. If the thermal stresses are ignored, the calculated fracture toughness will be an apparent toughness, which is larger than the true toughness.

2.3.3 Bearing response

Mechanical fastening with bolted joints is still one of the main currently used methods to join composite components e.g. in the aerospace industry, resulting in advantages of easy inspection and disassembly. The laminate lay-up and the joint geometries are important to reach true bearing failure and preventing failures such as shear-out, cleavage, and net-tension. The bearing strength σ^{br}, often defined by 2 % hole expansion [90], is mainly a compressive strength of the constituents.

The bearing loading leads to complex stress mechanics at the bolt loaded holes [91]. Contrary to metals, which show high stress peaks by localised plastic flow, FRP reduces the local stiffness by IFFs and delamination. In fact the stress peaks are reduced and the stress extensively rearranged. In addition kink-band occurs in the fibres lying in load direction. Simultaneously the hole expands. The bearing failure can be described as good-natured due to the fact that no joint part separation takes place. Due to their high stiffness, the 0°-fibres take most of the compression. In fact of the cylindrical bolt shape the 0°-fibres are only ideal oriented in the crown centre of the bolt. The circular shape of the bolt causes force components from the bolt to also appear angular to the direction of loading on the laminate. Hence, to prevent shear-out, cleavage failure, and net-tension, fibres in 90°- and ±45°-direction are necessary.

According to experiments [20,42], the best results of FRPs under bearing loading are obtained with 50 % of fibres in 0°-direction, 40 % of fibres in ±45°-direction and 10 % of fibres in 90°-direction (50/40/10)-(0,±45,90). This lay-up is called aircraft laminate due to the fact that it is widely used in the aerospace industry with respect to structure components, which require high bearing strength. The fit between the bolt and the hole has a significant influence on the bearing performance [92,93]. A transition fit resulted in up to 20 % higher bearing strength compared to a clearance fit [92].

Reaching full bearing strength requires a certain minimum value of the edge distance to diameter (e/d) and width to diameter (w/d) ratio in terms of joint geometries.

For GFRP, the recommended minimum e/d and w/d ratios are often 3 and 4, respectively, concerning pin-loaded bearing [94]. These increase further up to 6.5 and 10, respectively with increasing clamping torque (e.g. 30 Nm) [94]. Caprino et al. [3] indicated that for true pin-loaded bearing failure of FMLs the minimum e/d and w/d ratios are often 1.6 and 2, respectively. Wu et al. [95] specified for full bearing strength of FMLs an e/d and w/d ratio of 3, respectively 4. It has been found that increasing the clamping torque positively affects the bearing performance of a bolted joint, amongst others due to the effect of lateral pressure on the laminate, which prevents lateral expansion under compression and hence early delamination [1,94,96–98]. Additionally, the application of washers increases the joint strength [97–99] resulting in an optimal washer diameter of $D_{washer} = 2 \cdot d_{bolt}$ [100].

A further important aspect for the performance of bolted joints are the effects of drilling on the FRP [101–108]. Typical damage modes subjected to drilling are e.g. fibre pull-out, intra-laminar cracks, matrix cratering, thermal alterations, and delamination affecting the laminate quality and mechanical properties. The type of damage induced in the laminate after drilling is significantly influenced on the feed speed [103]. Davim et al. [109] evaluated the influence of cutting parameters (cutting and feed speed) on the size of the delamination and the surface roughness of GFRPs. Increasing the feed speed resulted in increasing delamination and surface roughness, while increasing the cutting speed led to increasing delamination but decreasing surface roughness for the composite materials. For industrial application, an optimum ratio of the cutting parameters must be chosen to obtain a compromise between laminate quality, mechanical properties, and productivity [101].

The mechanical behaviour of bolted joints has been comprehensively studied in the past [1–4,96,110]. Usually the loading capacity of a bolt connection is enhanced by locally increasing the laminate thickness (Figure 2.4a). An alternative to locally increasing the laminate thickness is the replacement of the less important 90°- and ±45°-layers using metal plies (Figure 2.4b), resulting in constant laminate thickness and improved bearing and shear capabilities [5,20,42]. The metal plies are stepped inserted in

terms of FRP ply-substitution into the laminate along the length of the connecting to avoid an abrupt change in stiffness. This process starts in the following order. First, locally replacing the weak 90°-layers. If this is not enough also the ±45°-layers and possibly even the 0°-layers. The inserted metal plies serve two other important functions. Due to their relatively high stiffness, the metal plies take high dynamic loads and distribute the local pressure forces extensively in wide laminate areas. Furthermore, stress peaks can be reduced and rearranged. The greater the strength of the metal plies, the less layers have to be inserted [42].

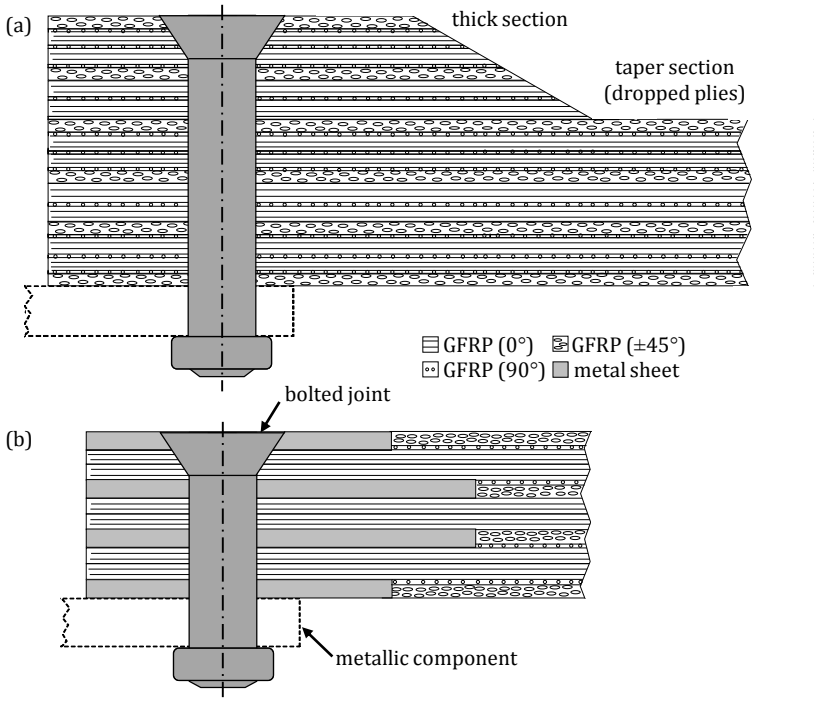

Figure 2.4: Load introduction according to [42]: (a) Enhancement the load capacity of the joint by conventional increasing the laminate thickness (FRP); (b) Enhancement the load capacity of the joint with constant laminate thickness by locally embedding of metal sheets (FML).

The bearing response is mainly researched in FMLs containing carbon fibre reinforced polymer (CFRP) and thin plain metal sheets. Fink et. al [5] performed a hybrid CFRP-titanium composite with a metal volume fraction of 16 % - 50 %. It was shown that the local hybridisation increases the load capability of bolted joints. Both et al. [28] compared the results of pure CFRP laminates with CFRP-titanium and CFRP-steel laminates using finite element analysis as well as experiments. The absolute bearing strengths increased significantly by substituting single CFRP-plies by thin metal sheets. Kolesnikov et al. [20] and Camanho et al. [111] investigated a CFRP-titanium hybrid laminate for improving composite bolted joints. Caprino et al. [3] studied the pin- and bolt- bearing response of GFRP-Al laminates. Matsuzaki et al. [112] investigated the performance of GFRP-Al single lap joints using a bolted and co-cured hybrid joining method. Both [113] tested the bearing strength of CFRP, CFRP-titanium and CFRP-steel laminates under fatigue loading. Under the same level of loading and numbers of cycles the pure CFRP laminate had a significantly higher hole expansion compared to the hybrid composites. Kelly [114] studied the static strength and fatigue life of bonded/bolted CFRP laminates using single-lap joints.

2.4 Structural health monitoring

Most of the FRPs for structural applications are designed for high load levels and a very long lifetime. To monitor the fatigue life and the degradation of the mechanical properties, SHM has gained importance and different types of methods have been developed [12–17]. SHM is based on non-destructive testing of components and provides real-time monitoring of its condition in terms of damage detection. Most of these methods need additional sensors or a modified system to monitor damages in the structure. Acoustic emission (AE) monitors in real time the occurrence and growth of damages by a piezo transducer that is located on the material surface [115]. Gungor and Bakis [116] detected damages in glass-epoxy composite laminates with electrically tailored conductive nanofiller.

Todoroki et al. [117] studied the relations of CF-epoxy composites between the electrical resistance change and the delamination crack length by conducting mode I and II tests, achieving good results for health monitoring.

Peairs et al. [118] monitored damages in bolted joints and composite structures using the impedance-based SHM technique with surface-bonded piezoelectric transducers. Todoroki et al. [119] presented a strain measurement system utilising the electric capacitance change of steel wire reinforced tires. Increasing the load caused an increase of the electrical capacitance, which changed the frequency of the oscillator circuit and consequently enabled to measure the strain of the tire wirelessly. Since this method does not need additional sensors, the stress and deformation field of the tire is not disturbed.

Non-destructive testing methods of adhesive bonded metal to metal joints include e.g. surface impedance measurements, AE, radiography, pulse-echo technique, thermal inspection methods, and the capacitance measurement [18,19]. Measuring the capacitance change has been studied with some success since the early days of metal bonding on small bonded joints [18]. The capacitance (C) is a function of the dielectric constant ($\varepsilon_0 \sim 8.854 \cdot 10^{-12}$ F·m^{-1}), relative static permittivity (ε_r), surface area of overlap of two plates (A), and distance between the plates (d). The capacitance is calculated as follows:

$$C = \varepsilon_0 \cdot \varepsilon_r \cdot A/d$$

Increasing the dielectric constant or the surface area and decreasing the distance between the metal plates leads to a higher capacitance. For larger bonded metal joints, this method might not be very effective as there is only a change of the capacity of the entire bonded area [18].

3 Manufacturing procedures

3.1 Materials

3.1.1 Glass fibres

The used E-glass fibres (with silane sizing as adhesion promoter) are non-crimp fabrics (NCF) with different orientation and mass per unit area (q_F):

1. q_F = 600 g/m²; 528 g/m² (0°-direction), q_F = 54 g/m² (90°-direction), q_F = 18 g/m² PES weft [$0^{90\%}$,$90^{10\%}$] (R&G Faserverbundwerkstoffe GmbH)
2. q_F = 500 g/m² (0°-direction), q_F = 2 g/m² GF weft (Gurit GmbH)
3. q_F = 250 g/m² (90°-direction), q_F = 2 g/m² GF weft (Gurit GmbH)
4. q_F = 430 g/m² (±45°-direction), q_F = 6 g/m² PES weft (R&G Faserverbundwerkstoffe GmbH)

The inter-laminar properties (Chapter 5.1) of the FMLs (metal-metal interface) are determined using the GF NCF (q_F = 600 g/m²) with ~ 90 % of 0°-fibres and ~ 10 % of 90°-fibres [$0^{90\%}$,$90^{10\%}$]. However, this GF NCF does not allow substitution of the 90°-layer. Hence, the subsequent tests (Chapter 5.3-5.6) are conducted using the UD GF NCF (q_F = 500 g/m²).

3.1.2 Metal plies

Different types of permeable and plain Al-stainless steel (St) plies are used (Figure 3.1). The untreated metal plies are cleaned with aceton before being placed in the RTM mould. The pre-treated metal plies undergo a chemical nanoscale sculpturing process [120] being described in detail in chapter 3.1.3. Both the perforated and the plain Al sheets have an initial thickness of 1 mm. After the nanoscale sculpturing the Al sheets result in a thickness of ~ 0.9 mm (AA5754) and ~ 0.65-0.70 mm (AA6082-T6). The permeable metal plies are positioned without specific alignment of the holes or mesh to each other. The different volume fractions of a single ply are adjusted by changing e.g. the mesh size and the wire diameter.

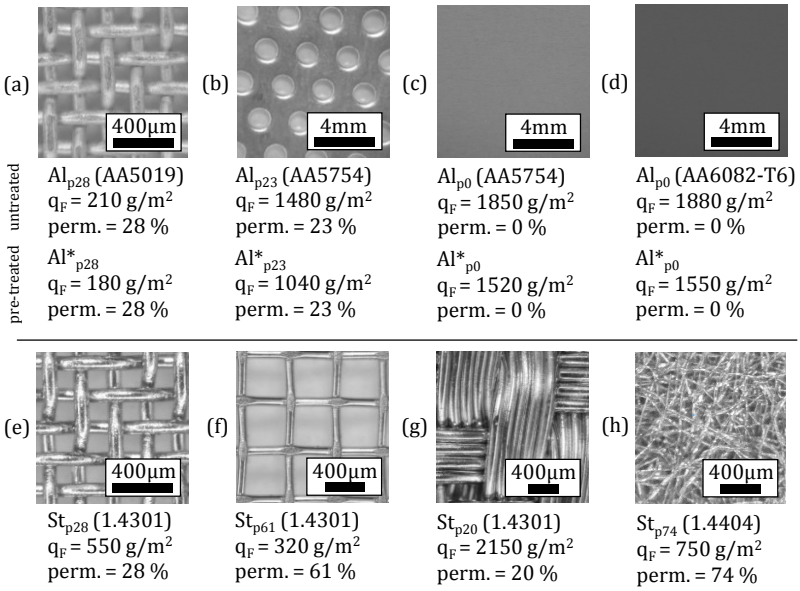

( ): cleaned with aceton; ( )*: nanoscale sculptured; p/perm.: permeability metal ply; St: stainless steel; Al: aluminium

Figure 3.1: Structure, mass per unit area, and permeability of the used metal plies: (a) Al_{p28}/Al^*_{p28} (AA5019); (b) Al_{p23}/Al^*_{p23} (AA5754); (c) Al_{p0}/Al^*_{p0} (AA5754); (d) Al_{p0}/Al^*_{p0} (AA6082-T6); (e) St_{p28} (1.4301); (f) St_{p61} (1.4301); (g) St_{p20} (1.4301); (h) St_{p74} (1.4404).

The woven metallic fabrics (WMF) e.g. Al_{28} consist of 72 % AA5019 for a single ply resulting in a permeability of 28 %. The perforated Al sheets exhibit a hexagonally arranged circular hole pattern with a hole diameter of 1.5 mm and a hole to hole distance of 3 mm.

3.1.3 Metal surface treatment (nanoscale sculpturing process)

Avoiding early crack initiation at the metal-matrix interface under the different loading conditions requires a pre-treatment of the Al surface to increase the interfacial metal-matrix bond. Hence, the Al plies are double-side pre-treated by nanoscale sculpturing (provided by the Chair for Functional Nanomaterials, Faculty of Engineering, Christian-Albrechts-University of Kiel) [120,121] before the FMLs are manufactured by RTM. Four different Al plies are used for the surface treatment: Al fibre fabric (AA5019), perforated Al sheets (AA5754), and plain Al sheets (AA5754

and AA6082). Prior to the nanoscale sculpturing process the Al plies are degreased in acetone and air-dried. Figure 3.2 shows the scanning electron microscope (SEM) images of the different surface structured Al plies. During the process [120], very thin oxide layers are formed and subsequently dissolved in a controlled manner. The slowest-oxidising grains and crystallographic lattice planes in Al are emphasised resulting in the cubical hook-like surface structures in the dimension range of tens of nanometres up to several micrometres with almost perfectly flat sides without any preferential grain boundary dissolution. In fact, the most chemically and mechanically stable surface is created, with a natural oxide coverage and homogeneously structure on the whole Al surface. Depending on the grain orientation, the cubes are inclined to each other. In combination with e.g. polymers it leads to a three-dimensional mechanical interlocking structure resulting in greatly improved adhesion between the Al and the matrix.

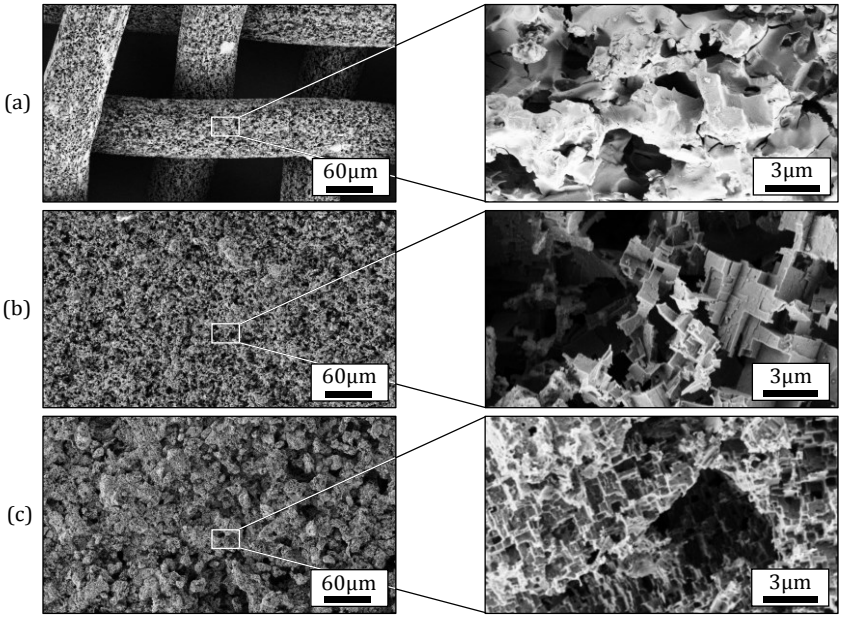

Figure 3.2: SEM images of Al plies after nanoscale sculpturing: (a) Al* fibre fabric (AA5019); (b) Plain Al* sheet (AA5754); (c) Plain Al* sheet (AA6082).

3.1.4 Thermoset polymer matrix

The matrix system consists of the epoxy resin RIMR 135 and the hardener RIMH 137 (Momentive Inc.). Resin and hardener are combined in a weight ratio of 10:3 using a mixer (drive: 450-1500rpm) for ~ 20 minutes under vacuum (~ 4 hPa).

3.2 Resin transfer moulding

In the first step, the inside of the aluminium mould is cleaned with aceton. Then a form release agent, Mikon W-64+ (Münch Chemie International GmbH), is applied on all surfaces as well as on the frame inside. The frame thickness varies (1 - 5 mm) depending on the required specimen geometry. Afterwards, the different layers are laid-up in the RTM mould and a 1 cm wide fleece strip is placed around the layers to prevent quick flowing of the epoxy along the edges of the mould during the RTM-process. Additionally, for the DCB and ENF specimens, a Polytetrafluoroethylene (PTFE) insert (thickness: 10 µm) (Goodfellow) is placed in the mid plane of the laminates, which serves as a delamination initiator. The mould is closed with screws and placed in a heating press at T = 40 °C. The vacuum on the trap side it set to ~ 4 hPa. The epoxy flow is throttled to a minimum by a clamp. By using permeable metal plies for the FMLs, the epoxy can flow in the thickness direction, reducing the process time by several minutes compared to using solid metal sheets for the FMLs or a pure GFRP laminate. Figure 3.3 schematically shows the RTM-process. The laminates are cured in the mould at 40 °C for 24 hours and post-cured at 80 °C for 15 hours. To reduce shrinkage of the epoxy the resource side is set to ~ 3000 hPa after injection.

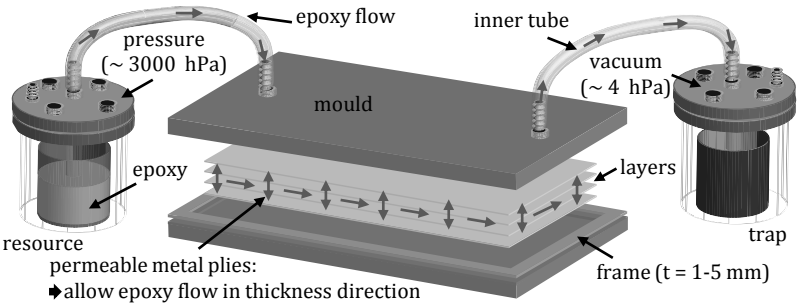

Figure 3.3: RTM-process (schematic).

3.3 Specimen preparation

The laminates are cut-out into specimens according to the corresponding standard of the mechanical tests using a cutting machine ATM Brillant 265 (ATM GmbH). The specimen edges are polished with SiC sandpaper up to grade P1000 to minimise edge effects and afterwards placed in a vacuum (~ 4 hPa) oven at 40 °C for 72 hours until the loss of mass is constant. The specimens are stored in a desiccator before testing to prevent further moisture absorption. The specimens for DCB, ENF, and DNS are cut from the same laminates for each configuration. For the static bearing and CAI testing a speckle pattern is sprayed on one side of each specimen allowing computer-aided image evaluation using a three-dimensional (setup with two cameras) digital image correlation (DIC) system ARAMIS 4M (GOM GmbH) to determine the bearing strain. To measure the capacitance during some tests, copper wires (diameter: 0.2 mm) are attached to the metal plies with silver conductive paint (Electrodag 1415 M).

3.3.1 Double notch shear (DNS)

Two parallel notches to the prescribed depth on each opposite side of the specimen is undertaken using a precision cutting machine ATM Brillant 220 (ATM GmbH). Light microscopy is used to visually inspect the quality of each specimen. The specimens are cut in longitudinal and transverse direction. The specimens are 79.5 mm long, 12.7 mm wide, and 5 mm thick.

3.3.2 Double cantilever beam (DCB)

One edge of the specimen is coated with a thin layer using white spray paint to aid in visual detection of delamination onset and crack growth. From the insert tip the first 5 mm are marked with thin vertical pencil lines every 1 mm, the remaining 20 mm every 5 mm. Aluminium loading blocks (20 mm · 20 mm) are bonded with an instant adhesive on each side of the laminate at the end of the initial crack to apply the opening force during the DCB test. The specimens are 125 mm long, 20 mm wide, and 5 mm thick.

3.3.3 End-notched flexure (ENF)

One edge of the specimen is coated with a thin layer using white spray paint to aid in visual detection of the delamination tip. The insert tip and the three compliance calibration (CC) positions are marked with thin vertical pencil lines. The specimens are 160 mm long, 20 mm wide, and 5 mm thick.

3.3.4 Tension (longitudinal/transverse) of UD-GFRP

End-tabs made of a combination of 50 mm long and 1 mm thick cured ±45°-GFRP with 1 mm thick Al strips are applied on both sides using a 2-component epoxy adhesive (UHU Endfest 300). The specimens are 250 mm long, 15 mm (longitudinal) and 25 mm (transverse) wide, and 2 mm thick.

3.3.5 Compression (longitudinal/transverse) of UD-GFRP

End-tabs made of 65 mm long and 2 mm thick ±45°-GFRP are applied on both sides using a 2-component epoxy adhesive (UHU Endfest 300). The strain measurement is carried out with strain gauges EA-06-060LZ-120/E (Vishay Precision Group Inc) glued on both sides. The specimens are 140 mm long, 25 mm (longitudinal) and 10 mm (transverse) wide, and 2 mm thick.

3.3.6 Tension of nanoscale sculptured aluminium alloy sheets

After the RTM process the nanoscale sculptured metal sheets (thickness: AA5754 ~ 0.9 mm; AA6082 ~ 0.65 mm) result in laminates with a thickness of 1 mm. Dogbone specimens are cut in longitudinal and transverse direction. The length is 220 mm and the width 20 mm.

3.3.7 Tension of GFRP with stepped lap metal sheets

The specimens are 250 mm long, 36 mm wide, and 5 mm thick. The GF layers and the embedded metal sheets are laid-up according to the bearing response specimens (chapter 3.3.10).

3.3.8 Low-velocity impact

The specimens are 150 mm long, 100 mm wide, and 5 mm thick.

3.3.9 Compression after impact

The FML specimen edges are insulated with a thin adhesive tape to avoid short-circuit during the capacitance measurement. For a better comparison, the GFRP specimen edges are also insulated. Pre-tests with and without adhesive tape resulted in a negligible influence on the mechanical CAI properties.

3.3.10 Static and fatigue pin- and bolt-loaded bearing response

End-tabs made of a combination of 50 mm long and 1 mm thick cured ±45°-GFRP with 1 mm thick Al strips are applied on one side using a 2-component epoxy adhesive (UHU Endfest 300). The drill hole is machined by one-shot-drilling (d = 6.3H7) using a FP3A Deckel machine (provided by the Institute of Production Management and Technology, Hamburg University of Technology) and hard metal-drill with crystalline diamond coating (Garant). Various one-shot-drill pre-test with different parameters are done with GFRP and FML specimens to reach a high quality drill hole. The spindle speed is set to n = 1600 rpm and the feed speed is set to v_t = 176 mm/min.

Figure 3.4 shows the SEM images of representative GFRP and FML drill holes without indicating delamination, intra-laminar matrix cracks, or other significant damages affecting the laminate quality.

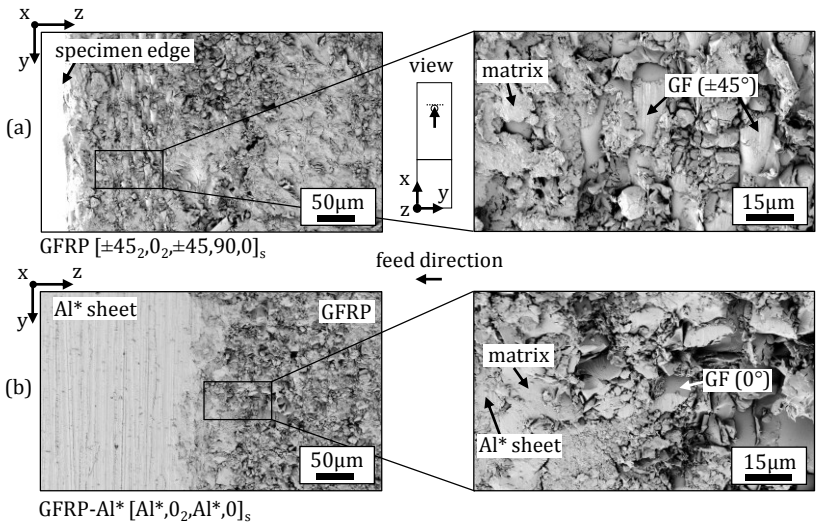

Figure 3.4: Representative SEM images of a drill hole: (a) GFRP; (b) FML.

The edge distance to pin and bolt diameter (e/d) as well as width to pin and bolt diameter (w/d) are experimentally pre-determined to ensure true bearing failure for all laminates. The GFRP specimens (e/d = 3) resulted in early shear-out failure under fatigue bolt-loaded (8 Nm) bearing. For a good comparison, the ratios for all specimens are set to e/d = 3 (static), 4 (fatigue), and w/d = 5.7. Figure 3.5 depicts the specimen design of the FMLs. The metal sheets are stepped inserted into the laminate along the length to avoid an abrupt change in stiffness.

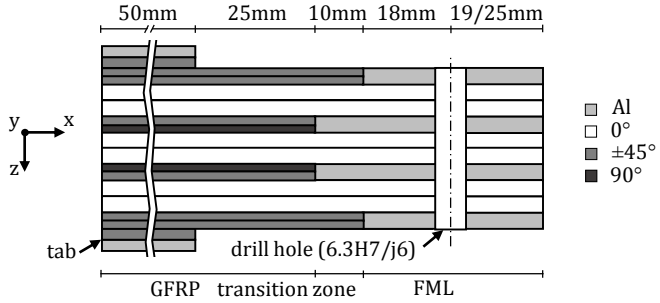

Figure 3.5: Specimen design for the bearing response of FMLs with stepped lap metal sheets.

4 Experimental methods

4.1 Quality assurance

To assure a high quality and reproducibility of the laminates, the glass transition temperature, the fibre-metal volume fraction, and optical microscopic edge views are analysed. For full traceability of all specimens, a sophisticated process plan is created for each laminate, which clearly displays the specimen arrangement of the different tests and documents the manufacturing date as well as the temperature and humidity during the tests (Figure 4.1).

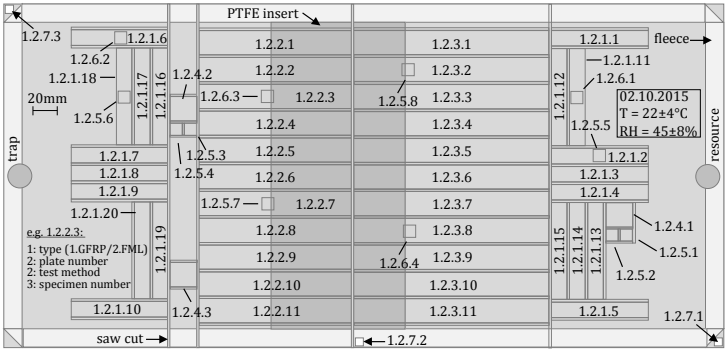

Third digit of index number (test method); 1: Double notched shear; 2: Double cantilever beam; 3: End notched flexure; 4: Fibre and metal volume fraction; 5: Optical microscopic edge view; 6: Scanning electron microscopy image; 7: Glass transition temperature.

Figure 4.1: Traceability of the different specimens/test methods (schematic).

4.1.1 Glass transition temperature

The glass transition temperature T_g is strongly dependent on the resin-hardener composition and the curing process. For all laminates T_g is measured using the differential scanning calorimetry (DSC) 204 F1 Phoenix (Netzsch GmbH & Co. Holding KG). Of each laminate, three different parts from the edges are cut and the amount of ~ 10-15 mg epoxy of each sample is analysed. The samples are heated twice to 150 °C with a heat rate of 20 K/min. The onset temperature $T_{g,onset}$ of the first heat rate curve is evaluated because the change of the mechanical properties occurs there first.

4.1.2 Fibre and metal volume fraction

The fibre and metal volume fractions $V_{f/metal}$ are determined by the standard DIN EN ISO 1172. Of each laminate, three different parts (20 mm · 20 mm) are cut and placed in a muffle furnance. In this process, the matrix is removed by high temperature (T = 550 °C) to receive the fibre and metal weight fraction with respect to the composite.

4.1.3 Optical microscopic edge view

Optical microscopic edge views of different parts of the laminates are analysed by means of visually inspecting fibre alignment, voids, and defects as well as damages after testing using a polyvar microscope with reflected light mode (Leica Microsystems GmbH). For this purpose, samples are cut in the longitudinal and transverse direction of the laminate and embedded with KEM 15plus (ATM GmbH) in a mould. Before examining all samples are polished with an ATM Saphir 550 polishing machine (ATM GmbH) using SiC sandpaper and diamond suspensions with a particle sizes down to 1 µm.

4.1.4 Scanning electron microscopy

The fracture surface of the specimens is inspected using a LEO 1530 FE (Carl Zeiss) SEM. The samples are sputtered with a gold layer (thickness: ~ 20 nm) to prevent an electric charge and investigated at an acceleration voltage of 3 kV. The secondary electron-detector (SE2) is used for the topographic analysis of the fracture surface.

4.2 Mechanical testing

For all mechanical tests a minimum of five specimens of at least two different laminates of each lay-up are tested at room temperature.

4.2.1 Double notch shear (DNS)

The DNS tests (Figure 4.2) are performed using a mechanical Zwick-Roell Z010 universal testing machine according to ASTM D-3846-08 [69]. A supporting jig is utilised to prevent out-of-plane deformation of the specimen under compression. The nuts of the supporting jig are tightened using a torque wrench. This leads to slight friction between the specimen and the supporting jig during loading. The crosshead speed in compression is set to 1.3 mm/min. The load-displacement response is recorded.

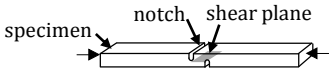

Figure 4.2: Schematic test set-up DNS.

4.2.2 Double cantilever beam (DCB)

The DCB tests (Figure 4.3) are performed using a Zwick-Roell Z010 universal testing machine according to ASTM D-5528-02 [122]. The crosshead speed is set to 2 mm/min. The load response-crack opening and the crack growth are recorded. For some specimens the capacitance is measured in-situ. The onset of the crack growth from the PTFE insert is determined by an inspection of the specimen edge with a magnifier lamp (10 times magnification). The delamination length is the sum of the distance from the loading line to the end of the insert (a_0 = 53 mm) plus the maximum crack growth (a = 25 mm).

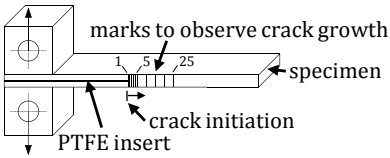

Figure 4.3: Schematic test set-up DCB.

4.2.3 End-notched flexure (ENF)

The ENF tests (Figure 4.4) are conducted using a mechanical Zwick-Roell Z010 universal testing machine according to ASTM D-7905-14 [88]. The pre-crack length is a_0 = 30 mm. The crack lengths (a_1 = 20 mm and a_2 = 40 mm) are used during the CC method by appropriate placement of the specimen in the fixture. The crosshead speed is set to 0.5 mm/min. The load-displacement response is recorded. For some specimens the capacitance is measured in-situ.

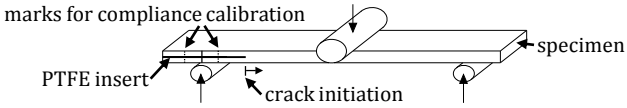

Figure 4.4: Schematic test set-up ENF.

4.2.4 Tension (longitudinal/transverse) of UD-GFRP

The tensile tests (Figure 4.5) in longitudinal and transverse direction of GFRP laminates are conducted using a mechanical Zwick-Roell 400 kN universal testing machine according to ASTM D3039-00 [123]. The specimens are clamped with wedge clamping jaws. The crosshead speed is set to 2 mm/min. The displacement is measured on the specimen surface using a long-travel extensometer (the initial distance is set to 50 mm) and the load-displacement is recorded.

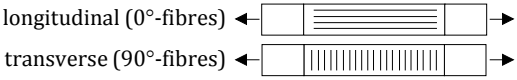

Figure 4.5: Schematic test set-up tension of UD-GFRP.

4.2.5 Compression (longitudinal/transverse) of UD-GFRP

The compression tests (Figure 4.6) in longitudinal and transverse direction of GFRP laminates are conducted using a mechanical Zwick-Roell 400 kN universal testing machine according to ASTM D3410-03 [124]. The specimens are clamped with a hydraulic composites compression fixture (IMA Materialforschung und Anwendungstechnik GmbH).

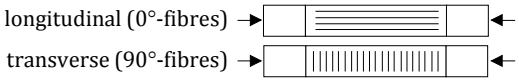

Figure 4.6: Schematic test set-up compression of UD-GFRP.

The crosshead speed is set to 1 mm/min. The displacement is measured via strain gauges using a measurement amplifier MGCPlus (HBM GmbH) and the load-displacement is recorded.

4.2.6 Tension of nanoscale sculptured aluminium alloy sheets

The tensile tests (Figure 4.7) in longitudinal and transverse direction of the nanoscale sculptured AA5754 and AA6082 metal sheets are conducted using a mechanical Zwick-Roell 400 kN universal testing machine according to DIN EN ISO 6892-1 [125]. The specimens are clamped with wedge clamping jaws. The crosshead speed is set to 2 mm/min. The displacement is measured on the specimen surface using a long-travel extensometer (the initial distance is set to 100 mm) and the load-displacement is recorded.

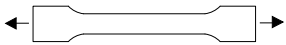

Figure 4.7: Schematic test set-up tension of aluminium alloy sheets.

4.2.7 Tension of GFRP with stepped lap metal sheets

The tensile tests (Figure 4.8) are conducted on a mechanical Zwick-Roell 400 kN universal testing machine with a constant displacement rate of 2 mm/min according to the static bearing response tests (chapter 4.2.10). The specimens are clamped with wedge clamping jaws. The displacement is measured on the specimen surface using a long-travel extensometer (the initial distance is set to 50 mm) and the load-displacement is recorded.

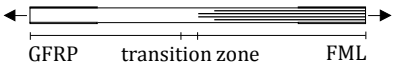

Figure 4.8: Schematic test set-up tension of GFRP with stepped lap metal sheets.

4.2.8 Low-velocity impact

The low-velocity impact (Figure 4.9) tests are conducted on a drop weight tower with a hemispherical hardened steel striker tip (d = 20 mm, m = 5.46 kg) according to ASTM D-7136-05 [126] resulting in an impact energy of 20.6 J. The striker tip is equipped with a strain gauge full bridge to measure the contact forces during the impact. An anti-rebound system, activated by a photo sensor, is used to avoid multiple impacts during testing. The impact Al support fixture frame has a cut-out of 75 mm · 125 mm.

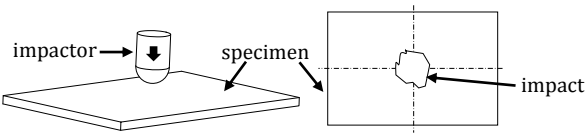

Figure 4.9: Schematic test set-up low-velocity impact.

4.2.9 Compression after impact

The CAI tests (Figure 4.10) are conducted using a mechanical Zwick-Roell 400 kN universal testing machine according to ASTM D-7137-05 [127]. The crosshead speed is set to 1.25 mm/min. The specimens are pre-loaded with a compressive force of 450 N. Afterwards, the compressive force is set to 150 N and all instrumentation are set to zero. The load-displacement curve is recorded. The DIC system measures the strain on the specimen surface (non-impacted side) during testing to ensure that no instability or excessive bending (> 10 %) of the specimen occurs.

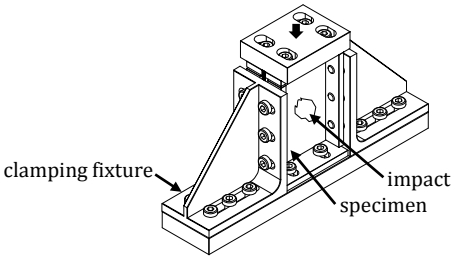

Figure 4.10: Schematic test set-up CAI.

4.2.10 Static and fatigue pin- and bolt-loaded bearing

The bearing tests are performed by the double-shear tensile loading of the specimens with a single bolt according to ASTM D-5961-13 [90] for static testing and according to ASTM D-3479-96 [128] for fatigue testing. The tests are conducted with a modified loading fixture according to [98,129], to enable observation of the specimen surface in front of the pin or bolt by DIC (static testing) or passive thermography (fatigue testing). Two types of tests are carried out using a stainless steel fixture assembly to determine the bearing strength. The first (Figure 4.11a) without lateral restraint (pin-loaded bearing) and the second (Figure 4.11b) providing lateral restraint (bolt-loaded bearing) by means of stainless steel washers with 6.3 mm internal and 12.6 mm external diameter. The pin and bolt is made from 42CrMo4 steel and has a diameter of d = 6.3j6 causing a transition fit H7/j6 between the pin/bolt and the hole. The bolted joints are tightened with 1, 4 and 8 Nm for the static and with 8 Nm for the fatigue specimens using a calibrated HAZET 5107-2CT torque wrench. The 8 Nm torque corresponds approximately to the torque of a 1/4 inch Hi-Lok fastener used in the aviation industry.

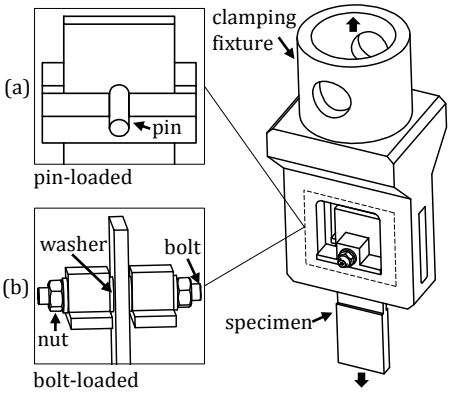

Figure 4.11: Schematic test set-up according to [40]: (a) Pin-loaded bearing; (b) Bolt-loaded bearing.

The static tests are conducted on a mechanical Zwick-Roell 400 kN testing machine with a constant displacement rate of 2 mm/min. The specimens are clamped on one side with wedge clamping jaws. The load-displacement is recorded and the offset bearing strength (2 % hole expansion) is evaluated. The DIC system measures the bearing strain (ε^{br}) on the specimen surface for the static testing.

The fatigue tests are conducted on an Instron-Schenk 8800PL100K servo-hydraulic machine under load control with a constant amplitude and a sinusoidal waveform cycling at a cyclic frequency of 5 Hz (bolt-loaded) and 10 Hz (pin-loaded) and at a stress ratio ($R = \sigma_{min}/\sigma_{max}$) equal to 0.1 (tension-tension fatigue). However, tensile loading of the specimen under bearing leads to a compression of the constituents in the pin/bolt area. Therefore, the stress ratio R is equal to 10 (compression-compression fatigue). The specimens are clamped with hydraulic jaws with a torque of 8 Nm. Fatigue stress (S) vs. cycles (N) data are used to generate mean lifetime S-N curves, which represent the applied maximum bearing stress vs. log cycles to 2 % hole expansion and final failure. The 2 % hole expansion is determined by the change of the machine actuator position relative to the initial value. In order to ensure an accurate measuring of the hole expansion, pre-tests with specimens at different load levels are conducted. Therefore, the fatigue tests are stopped after 1, 10, 100, and 1000 cycles to measure the hole dimension of the specimens relative to the initial value and to compare it with the actuator positon. Each specimen is tested with a new bolt to prevent fatigue of the bolt. Passive thermography measurements are conducted with a non-destructive infrared testing system (Automation Technology GmbH) and an infrared camera Photon A615 (Flir) to ensure that no significant increase in temperature of the specimens occurs during cycling loading.

4.3 Health monitoring

4.3.1 Acoustic emission

The acoustic emission is monitored using a 32-channel Micro-II AE system and a R6D-transducer (Physical Acoustics Corp.) The cumulative AE energy (total number of energy counts) is recorded using a wideband differential

sensor. For the CAI test the sensor is placed on the impacted side of the specimen at a distance of ~ 50 mm to the centre of the impact. For the static bearing response test the sensor is placed at a distance of ~ 40 mm to the drill hole. The maximum signal amplitude is 100 dB. Before monitoring, the breaking of a lead pencil near the sensor is conducted to verify its response to an acoustic signal resulting in very similar results (~ 100 dB) for GFRP and FMLs. The threshold of the amplitude is set to 50 dB to eliminate the influence of background noise.

4.3.2 Capacitance measurement

The capacitance of the specimens is measured via attached copper wires (diameter: 0.2 mm) using a PeakTech 2170 LCR meter. The resolution is 1 pF (100 Hz) and 0.1 pF (1 kHz). The specimens are placed in the mechanical testing fixtures before measuring the initial capacitance values. For each specimen, the variation of capacitance is measured, and normalised to the initial capacitance. The measured data of each LCR meter are recorded by separate laptops without using a power supply, to minimise electrical interferences. Figure 4.12 schematically presents the set-up of the mechanical ENF test with in-situ health monitoring.

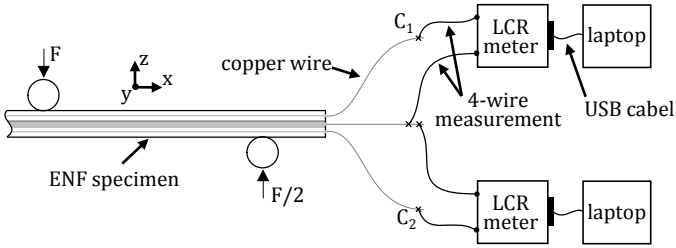

Figure 4.12: Schematic set-up of the mechanical ENF test with in-situ health monitroing [38].

DCB and ENF test set-up

The capacitance of the DCB and ENF specimens is measured with different test frequencies (f = 100 Hz, 1 kHz). Two LCR meters are used, to detect possible crack growth in two interfaces in case of crack jumping. For the test set-up of the GFRP-WMF laminate only one LCR meter is used. Otherwise the

test set-up is similar. The electrical set-up of the DCB and ENF tests is the same for each laminate.

Tension of GFRP with stepped lap metal sheets test set-up

The capacitance is measured with the test frequency (f = 1 kHz) at the outer metal plies during the tensile test.

Low-velocity impact and compression after impact test set-up

The capacitance of the specimens is measured before and after the impact as well as during the CAI loading with the test frequency (f = 100 Hz). Two LCR meters are used to detect damages between the metal sheets during CAI loading.

Static bearing response test set-up

The bearing loading with in-situ capacitance measurement (f = 1 kHz) requires an insulating coating of the alloy steel (42CrMo4) pin to avoid short-circuit during testing. For this purpose, the pin is coated with a thin (~ 100 µm) ceramic (Al oxide) using atmospheric plasma spraying (Coating Center Castrop GmbH) causing a transition fit H7/j6 between the pin and the hole. The schematic set-up of the mechanical bearing response test with in-situ healVth monitoring and the corresponding electrical circuit are illustrated in Figure 4.13.

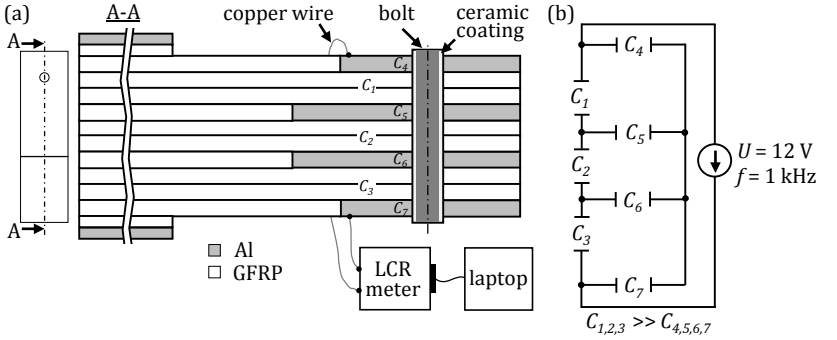

Figure 4.13: (a) Schematic set-up of the mechanical bearing response test with in-situ health monitoring; (b) Corresponding electrical circuit (simplified).

5 Results and discussion

The onset glass transition temperature results in a mean value of $T_{g,onset}$ = 86±3 °C for all laminates. The fibre-metal volume fraction of the laminates is listed in the tables of the corresponding testing results of this chapter. All composites show a high inter- and intra-laminar matrix wetting with no visible imperfections.

The FML composed of untreated solid Al sheets shows early delamination, either between the two metal sheets or between the metal sheet and GFRP layer, already after cutting the specimens. SEM images and light microscopic edge view results demonstrate in both cases adhesive failure of the metal-matrix interface. This result indicates the extremely low interfacial bonding between the untreated Al sheets and the matrix. Hence, this FML is not further investigated in terms of mechanical properties.

In order to show the potential of the SHM method on the pin-loaded bearing response (Chapter 5.6.6), untreated perforated Al sheets are used. Although the interfacial strength of the Al-matrix bond is extremely low, the perforated Al sheets lead to the formation of matrix bridges that prevent premature delamination during testing (Figure 5.41a).

5.1 Inter-laminar properties

Different GF and metal plies are investigated to characterise the inter-laminar properties under DNS, DCB, and ENF loading. Table 5.1 shows the lay-up, fibre and metal volume fraction, and density of the laminates. The results of the FMLs are significantly influenced by the surface treatment and permeability of the metal plies, which influence the mechanical adhesion between the constituents depending on the loading mode.

Table 5.1: Lay-up, fibre and metal volume fraction, and density of the laminates.

Laminate	Lay-up	V_f (%)	V_{metal} (%)	ρ (g/cm³)
GFRP	$[0_6]_s$	$47.5^{\pm 0.4}$	-	$1.81^{\pm 0.01}$
GFRP#	$[(0^{90\%},90^{10\%})_2,(90^{10\%},0^{90\%})_3]_s$	$46.2^{\pm 0.8}$	-	$1.79^{\pm 0.02}$
GFRP#-Al_{28}	$[(0^{90\%},90^{10\%})_2,(90^{10\%},0^{90\%})_3,Al_{28}]_s$	$45.7^{\pm 0.4}$	$3.2^{\pm 0.1}$	$1.86^{\pm 0.01}$
GFRP#-Al*$_{28}$	$[(0^{90\%},90^{10\%})_2,(90^{10\%},0^{90\%})_3,Al^*_{28}]_s$	$46.1^{\pm 0.3}$	$3.0^{\pm 0.5}$	$1.85^{\pm 0.02}$
GFRP#-Al_{23}	$[(0^{90\%},90^{10\%})_2,(90^{10\%},0^{90\%})_2,Al_{23}]_s$	$36.8^{\pm 0.5}$	$22.3^{\pm 0.4}$	$2.01^{\pm 0.04}$
GFRP#-Al*$_{23}$	$[(0^{90\%},90^{10\%})_2,(90^{10\%},0^{90\%})_2,Al^*_{23}]_s$	$35.9^{\pm 0.2}$	$18.6^{\pm 0.9}$	$1.95^{\pm 0.05}$
GFRP#-Al*$_0$	$[(0^{90\%},90^{10\%})_2,(90^{10\%},0^{90\%})_2,Al^*_0]_s$	$36.1^{\pm 0.5}$	$23.4^{\pm 1.2}$	$2.02^{\pm 0.07}$
GFRP#-St_{28}	$[(0^{90\%},90^{10\%})_2,(90^{10\%},0^{90\%})_3,St_{28}]_s$	$46.0^{\pm 0.6}$	$2.8^{\pm 0.3}$	$1.99^{\pm 0.02}$
GFRP#-St_{61}	$[(0^{90\%},90^{10\%})_2,(90^{10\%},0^{90\%})_3,St_{61}]_s$	$44.9^{\pm 0.2}$	$1.5^{\pm 0.6}$	$1.89^{\pm 0.03}$
GFRP#-St_{20}	$[(0^{90\%},90^{10\%})_2,(90^{10\%},0^{90\%})_2,St_{20}]_s$	$35.7^{\pm 0.4}$	$10.3^{\pm 0.5}$	$2.38^{\pm 0.02}$
GFRP#-St_{74}	$[(0^{90\%},90^{10\%})_2,(90^{10\%},0^{90\%})_2,St_{74}]_s$	$37.7^{\pm 0.6}$	$4.19^{\pm 0.7}$	$1.98^{\pm 0.02}$

(*): nanoscale sculptured; Al_x/St_x : X % permeability of Al/St ply (Figure 3.1)

5.1.1 Double notch shear (DNS)

Figure 5.1 depicts the load (P)-displacement (δ) response of representative specimens. In the initial stage of loading all laminates are non-linear, mainly due to the self-aligning processes between the test fixture and the specimen. The influence of friction on the test results is relatively low. The average value of the friction force of all laminates is P = 240±12 N. Subsequently, the curves increase monotonically up to this load where first inter-laminar failures occur. The laminates fail spontaneously as soon as the maximum in-plane shear stress is reached indicated by the sharp drop in the P-δ curve.

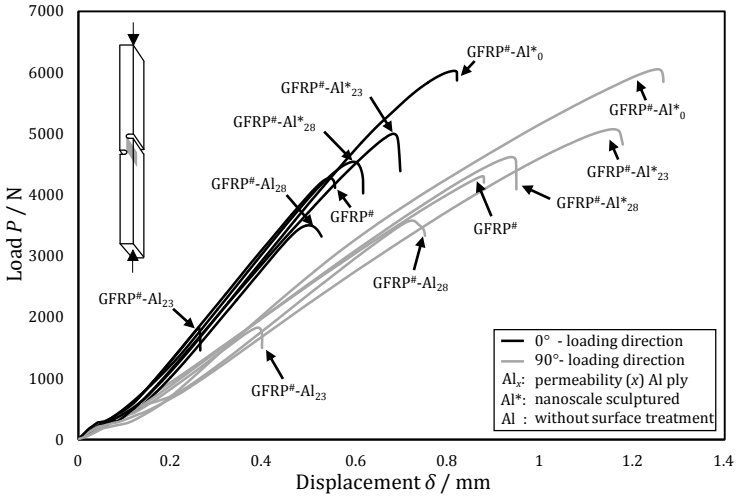

Figure 5.1: Load-displacement response of representative GFRP#, GFRP#-Al_{28}, GFRP#-Al^*_{28}, GFRP#-Al_{23}, and GFRP#-Al^*_{23}, GFRP#-Al^*_0 specimens under DNS loading according to [39].

Each type of laminate exhibits a similar maximum applied loading in 0°- and 90°-loading direction. A small amount of GFs oriented perpendicular to the principal fibre direction avoids premature intra-laminar failure in the laminate planes, which appeared during previous tests using only UD GF NCFs. The FMLs with permeable metal plies withstand higher loads before failure compared to untreated metal sheets because of the formation of matrix bridges (mechanical adhesion) between these plies. These matrix bridges increase the resistance against delamination leading to higher ILSS. Among the untreated Al plies the maximum load before failure increases with higher permeability of the metal plies. One can understand this in terms of a higher amount of matrix bridges between the metal plies. Nevertheless, the achieved maximum loads before failure are lower compared to the GFRP# references. The GFRP#-Al^*_0 shows the highest ultimate loading, followed by GFRP#-Al^*_{23} and GFRP#-Al^*_{28}. These loads are significant higher compared to the GFRP# reference. Here, the order of the FMLs is inverse compared to untreated Al plies. This can be explained by the mechanical interlocking surface structure of the Al* plies.

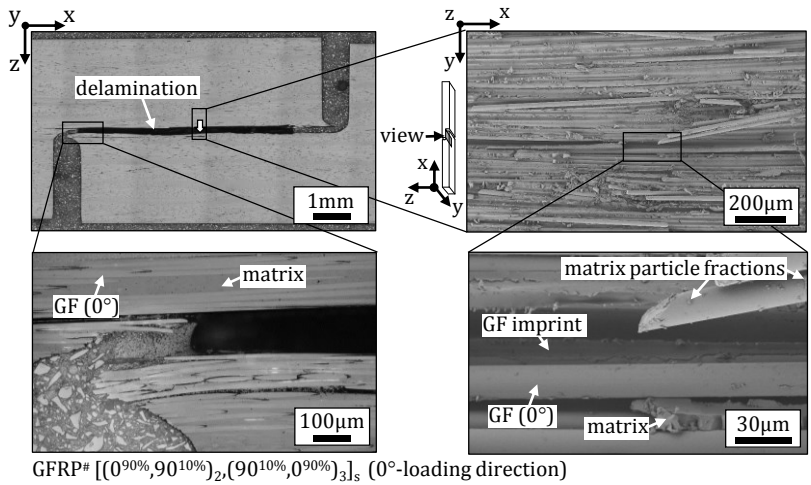

Figure 5.2: Optical microscopic edge view and SEM images of representative GFRP# specimens under DNS loading (0°-loading direction) according to [39].

Reducing the permeability of the Al* plies increases the nanoscale sculptured surface resulting in higher load before failure. The FML composites fail by reaching the maximum inter-laminar shear stress. The onset of sequential process of inter-laminar shear failures is expected to be initiated in the mid plane due to the maximum shear stress. This behaviour is shown by the pure GFRP# laminate (Figure 5.2) and the FMLs consisting of untreated Al plies (Figure 5.3a, Figure 5.4a). The fracture behaviour of the laminates looks similar in 0°- and 90°-loading direction. Therefore, only one representative is shown. The fracture surface analysis of the GFRP# laminates show smooth fibres with low matrix particle adherences. This indicates low interfacial strength of the fibre-matrix bond resulting in early adhesive failure and ply delamination.

The GFRP#-Al_{28} with untreated permeable woven Al fabric (Figure 5.3a) forms matrix bridges between the plies. These are expected to act as "crack-stoppers" due to the mechanical adhesion and thus increase the resistance against delamination. However, the in-plane shear failure is dominated by the Al-matrix interfacial strength and matrix properties.

Shear deformation triggers fracture by debonding between the Al-matrix and the formation of cusps resulting in ply delamination. Cusps occur as a result of shear stress ahead of the crack tip, which causes a tensile stress, at an angle of 45° to the laminate plane. By increasing the loading, these angled cracks start to extend along the 45° lines. By converging the vertical boundary of the Al-matrix interface the presence of the Al wires above and below leads to a rotation of the local crack tips. Consequently, these angled cracks produce the S-shaped cusps. These effects of cusp formation were found and described in other publications as well [130–133].

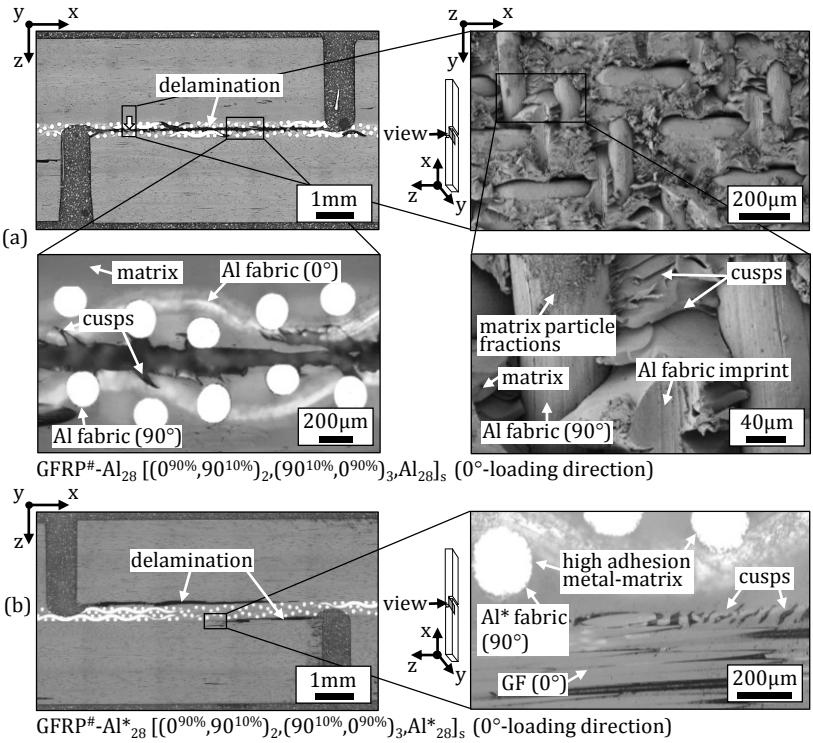

Figure 5.3: Optical microscopic edge view and SEM images of representative specimens under DNS loading (0°-loading direction) according to [39]: (a) GFRP#-Al$_{28}$; (b) GFRP#-Al*$_{28}$.

The inter-laminar bond between the pre-treated Al* plies of GFRP#-Al*$_{28}$ (Figure 5.3b), GFRP#-Al*$_{23}$ (Figure 5.4b), and GFRP#-Al*$_{0}$ (Figure 5.4c), as well as the untreated St plies of GFRP#-Al$_{74}$, is strong enough to withstand the shear stress in the interface. Therefore, delamination appears away from the neutral plane in the transition zone between GF and matrix due to the lower adhesion of the GF-matrix interface. Taking a closer look on the fracture surfaces, one detects that the actual interface, the adhesive Al*-epoxy bond, remains intact.

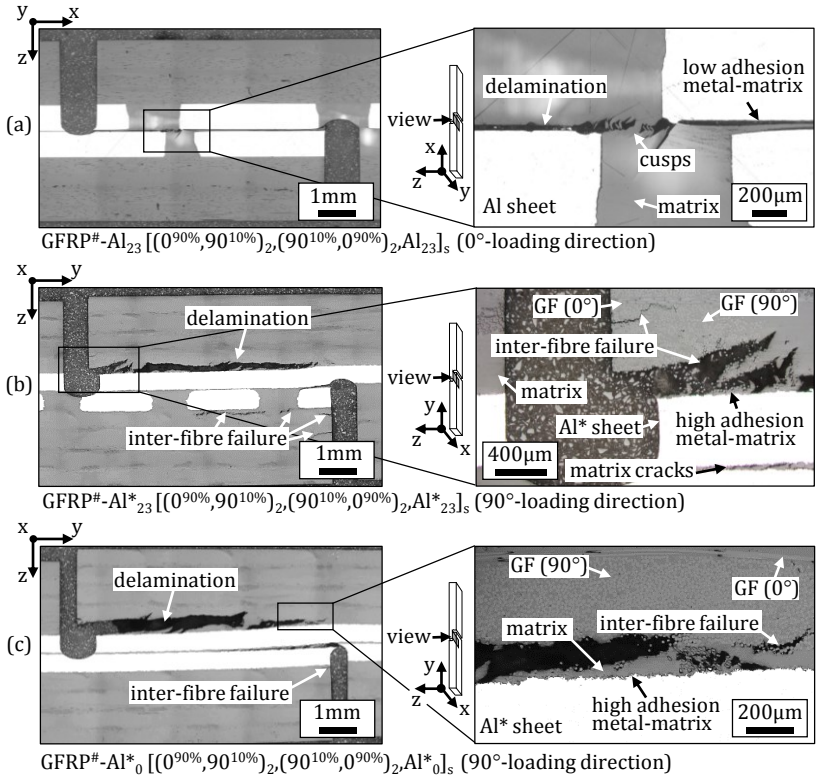

Figure 5.4: Optical microscopic edge view and SEM images of representative specimens under DNS loading according to [39]: (a) GFRP#-Al$_{23}$ (0°-loading direction); (b) GFRP#-Al*$_{23}$ (90°-loading direction); (c) GFRP#-Al*$_0$ (90°-loading direction).

This observation can be explained by the three-dimensional mechanical interlocking surface structure of the Al* plies after nanoscale sculpturing. The cubical hook-like structures are completely enclosed by the epoxy forming a high connection between the Al* and the epoxy. Along the whole mid plane the distance (x) between the metal sheets is $30 \leq x \leq 80$ µm. Consequently, the two metal sheets do not touch at any point during testing.

The GFRP$^{\#}$-Al*$_{28}$ (Figure 5.3b) combines the effect of mechanical adhesion by the formation of matrix bridges and the mechanical interlocking by the surface structured woven Al* fabric resulting in a high Al*-matrix interfacial strength. Consequently, delamination appears in the transition zone between GF and matrix due to the lower bonding between fibre and matrix. Furthermore, the GFRP$^{\#}$ layers show cusp formation. The GFRP$^{\#}$-Al$_{23}$ (Figure 5.4a) with untreated perforated Al sheets fails mainly by delamination due to the low Al-matrix bond. The effect of the mechanical adhesion due to the permeability of the Al sheets is similar to the GFRP$^{\#}$-Al$_{28}$. The GFRP$^{\#}$-Al*$_{23}$ and GFRP$^{\#}$-Al*$_{0}$ (Figure 5.4b,c) demonstrate an analogue fracture behaviour compared to GFRP$^{\#}$-Al*$_{28}$. Delamination occurs away from the neutral plane in the transition zone between GF-matrix. The Al* sheets show a high adhesion bonding to the matrix.

Figure 5.5 presents the inter-laminar shear strength of the laminates showing similar values in 0°- and 90°-loading direction. The specimens of each configuration are cut-out from different areas of the laminate, leading to slightly different hole and mesh patterns of the two permeable metal plies. Due to the relatively low standard deviation, the influence on the testing results appears to be negligible. The friction between the specimen and the supporting jig ($\sim$ 1.5 MPa) is considered for all laminates. The hybrid composites with untreated Al plies always exhibit lower ILSS compared to the GFRP reference, in case of the GFRP$^{\#}$-Al$_{23}$ even less than 50 % of the reference ILSS. All investigated hybrid composites with nanoscale sculptured Al* plies (GFRP$^{\#}$-Al*$_{28}$, GFRP$^{\#}$-Al*$_{23}$ and GFRP$^{\#}$-Al*$_{0}$) always reveal much higher ILSS compared to the GFRP reference, in case of GFRP$^{\#}$-Al*$_{0}$ even about 30 % higher.

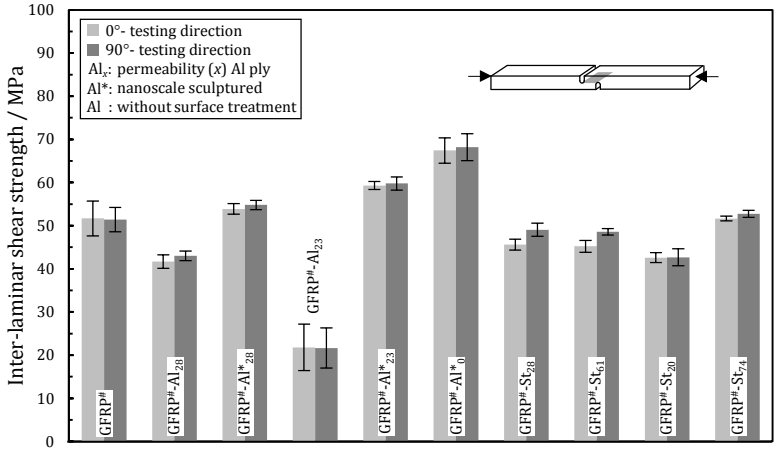

Figure 5.5: Mean and standard deviation of the ILSS of all investigated laminates under DNS loading according to [39].

The shear failures of FMLs with nanoscale sculptured Al plies show that the fracture occurs away from the neutral plane. Therefore, the local shear strength between the nanoscale sculptured Al* plies could be even higher than the measured shear strength.

5.1.2 Double cantilever beam (DCB)

The load (P)-crack opening (δ) responses of representative GFRP, GFRP#, GFRP#-Al$_{23}$, and GFRP#-Al*$_{23}$ specimens are illustrated in Figure 5.6. The curves show a linear behaviour up to a point where the delamination front in the mid plane starts to grow (crack initiation). This point is indicated as the initiation delamination toughness ($G_{\mathrm{Ic,init.}}$). The composites display sharp drops in the P-δ graphs, which indicate unstable crack growth. For the GFRP and GFRP# laminate, the load after crack initiation continues to increase up to a maximum value due to fibre bridging and bridging of the PES weft (only GFRP#). These effects for FRPs have also been reported by other authors [130,133]. The PES weft within the GFRP# significantly influences the inter-laminar fracture toughness resulting in $G_{\mathrm{Ic,init.}} = 299\pm8$ J/m^2 (GFRP), $G_{\mathrm{Ic,init.}} = 417\pm34$ J/m^2 (GFRP#).

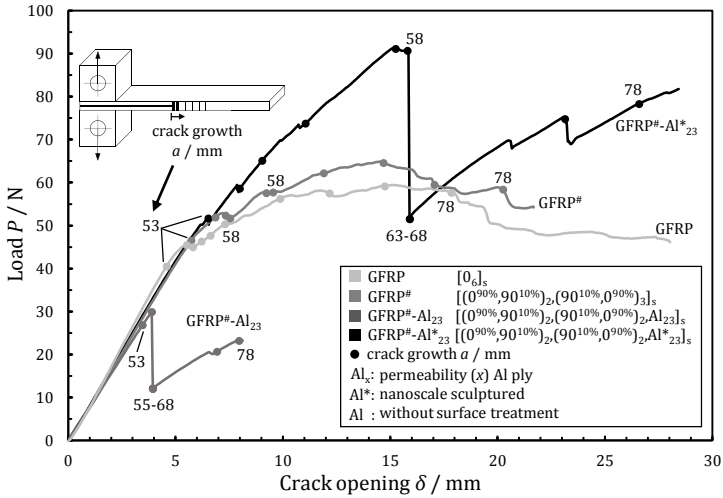

Figure 5.6: Load-crack opening response of representative GFRP, GFRP#, GFRP#-Al_{23}, and GFRP#-Al^*_{23} specimens under DCB loading according to [39]; numbers indicate crack growth.

All laminates with permeable metal plies lead to the formation of matrix bridges (mechanical adhesion) between the two metal plies. These matrix bridges increase the resistance against delamination. As soon as the normal stress during DCB (mode I) loading reaches a critical stress, the crack suddenly propagates a few millimetres and the load drops drastically (Figure 5.6, GFRP#-Al_{23} and GFRP#-Al^*_{23}). Afterwards, the crack growth slows down or even stops until a critical stress is reached again. The achieved load at crack initiation for the GFRP#-Al_{23} with untreated Al sheets is significantly lower compared to the GFRP and GFRP# references resulting in $G_{Ic,init.}$ = 214±25 J/m². The GFRP#-Al^*_{23} with nanoscale sculptured Al* sheets shows a drastically higher fracture toughness compared to the untreated Al sheets resulting in $G_{Ic,init.}$ = 468±25 J/m². The FMLs with WMFs, except for the GFRP#-St_{20}, lead to crack jumping and double cracking, which causes a bridging of the metal wires. During further crack opening, the wires are under tension, which increases the load. Hence, G_{Ic} increases drastically. The wires fail if the maximum tensile strength is reached. All laminates display a rising R-curve behaviour since the energy release rate (G_{Ic}) increases with crack growth.

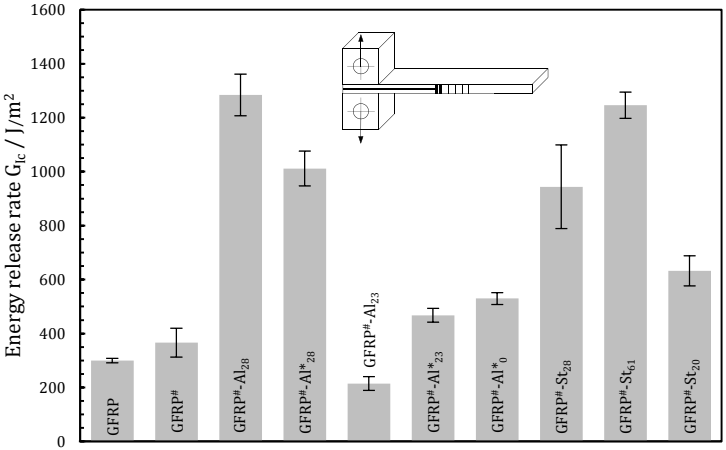

Figure 5.7: Mean and standard deviation of the energy release rate G_{IC} of all investigated laminates under DCB loading according to [39].

Figure 5.7 depicts the mean and standard deviation of the energy release rate G_{IC} of all investigated laminates. For all FMLs, the thermal influence of residual stresses [89] due to the different constituent properties is considered.

Figure 5.8 shows the optical microscopic edge view after testing. For the neat GFRP# laminate, the results show a low fibre-matrix interfacial strength resulting in early adhesive failure and ply delamination (Figure 5.8a). The GFRP shows a similar behaviour compared to the GFRP#. The GFRP#-Al_{23} laminate with untreated Al plies demonstrates a smooth metal surface revealing low adhesion between metal and matrix (Figure 5.8b). The other permeable metal plies with untreated surface also show low interfacial strength of the metal-matrix bond. In areas, where two holes/squares of both metal sheets/WMFs are aligned, the existing matrix bridges lead to cohesive failure, which increases the resistance against delamination. Nevertheless, the extremely low interfacial bonding between the untreated metal plies and the matrix results in early ply delamination. Within the GFRP#-Al*$_{23}$ laminate with nanoscale sculptured Al* plies (Figure 5.8c), the inter-laminar bond between the nanoscale sculptured Al* sheets and the matrix is strong enough

to withstand the normal stress during DCB loading causing crack jumping and double cracking. This effect increases the inter-laminar fracture toughness after crack initiation. Delamination appears in the mid plane due to cohesive matrix failure between the two metal sheets. Furthermore, delamination occurs at the GF-matrix interface, even without a triggering insert, due to the low interfacial bonding between the GF and matrix. The GFRP#-Al*$_{28}$ and GFRP#-Al*$_{0}$ laminates result in similar behaviour compared to the GFRP#-Al*$_{23}$. The multi-plane crack growth has also been observed in other publications [77,79,80].

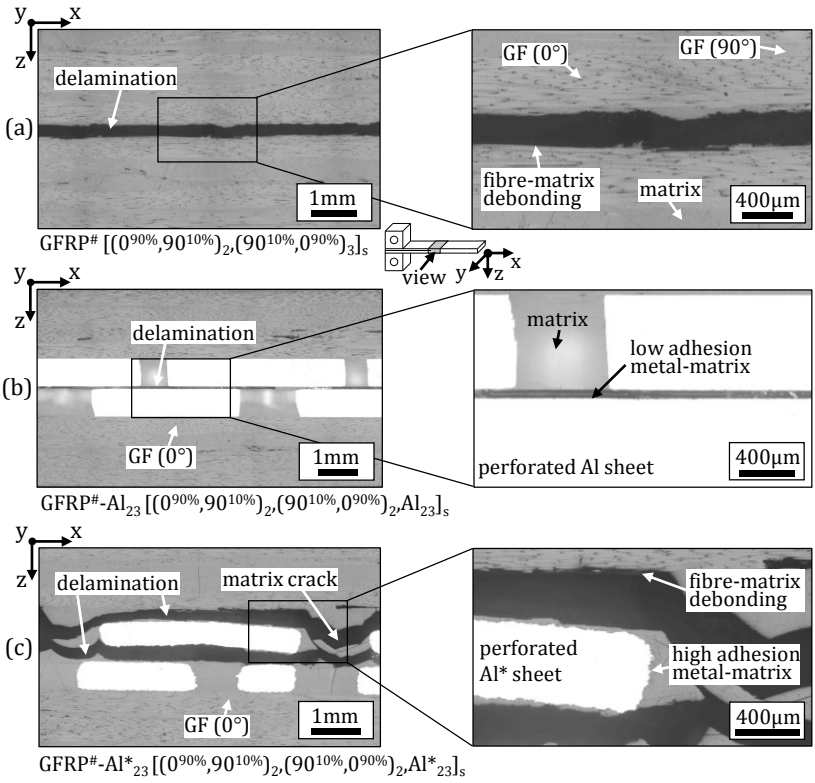

Figure 5.8: Optical microscopic edge view of representative specimens under DCB loading according to [39]: (a) GFRP#; (b) GFRP#-Al$_{23}$ with untreated Al plies; (c) GFRP#-Al*$_{23}$ with nanoscale sculptured Al* plies.

5.1.3 End-notched flexure (ENF)

Figure 5.9 shows the load (P)-displacement (δ) responses of representative GFRP, GFRP#, GFRP#-Al_{23}, and GFRP#-Al^*_{23} specimens. The laminates fail by reaching the maximum inter-laminar shear stress. Due to the different longitudinal flexural stiffness of the laminates the slopes of the first linear parts varies. The GFRP curve appears nearly linear and the FMLs demonstrate significantly higher plastic deformation before reaching the maximum loading. Due to the maximum amount of UD 0°-GF layers compared to the other laminates the GFRP laminate shows the highest flexural stiffness.

Between these four laminates, the GFRP-$Al^*_{23\%}$ leads to the highest inter-laminar fracture toughness (G_{IIc} = 2903±166 J/m²), followed by GFRP (G_{IIc} = 2384±197 J/m²), GFRP# (G_{IIc} = 2241±100 J/m²), and GFRP-$Al_{23\%}$ (G_{IIc} = 270±17 J/m²).

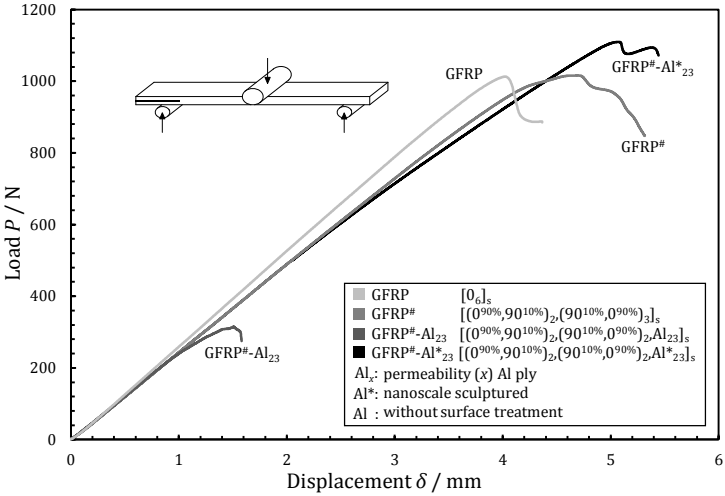

Figure 5.9: Load-displacement response of representative GFRP, GFRP#, GFRP#-Al_{23}, and GFRP#-Al^*_{23} specimens under ENF loading according to [39].

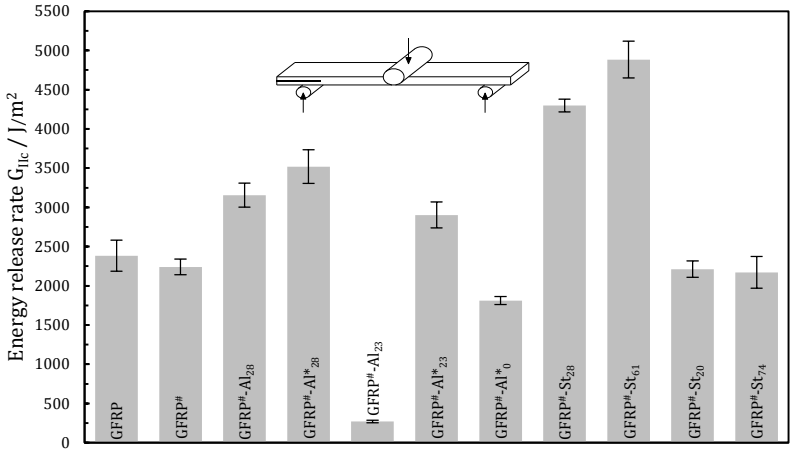

Figure 5.10: Mean and standard deviation of the energy release rate G_{IIC} of all investigated laminates under ENF loading according to [39].

Figure 5.10 shows the mean and standard deviation of the energy release rate G_{IIC} of all investigated laminates under ENF (mode II) loading. The thermal influence of residual stresses [134] for the FMLs due to the different material properties is considered leading to negligible contribution to the inter-laminar fracture toughness. All laminates with permeable metal plies lead to the formation of matrix bridges (mechanical adhesion) between the two metal plies resulting in higher resistance against delamination. In fact, the fracture toughness increases with increasing the amount of matrix bridges between the layers (increasing permeability). Although the GFRP#-Al_{74} has a high permeability, the dense WMF structure limits the formation of matrix bridges.

Figure 5.11 depicts the optical microscopic edge views after testing. For the GFRP# laminate, shear deformation triggers fracturing by debonding at the GF-matrix interface causing ply delamination (Figure 5.11a). The GFRP shows a similar behaviour compared to the GFRP#. The GFRP-$Al_{23\%}$ with untreated Al plies shows a smooth metal surface, revealing low interfacial strength of the metal-matrix bond with delamination at the metal-matrix interface (Figure 5.11b).

In areas, where two holes of both metal sheets are aligned, the existing matrix bridges lead to the formation of cusps. The GFRP-Al*$_{23\%}$ laminate images in (Figure 5.11c) show that the inter-laminar bond between the three-dimensional mechanical interlocking surface structures of the Al* ply is strong enough to withstand the shear stress in the interface. The cubical hook-like structures are completely enclosed by the matrix forming a very stable connection between the Al* ply and matrix. Hence, delamination appears due to cohesive failure of the matrix.

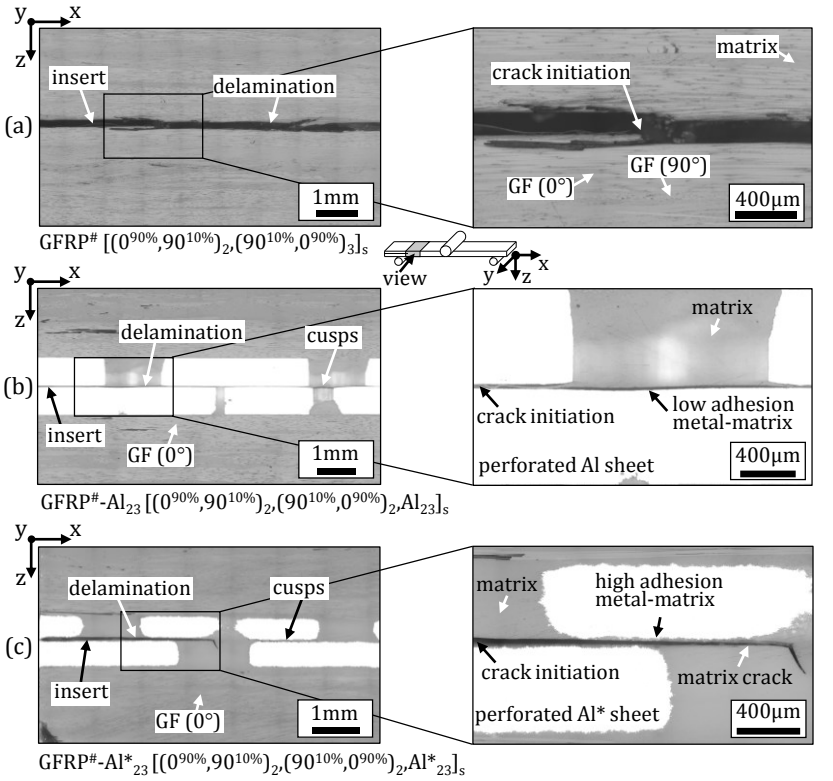

Figure 5.11: Optical microscopic edge view of representative specimens under ENF loading according to [39]: (a) GFRP#; (b) GFRP#-Al$_{23}$ with untreated Al plies; (c) GFRP#-Al*$_{23}$ with nanoscale sculptured Al* plies.

5.2 Model-based description of mechanical interlocking

Figure 5.12 depicts a schematic cross sectional illustration of a FML with nanoscale sculptured Al* plies. During the surface treatment an extremely high number of micrometer-sized cubical hook-like structures are formed with a structuring depth of ~ 30 µm as described in chapter 3.1.3. To better illustrate their working principle, the cubical structures are highly magnified (Figure 5.12). After polymer injection (by RTM) and curing, the cubical hook-like structures are completely enclosed by the matrix leading to a three-dimensional mechanical interlocking surface structure with highly improved interfacial strength of the Al*-matrix bond. Due to the extremely high number of cubical hook-like structures on the Al* ply surface, each hook-like structure has to transmit a relatively small normal and shear load to the bulk Al* ply. Therefore, the hook-like structures remain mechanically intact and adhere to the bulk Al* ply even under high and different load conditions. The failure of the FMLs occurs by cohesive matrix failure as well as delamination and IFFs between the GFs and the matrix, even without a triggering insert, due to a lower interfacial strength of the fibre-matrix bond compared to the Al*-matrix bond. This means that the inter-laminar properties of the FMLs are now entirely limited by the fibre-matrix bond of the base GFRP material and the cohesive strength of the matrix. Hence, without these limitations, the maximum normal and shear loads could be even higher.

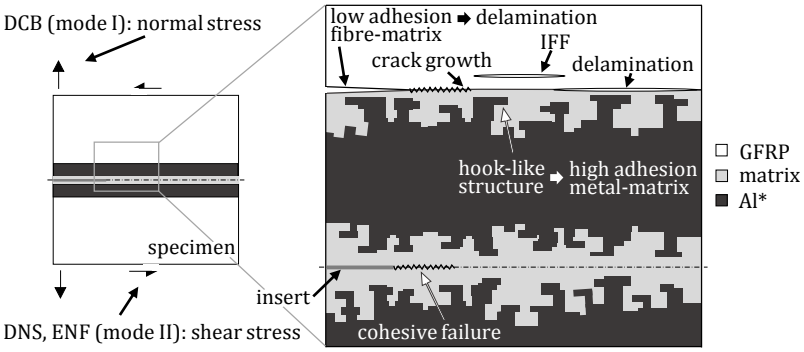

Figure 5.12: Schematic cross section of the different failure modes under normal and shear stress of a FML based on nanoscale sculptured Al* plies and GFRP layers according to [39].

5.3 Material constituents

Based on the testing results of the inter-laminar properties in chapter 5.1, the most promising constituents for the bearing capability and CAI are characterised under tension and compression. Table 5.2 shows the lay-up, fibre and metal volume fraction, and density of the laminates.

Table 5.2: Lay-up, fibre and metal volume fraction, and density of the laminates.

Laminate	Lay-up	V_f (%)	V_{Al^*} (%)	ρ (g/cm³)
GFRP	$[0_5]_s$	$48.3^{\pm 0.9}$	-	$1.82^{\pm 0.01}$
AA5754	[Al*]	-	$90.2^{\pm 2.1}$	-
AA6082	[Al*]	-	$65.1^{\pm 2.2}$	-

5.3.1 Tension/compression (longitudinal/transverse) of UD-GFRP

Figure 5.13 depicts the Young's modulus and maximum strength of UD-GFRP laminates under tension and compression in longitudinal and transverse direction. The first failure within the specimens under transverse tension (σ_{max} = 16.9±3.7 MPa) is dominated by the weakest link leading to IFFs of the composite. This failure mode depends mainly on the inter-ply bonding between the fibre-matrix and the defect distribution within the specimen volume. Hence, considering the size effect of transverse tensile specimens [135] the transverse tensile strength can be even higher.

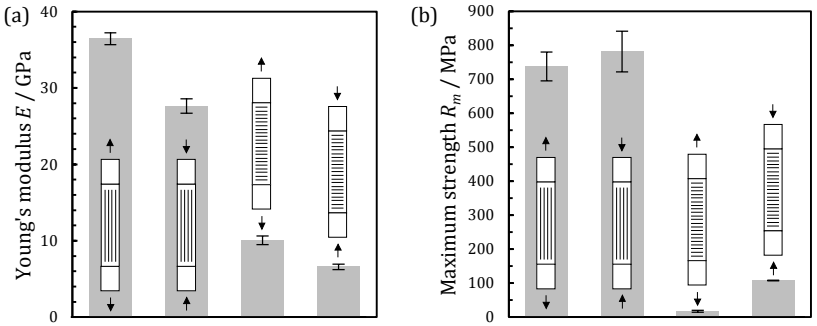

Figure 5.13: Tension and compression in longitudinal and transverse direction of UD-GFRP laminates; (a) Young's modulus; (b) Maximum strength.

The maximum longitudinal compression strength (σ_{max} = 781.7±64.1 MPa) is higher compared to the maximum longitudinal tensile strength (σ_{max} = 737.7±45.7 MPa). This phenomenon has also been observed with E-glass fibres in other literature [136].

5.3.2 Tension of nanoscale sculptured aluminium alloy sheets

Figure 5.14a demonstrates the tensile stress (σ)-strain (ε) response of representative nanoscale sculptured AA5754 and AA6082 specimens under tension. The curves increase monotonically (elastic region) up to this load where irreversible plastic deformation occur. The Young's modulus in 0°-loading direction (rolling direction of the sheets) for AA5754 and AA6082 are E = 73.17±1.66 GPa, E = 73.56±1.75 GPa, respectively. The transition between these regions (yield strength) is evaluated at 0.2 % strain. After reaching the maximum stress, the material constricts until the specimens finally fail, as indicated by the slight drop in the σ-ε curve. The elongation at fracture depends on the loading direction. The specimens in the 0°-loading direction show a higher fracture strain compared to the 90°-loading direction. All other mechanical properties are almost equal in both loading directions. The specimens AA5754 demonstrate the phenomenon of dynamic strain ageing (Portevin-Le Chatelier effect) [137], leading to continuous propagation with small stress drops.

Figure 5.14b depicts the mean and standard deviation of the yield and maximum tensile strength in 0°-loading direction of the AA5754 and AA6082 specimens. The values are evaluated considering the core cross section of the sheets (core section thickness is approximately 100 µm thinner compared to the outside thickness). The load transfer of the mechanical interlocking surface structure and matrix interphase is negligible small. The AA6082 shows drastically higher yield and maximum tensile strength compared to the AA5754 due to the greater proportion of the alloying element manganese and the post-processing of the alloy by precipitation hardening (T6). Hence, the results demonstrate a high potential using the nanoscale sculptured AA6082 for the impact, CAI, static and fatigue bearing response tests.

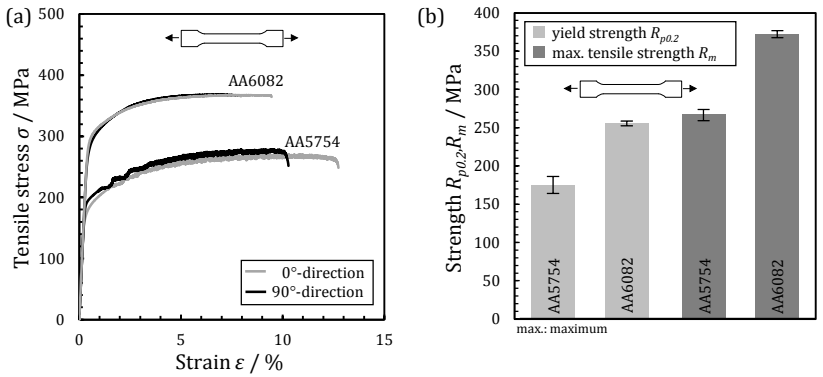

Figure 5.14: (a) Tensile stress-strain response of representative nanoscale sculptured AA5754 and AA6082 specimens under tension; (b) Mean and standard deviation of the yield and maximum tensile strength of nanoscale sculptured AA5754 and AA6082 specimens.

The inter-laminar properties (Chapter 5.1) of the nanoscale sculptured AA5754 results in promising interfacial bonding between the Al* and matrix. The SEM images (Figure 3.2c) of the AA6082 illustrate mostly the same interlocking surface structure as the AA5754 one. Hence, conducting additionally tests to determine the inter-laminar properties of the AA6082 has not been considered.

5.4 Impact behaviour

Table 5.3 shows the lay-up, fibre and metal volume fraction, and density of the laminates.

Table 5.3: Lay-up, fibre and metal volume fraction, and density of the laminates.

Laminate	Lay-up	V_f (%)	V_{Al^*} (%)	ρ (g/cm³)
GFRP	$[\pm45,90,0,\pm45,0,\pm45,0]_s$	$47.6^{\pm0.9}$	-	$1.82^{\pm0.01}$
GFRP-Al*	$[Al^*,0_2,Al^*,0]_s$	$24.0^{\pm0.3}$	$54.1^{\pm3.1}$	$2.29^{\pm0.05}$

5.4.1 Low-velocity impact

The contact load (P)-time (t) response, corresponding absorbed energy (E_a) and impactor displacement (δ) of representative GFRP and GFRP-Al* specimens under low-velocity impact loading are shown in Figure 5.15.

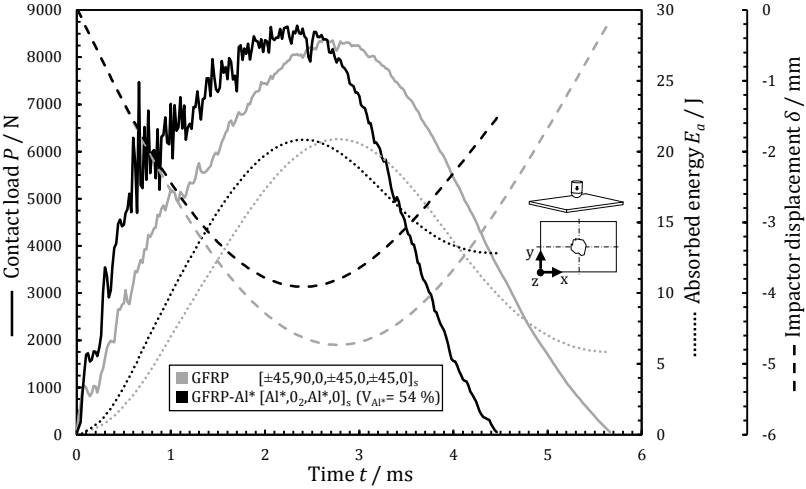

Figure 5.15: Contact load-time response, corresponding absorbed energy and impactor displacement of representative GFRP and GFRP-Al* specimens under low-velocity impact loading according to [40].

During the initial time of the contact period the typical behaviour is observed. The GFRP laminate leads to first failures at a contact load of $P \approx 1000$ N ($t \approx 0.1$ ms). First failure within the GFRP-Al* laminate occurs

delayed due to the ductility of the metal sheets ($P \approx 1750$ N, $t \approx 0.12$ ms). Both laminates show a decrease and fluctuation of the load up to $t \approx 2.8$ ms and a smooth curve thereafter. This is due to the occurrence of failures such as delamination at the fibre-matrix interfaces as well as IFFs (Figure 5.16), which decreases the local bending stiffness of the laminates in the impact area. The GFRP-Al* laminates lead to a slightly higher maximum contact load compared to the GFRP. The load drops to zero and the impactor displacement becomes equal to the plastic deformation in the dent. Due to the extensively higher plastic deformation (Figure 5.15, impactor displacement-time curve) of the GFRP-Al* laminates (up to 9 times), the absorbed energy is higher (~ 120 %) in comparison to the GFRP ones.

The GFRP laminate exhibits the typical damage behaviour under a low-velocity impact resulting in a truncated pyramid pattern due to IFFs and delamination (Figure 5.16a). The GFRP-Al* demonstrates similar failure modes. The absorbed energy results in significant delamination between the Al* sheets, especially on the non-impacted side. However, all parts of the interfacial bonding between the nanoscale sculptured Al* and the matrix remain intact, exhibiting a high interfacial metal-matrix strength of the GFRP-Al* under impact loading (Figure 5.16b).

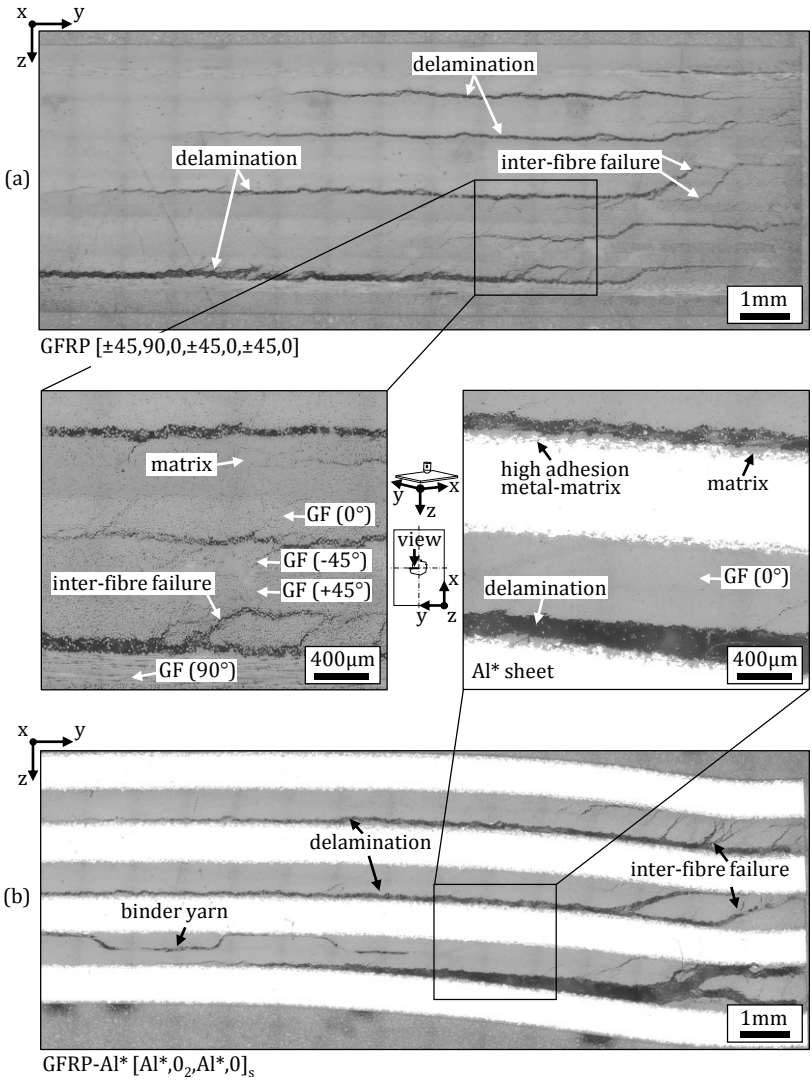

Figure 5.16: Optical microscopic edge view of representative specimens under low-velocity impact loading according to [40]: (a) GFRP and (b) GFRP-Al*.

5.4.2 Compression after impact

The compressive residual stress (σ^{CAI})-strain (ε^{CAI}) response of representative GFRP and GFRP-Al* specimens as well as the compressive residual strength of all specimens under CAI loading are illustrated in Figure 5.17a and Figure 5.17b, respectively. In the initial stage of loading, all laminate curves show a nonlinear behaviour, mainly due to self-aligning processes between the test fixture and specimen. Afterwards, the curves increase linearly up to the load where first failures (GFRP) and plastic deformation (GFRP-Al*) in the laminate occur resulting in degradation of the composite.

The specimens fail after reaching the maximum loading. The GFRP-Al* laminates demonstrate higher specific compressive residual strength (~ 9 %), compared to the GFRP ones. The optical microscopic edge view (GFRP-Al*) shows drastically high bonding of the Al*-matrix interface (Figure 5.18). Further description of the failure modes can be found in chapter 5.6.5.

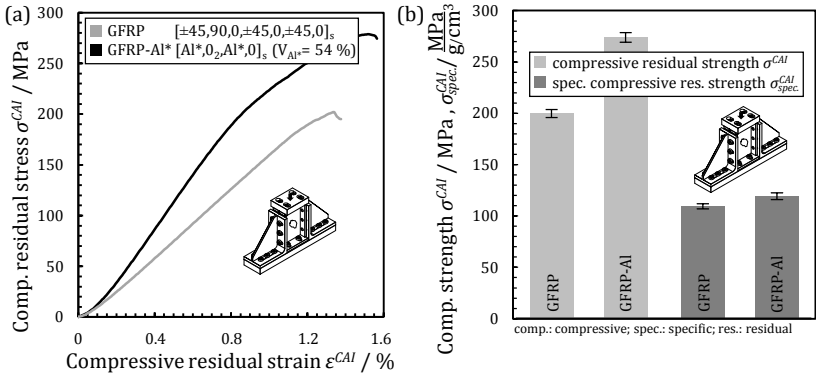

Figure 5.17: (a) Compressive residual stress-strain response of representative GFRP and GFRP-Al* specimens under CAI loading; (b) Compressive residual strength of all GFRP and GFRP-Al* specimens according to [40].

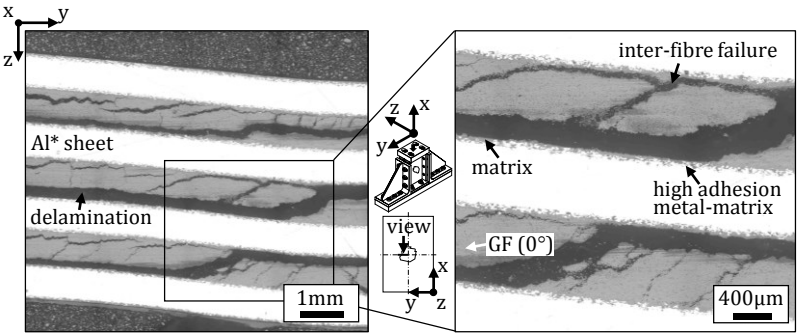

GFRP-Al* $[Al^*,0_2,Al^*,0]_s$

Figure 5.18: Optical microscopic edge view of a representative GFRP-Al* specimen under CAI loading according to [40].

5.5 Bearing response

Table 5.4 shows the lay-up, fibre and metal volume fraction, and density of the laminates under static and fatigue pin- and bolt-loaded bearing.

Table 5.4: Lay-up, fibre and metal volume fraction, and density of the laminates.

Laminate	Lay-up	V_f (%)	V_{Al^*} (%)	ρ (g/cm^3)
GFRP	$[\pm 45_2, 0_2, \pm 45, 90, 0]_s$	$49.3^{\pm 0.5}$	-	$1.85^{\pm 0.01}$
GFRP-Al*$_{45}$	$[Al^*, 0_2, Al^*, 0]_s$	$25.0^{\pm 0.2}$	$44.7^{\pm 0.4}$	$2.20^{\pm 0.05}$
GFRP-Al*$_{49}$	$[Al^*, 0_2, Al^*, 0]_s$	$24.7^{\pm 0.1}$	$48.6^{\pm 0.2}$	$2.26^{\pm 0.04}$
GFRP-Al*$_{52}$	$[Al^*, 0_2, Al^*, 0]_s$	$24.5^{\pm 0.4}$	$52.2^{\pm 1.2}$	$2.31^{\pm 0.06}$

5.5.1 Static pin- and bolt-loaded bearing

The bearing stress (σ^{br})-strain (ε^{br}) response of representative GFRP and GFRP-Al*$_{52}$ specimens under static pin- and bolt-loaded (1,4,8 Nm) bearing as well as the bearing strength (2 % hole expansion) of all GFRP and GFRP-Al* specimens under static pin- and bolt-loaded (1,4,8 Nm) bearing is shown in Figure 5.19a and Figure 5.19b, respectively. All laminates fail by bearing.

The non-uniform distribution of the bearing pressure generates compression and interlaminar shear stresses within the laminate. In the initial stage of loading, all laminates are non-linear, mainly due to the self-aligning processes between the test fixture and the specimen as well as between the pin/bolt and the hole. Subsequently, the curves increase linearly up to the load where first failures in the material structure occur resulting in degradation of the composite.

The pin-loaded GFRP laminate (Figure 5.19a) demonstrates a substantial sudden load drop after reaching the maximum bearing strength indicating significant failure phenomena. As shown in Figure 5.20a, IFFs in the ±45°-GFRP layers and delamination between the 0°/±45°-GFRP outer layers occur leading to kink-band formation. Under pin-loaded bearing, delamination seems to be the dominant failure mode.

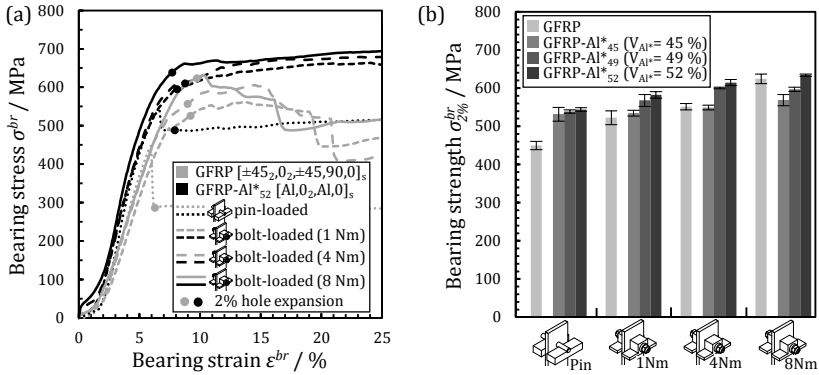

Figure 5.19: (a) Bearing stress-strain response of representative GFRP and GFRP-Al*$_{52}$ specimens under static pin- and bolt-loaded (1,4,8 Nm) bearing according to [40]; (b) Bearing strength (2 % hole expansion) of all GFRP and GFRP-Al* specimens under static pin- and bolt-loaded (1,4,8 Nm) bearing according to [40].

Lee et al. [138] detected that the outer layers (mostly ±45°/90°) provide lateral support to the 0°-layers under compression that reduce the stress concentration, as a result, it delays the initiation of fibre buckling.

However, the stiff Al* sheets, within the pin-loaded GFRP-Al* laminates, provide much higher lateral support to the 0°-GFRP layers, preventing significant expansion under compression and delamination (Figure 5.20b). Furthermore, the stiff Al* sheets also take up more compression stress compared to the ±45°-GFRP outer layers, resulting in lower kink-band formation in the 0°-GFRP layers. Both leads to an increased ultimate bearing strength compared to the GFRP. After reaching the 2 % hole expansion, the Al* sheets show buckling and plastic deformation.

Under bolt-loaded bearing (1, 4 Nm), the GFRP laminates fail due to IFFs of the ±45°-GFRP outer layers outside the washers causing delamination and kink-band formation (Figure 5.21a, Figure 5.22a). The GFRP-Al* laminates under bolt-loaded bearing (1, 4 Nm) exhibit lower delamination and kink-band formation due to the stiff Al* sheets (Figure 5.21b, Figure 5.22b). After reaching the 2 % hole expansion, the Al* sheets show slight buckling and plastic deformation.

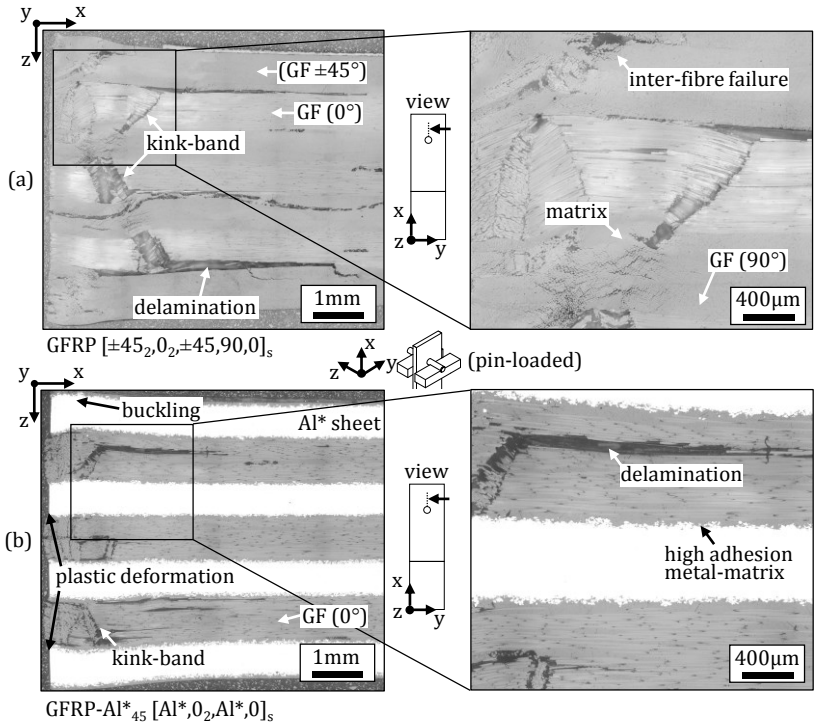

Figure 5.20: Optical microscopic edge view of representative specimens under static pin-loaded bearing according to [40]: (a) GFRP and (b) GFRP-Al*$_{45}$.

The bolt-loaded (8 Nm) GFRP laminate shows the first load drop after reaching the 2 % hole expansion (Figure 5.19a) due to progressive kink-band formation (Figure 5.23a). Here, the IFF of the ±45°-GFRP outer layers outside the washers are suppressed by the high lateral support (8 Nm). The bolt-loaded (8 Nm) GFRP-Al* laminate shows further load increase after reaching the 2 % hole expansion (Figure 5.19a) due to the suppressed buckling of the Al* sheets by the high lateral support (8 Nm) and the significant lower kind-band formation due to the stiff Al* sheets (Figure 5.23b).

The optical microscopic edge view results (Figure 5.20b-Figure 5.23b) demonstrate for all FMLs that the adhesive bond between the nanoscale sculptured Al* sheets and the matrix remains intact and is strong enough to

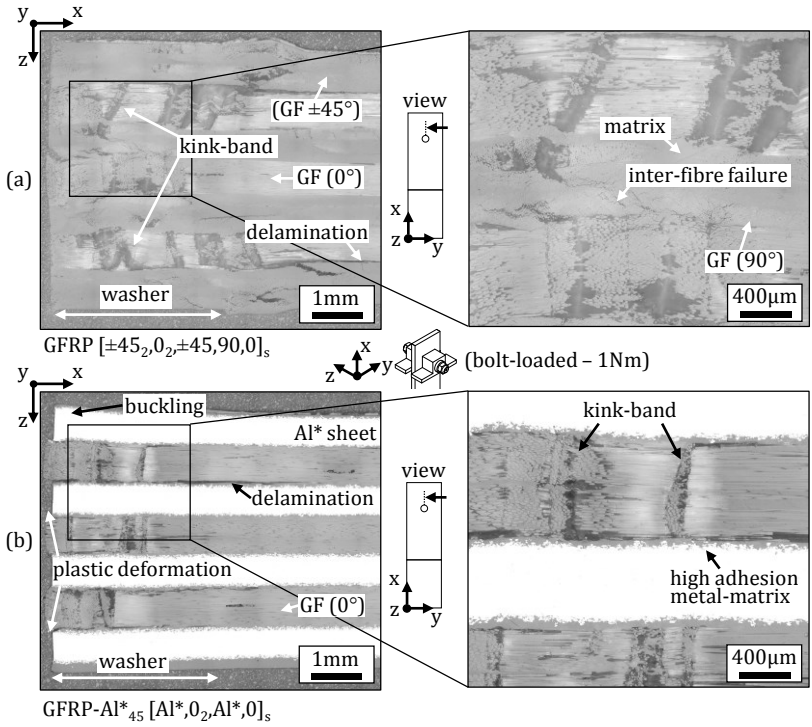

Figure 5.21: Optical microscopic edge view of representative specimens under static bolt-loaded (1 Nm) bearing according to [40]: (a) GFRP and (b) GFRP-Al*$_{45}$.

withstand the normal and shear stress in the interface of the stepped lap bonded joint. As a result, the premature delamination and catastrophic failure is prevented. These failures commonly occur in conventional FMLs with insufficient metal-matrix adhesion.

This strongly improved mechanical behaviour can be understood in terms of the mechanical interlocking surface structure of the Al* sheets. This surface structure ensures such a high interfacial strength between the nanoscale sculptured Al* surface and the matrix that delamination occurs only at the GF-matrix interface.

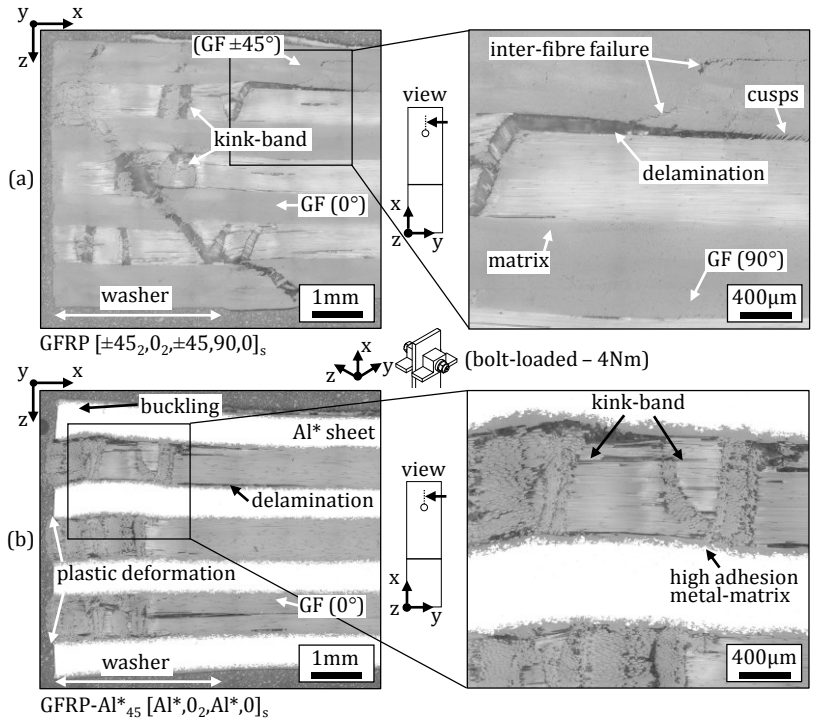

Figure 5.22: Optical microscopic edge view of representative specimens under static bolt-loaded (4 Nm) bearing according to [40]: (a) GFRP and (b) GFRP-Al*$_{45}$.

For both, pin- and bolt loading, the FML structures are still able to sustain a significant load when deformations are imparted well beyond the 2 % hole expansion. However, the bearing behaviour in case of bolted joints exhibits a significant difference in comparison to the pin-loaded ones. The washers of the bolted joints lead to a substantial lateral support under compression preventing lateral expansion, and thus delaying the development of delamination. Consequently, the bolt-loaded bearing strength increases with higher bolt torque (8 Nm) up to 39 % for GFRP and up to 17 % for GFRP-Al*$_{52}$ (V_{Al}* ≈ 52 %) in comparison to pin-loaded bearing (Figure 5.19b).

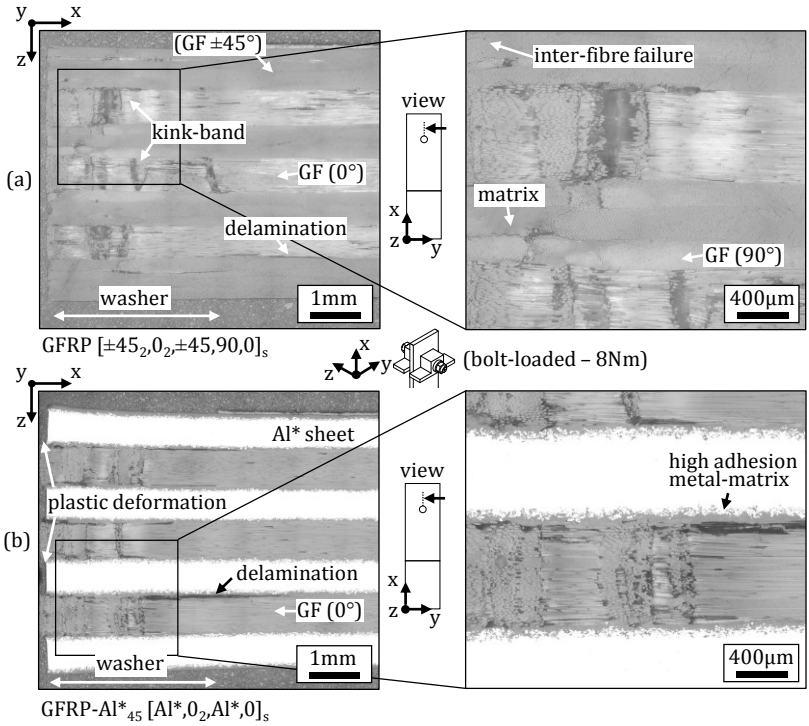

Figure 5.23: Optical microscopic edge view of representative specimens under static bolt-loaded (8 Nm) bearing according to [40]: (a) GFRP and (b) GFRP-Al*$_{45}$.

The stiff Al* sheets absorb higher compression stress compared to the biaxial GFRP layers resulting in bearing strength (for GFRP-Al*$_{52}$) up to approximately 21 % higher for pin-loaded, 11 % for bolt-loaded (1 Nm), 12 % for bolt-loaded (4 Nm), and 2 % for bolt-loaded (8 Nm) in comparison with the GFRP laminate (Figure 5.19b). The influence of the lateral support of the Al* sheets to the 0°-GFRP layers is minimised by increasing the bolt torque. The bolt-loaded bearing strengths demonstrate an almost linear behaviour with increasing metal volume fraction resulting in substantial improvements of the ultimate bearing strength. Under pin-loaded bearing, the metal volume fraction seems to have a minor influence on the bearing strength.

5.5.2 Fatigue pin- and bolt-loaded bearing

The bearing stress-cycles till 2 % hole expansion of the GFRP and GFRP-Al* specimens under fatigue pin-loaded bearing is illustrated in Figure 5.24a. Both laminates show bearing failure even until 15-20 % hole expansion. Consequently, the width to diameter (w/d) ratio can be reduced under pin-loaded bearing. The GFRP-Al* laminates show significantly higher resistance to fatigue compared to the GFRP laminate. At 60 % of the static maximum (s.m.) pin-loaded bearing ($\sigma^{br}_{2\%,max}$ = 544 MPa), the fatigue life improvement of the GFRP-Al* (for 2 % hole expansion) is in excess of over $1{\cdot}10^4$ % in comparison to the GFRP (60 % s.m.). Even at higher loads (80 % s.m.), the fatigue life of the GFRP-Al*$_{52}$ is still ~ 1300 % higher compared to the GFRP (60 % s.m.). The resistance to fatigue increases significantly with increasing metal volume fraction. $2{\cdot}10^6$ cycles is considered as criterion for test run-out, indicated by the arrows in the graphs. The optical microscopic edge view of a representative GFRP-Al*$_{45}$ specimen at 70 % s.m. (stopped at $1{\cdot}10^6$ cycles) is shown in Figure 5.25. The failure modes are similar to the static bearing loading ones resulting in high interfacial strength of the nanoscale sculptured Al*-matrix bond.

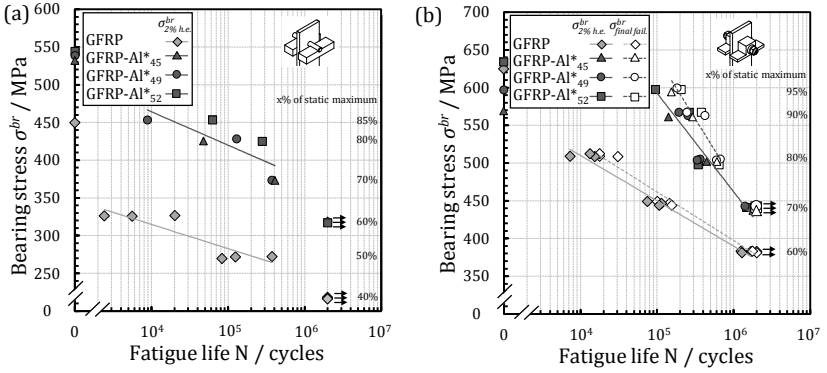

Figure 5.24: Bearing stress-cycles till 2 % hole expansion (h.e.) as well as till final failure (fail.) of GFRP and GFRP-Al* specimens under fatigue (a) pin-loaded bearing according to [40]; (b) bolt-loaded (8 Nm) bearing according to [40]; criterion for test run-out is indicated by arrows in the graphs.

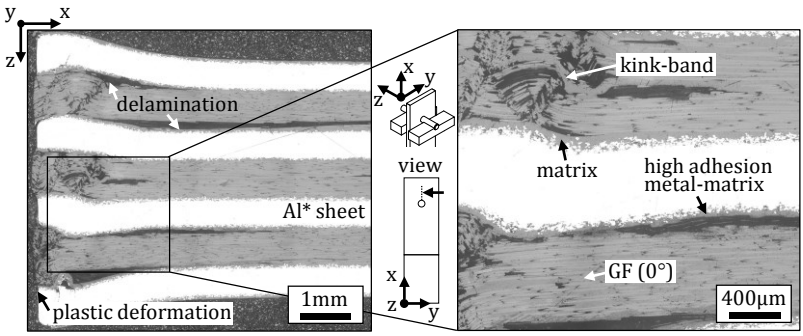

Figure 5.25: Optical microscopic edge view of a representative GFRP-Al*$_{45}$ specimen (70 % s.m., stopped at 1·10^6 cycles) under fatigue pin-loaded bearing according to [40].

Figure 5.24b shows the bearing stress-cycles till 2 % hole expansion as well as till final failure of the GFRP and GFRP-Al* specimens under fatigue bolt-loaded (8 Nm) bearing.

The GFRP-Al* laminates show drastically higher resistance to fatigue compared to the GFRP (Figure 5.24b). All laminates, the GFRP and GFRP-Al*, show bearing failure until ~ 3-4 % hole expansion. After further cycles, the GFRP specimens fail mostly by shear-out and the GFRP-Al* by cleavage. At 70 % and 80 % of the s.m. bolt-loaded bearing ($\sigma_{2\%}^{br}$ = 634 MPa), the fatigue life improvement of the GFRP-Al* (for 2 % hole expansion) is in excess of over 1300 % and 2800 % in comparison to the GFRP. Even at higher loads (90 % s.m.), the fatigue life of the GFRP-Al*$_{52}$ is still ~ 1600 % higher compared to the GFRP (80 % s.m.). The GFRP-Al*$_{45}$ at 95 % s.m. resulted in a hole expansion of ~ 1 % after 10, ~ 2 % after 100, and ~ 2.5 % after 1000 cycles. The final failure occurs at ~ 1.55·10^5 cycles. The resistance to fatigue increases slightly with increasing metal volume fraction. The optical microscopic edge views of representative GFRP specimens at 60 % s.m. (stopped at 2·10^6 cycles) and GFRP-Al*$_{49}$ 70 % s.m. (stopped at 2·10^6 cycles) are illustrated in Figure 5.26a and Figure 5.26b, respectively. They indicate high bonding between the nanoscale sculptured Al* surface and the matrix. The failure modes are similar to the static bearing loading ones (chapter 5.5.1).

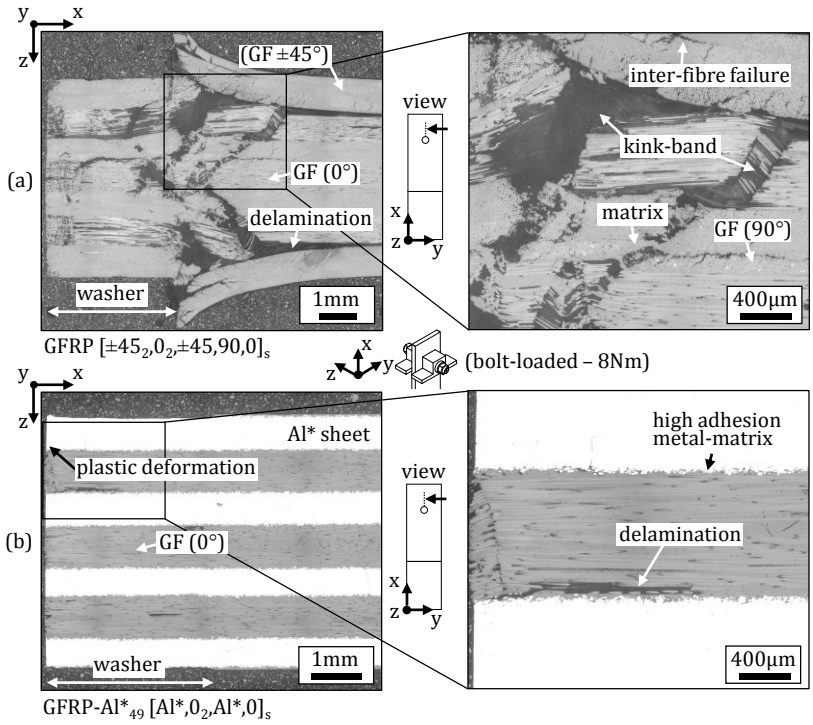

Figure 5.26: Optical microscopic edge view of representative specimens under fatigue bolt-loaded (8 Nm) bearing according to [40]: (a) GFRP (60 % s.m., stopped at $2 \cdot 10^6$ cycles) and (b) GFRP-Al*$_{49}$ (70 % s.m., stopped at $2 \cdot 10^6$ cycles).

Passive thermography of all specimens under fatigue pin- and bolt-loaded bearing results in negligible temperature increase (< 5 °C) during loading.

5.6 Health monitoring

To demonstrate the potential of the health monitoring method using the capacitance measurement DCB (5.6.1) and ENF (5.6.2) tests are conducted. Therefore, two thin WMFs (St_{p28}) are laid-up in both laminates to locate the crack growth by measuring the capacitance change between the two metal plies. In the first laminate (GFRP-WMF $[0_5,St_{p28},0]_s$), the crack growth between the GFRP-GFRP layers is observed. In the second laminate (GFRP-WMF-Al* $[0_3,St_{p28},0_2,Al^*_{p0,AA5754},0_2,St_{p28},0_3]$), one surface structured metal sheet (AA5754) is added in the mid plane to observe the crack growth between the Al*-GFRP layers, resulting in a slight asymmetry.

For the subsequent mechanical testing of the FMLs under tension (5.6.3), low-velocity impact (5.6.4), CAI (5.6.5), and static pin-loaded bearing (5.6.6) with in-situ health monitoring the integral Al sheets act as the sensors.

5.6.1 Double cantilever beam (DCB)

The testing results demonstrate that the capacitance significantly decreases due to crack growth between the GFRP layers. Figure 5.27 shows the load-crack opening response and corresponding capacitance measurement of a representative GFRP-WMF $[0_5,St_{p28},0]_s$ specimen. The variation of capacitance is normalised to the initial capacitance (C_0 = 137.5 pF).

For all investigated specimens, the capacitance decreases rapidly in the beginning until crack initiation and afterwards nearly linear with increasing crack growth. Sharp drops in the load-crack opening graphs result in observable capacitance variations. Changing the distance (d) and/or the relative static permittivity (ε_r) of the metal plies during the mechanical testing changes the capacitor geometry, which influences the capacitance. Separating the metal plies by crack opening (δ) increases the distance (d) and decreases the relative static permittivity due to air between the layers ($\varepsilon_{r,air} \approx 1$, $\varepsilon_{r,GFRP} \approx 5\text{-}8$).

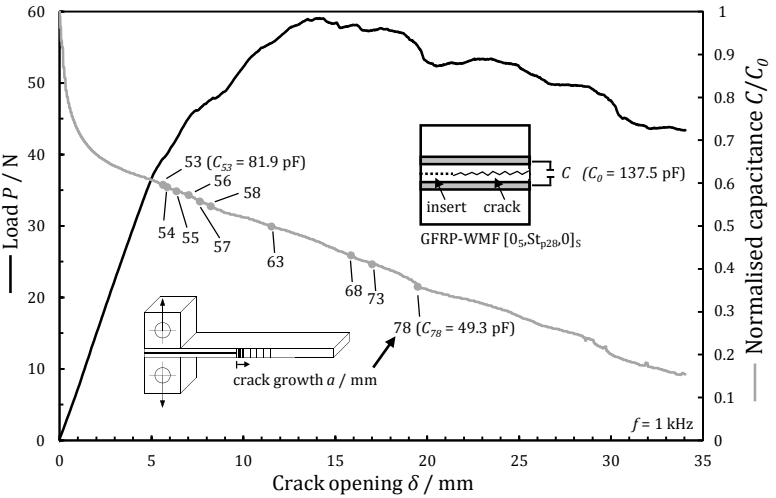

Figure 5.27: Load-crack opening response and corresponding normalised capacitance measurement of a representative GFRP-WMF specimen under DCB loading according to [38]; numbers indicate crack growth.

Further measurements demonstrate that the capacitance is significantly dominated by the undamaged portion of the specimen (Figure 5.28). The capacitive outcome decreases rapidly to nearly zero in the area of delamination. Measuring the capacitance of an undamaged part of a specimen with a length of L = 62 mm (corresponds to a crack of a = 53 mm) and L = 37 mm (corresponds to a = 78 mm) leads to a capacitance of C (a = 53 mm) = 79.3 pF and C (a = 78 mm) = 47.5 pF. The actual capacitance (Figure 5.27) is C (a = 53 mm) = 81.9 pF and C (a = 78 mm) = 49.3 pF. This corresponds to an error deviation of <4 %. The discrepancy is the sum of the capacitive outcome in the area of delamination, measuring deviations, manufacturing and material variations.

The mechanical tests demonstrate, that the GFRP-WMF-Al* laminates [0$_3$,St$_{p28}$,0$_2$,Al*$_{p0,AA5754}$,0$_2$,St$_{p28}$,0$_3$] tend towards a crack growth between the GF-matrix interface, resulting in similar results for the capacitance measurement C_1 to the GFRP-WMF laminates.

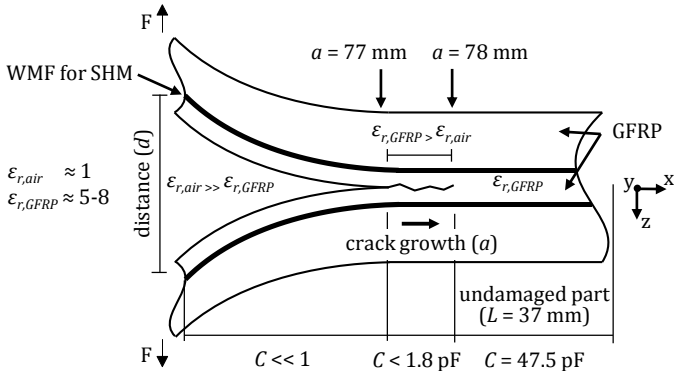

Figure 5.28: Schematic crack growth compared to the capacitive outcome of a DCB specimen according to [38].

Double cracking or crack jumping to the other metal side do not occur, resulting in a constant capacitance C_2 (aside from insignificant measuring deviations) for all GFRP-WMF-Al* specimens. The GFRP-WMF (Figure 5.27) and GFRP-WMF-Al* laminates show linear behaviour up to a point where the delamination front in the mid plane starts to grow (crack initiation). The laminates display sharp drops in the *P-δ* graphs, which indicate unstable crack growth. Afterwards, the load-crack opening curves increase up to a maximum value due to fibre bridging.

Figure 5.29 shows the SEM images of the laminates after testing. The fracture surface analyses show smooth fibres with low matrix particle fractions implying low interfacial strength of the fibre-matrix bond, resulting in early adhesive failure and ply delamination. The inter-laminar bond between the pre-treated Al* ply with cubical hook-like structures after nanoscale sculpturing, within the GFRP-WMF-Al* composites, is strong enough to withstand the normal stress during DCB (mode I) loading in the interface. Hence, delamination appears away from the metal-matrix interface in the transition zone between GF and matrix due to the lower adhesion of the GF-matrix interface (Figure 5.29b,c).

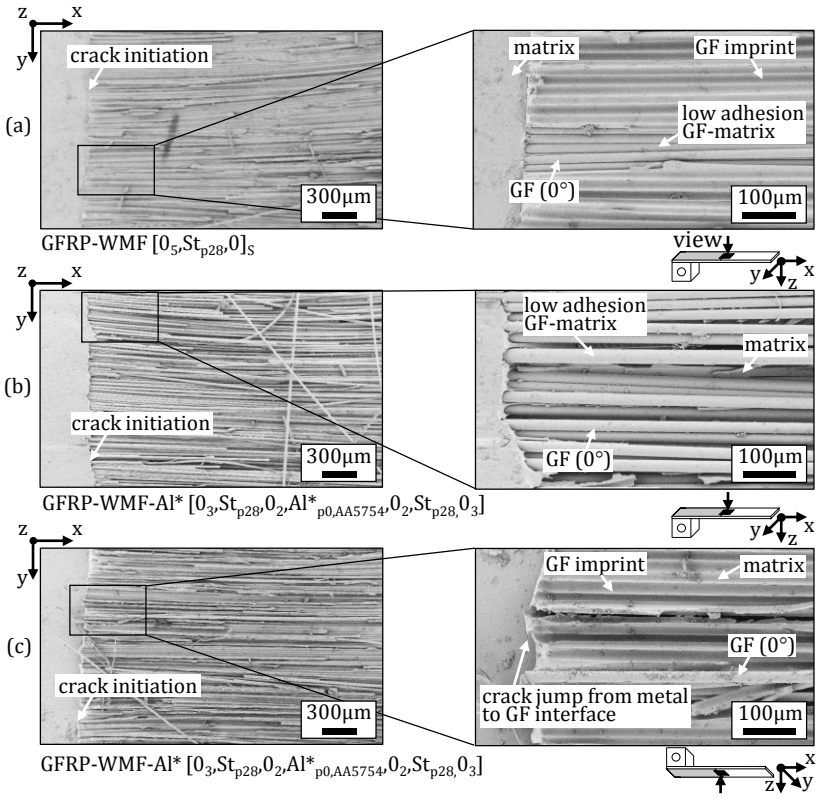

Figure 5.29: SEM images of representative specimens under DCB loading according to [38]: (a) GFRP-WMF; (b) GFRP-WMF-Al* (lower side); (c) GFRP-WMF-Al* (upper side).

All laminates display a rising R-curve behaviour since the energy release rate (G_{DCB}^{total}) increases with crack growth (Figure 5.30). The GFRP-WMF and GFRP-WMF-Al* laminates show an almost equal energy release rate at crack initiation by reason that within both laminates crack growth appears between the GF-matrix interface. The capacitance decreases nearly linearly with increasing crack growth. Changes in the energy release rate result in observable capacitance variations.

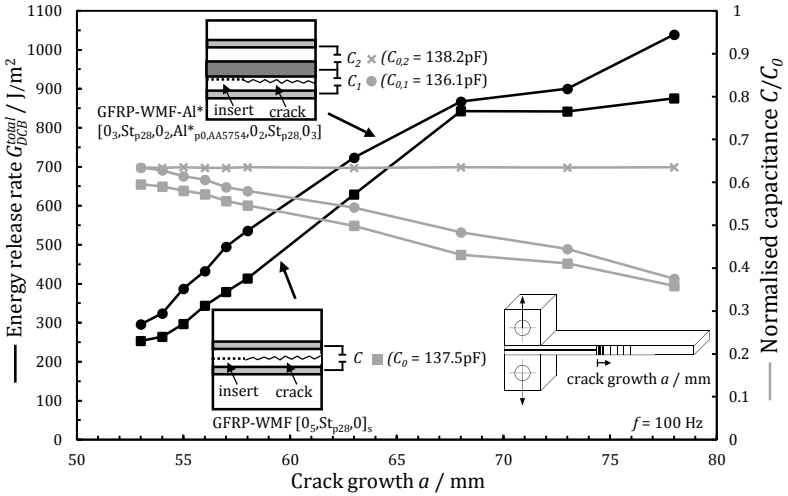

Figure 5.30: Energy release rate-crack growth and corresponding normalised capacitance measurement of representative GFRP-WMF and GFRP-WMF-Al* specimens under DCB loading according to [38].

The initiation delamination toughness of the GFRP-WMF laminates is $G_{DCB,init.}^{total}$ = 259±36 J/m². The GFRP-WMF-Al* laminates show a similar toughness of $G_{DCB,init.}^{total}$ = 267±31 J/m². Due to the slight asymmetric lay-up of the GFRP-WMF-Al* laminates the crack growth is off the mid plane and leads to a mix of the fracture mode I/II at the crack tip. Calculating the mode-mixity [84] results in $G_{II}/G_{total} \approx 3\%$. The thermal influence of residual stresses [89] due to the different material properties is considered leading to negligible contribution to the test values.

5.6.2 End-notched flexure (ENF)

Figure 5.31 depicts the load-displacement response and corresponding capacitance measurement (f = 100 Hz, 1 kHz) of representative GFRP-WMF $[0_5,St_{p28},0]_s$ specimens. The variation of capacitance is normalised to the initial capacitance of each specimen. The results obtained demonstrate that the capacitance significantly decreases due to crack growth between the GF-matrix interface. The composites fail by reaching the maximum inter-laminar shear stress. The load-displacement response appears nearly linear until reaching maximum loading, the SHM method presents observable capacitance decreases already after a loading of approximately F = 150-250 N. After reaching the maximum applied load the capacitance decreases rapidly with increasing crack growths.

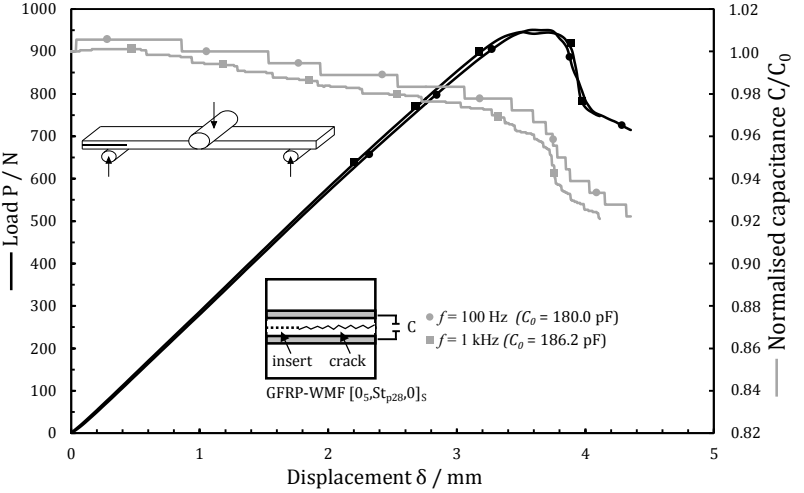

Figure 5.31: Load-displacement response and corresponding normalised capacitance measurement of representative GFRP-WMF specimens under ENF loading according to [38].

Figure 5.32 shows the load-displacement response, corresponding capacitance measurement (f = 100 Hz) and the micrograph of a representative GFRP-WMF specimen after ENF loading (F_{max} = 800 N). The load-displacement response and corresponding capacitance measurement are similar to the results of the specimens in Figure 5.31. Even though the load-displacement response looks linear the crack, starting from the insert, has in fact already started to propagate (micrograph, Figure 5.32). In this context it is important to point out, that even very small crack growth, occurring between the GF-epoxy interface, can be electrically detected with the capacitance measurements.

Figure 5.33 presents the load-displacement response and corresponding capacitance measurement (f = 100 Hz) of a representative GFRP-WMF-Al* [0_3,St_{p28},0_2,$Al^*_{p0,AA5754}$,0_2,St_{p28},0_3] specimen. The results show, that GFRP-WMF-Al* laminates tend also towards crack growth between the GF-matrix interface, resulting in similar results to the GFRP-WMF laminates, as seen for DCB loading.

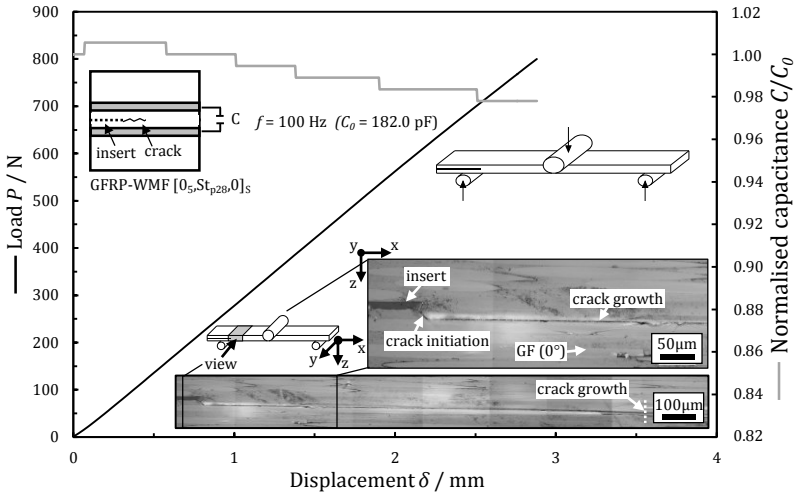

Figure 5.32: Load-displacement response, corresponding normalised capacitance measurement and micrograph of a representative GFRP-WMF specimen under ENF loading according to [38].

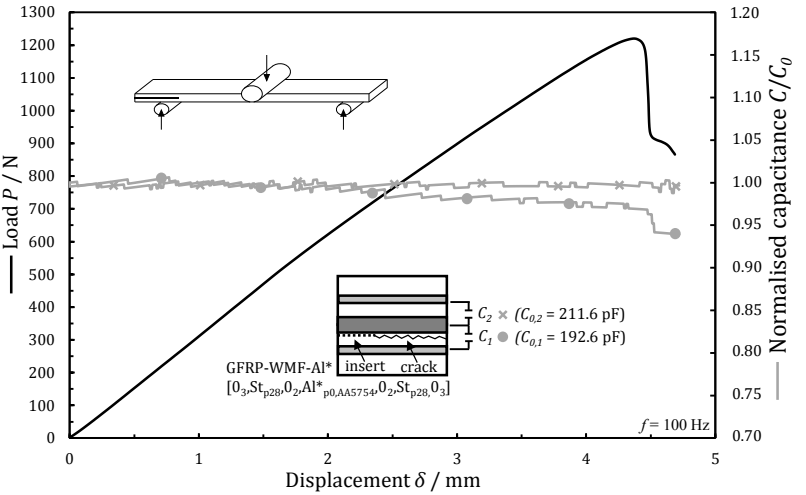

Figure 5.33: Load-displacement response and corresponding normalised capacitance measurement of a representative GFRP-WMF-Al* specimen under ENF loading according to [38].

The capacitance C_1 decreases with increasing crack growth and the capacitance C_2 is constant (aside from insignificant measuring deviations) for all GFRP-WMF-Al* specimens. During loading, the capacitor geometry changes slightly, resulting in a negligible influence on the capacitance measurement.

Figure 5.34 and Figure 5.35 depict the optical microscopic edge view and SEM images of representative GFRP-WMF and GFRP-WMF-Al* specimens after testing. Shear deformation triggers fracturing by a debonding at the GF-matrix interface and the formation of cusps causing ply delamination. The mechanisms of cusp formation are illustrated in Figure 5.34b. The fracture surfaces show very low presence of matrix adherence implying low interfacial strength of the fibre-matrix bond, resulting in early adhesive failure. The GFRP-WMF-Al* composite images in Figure 5.35 show that the inter-laminar bond between the three-dimensional mechanical interlocking surface structures of the Al* ply is strong enough to withstand the shear stress in the interface.

The cubical hook-like structures are completely enclosed by the matrix forming a very stable connection between the Al* ply and the matrix. Hence, delamination appears away from the Al*-matrix interface in the transition zone between the GF-matrix due to the lower adhesion of the GF-matrix interface. This behaviour is representative for all GFRP-WMF-Al* specimens investigated in this study.

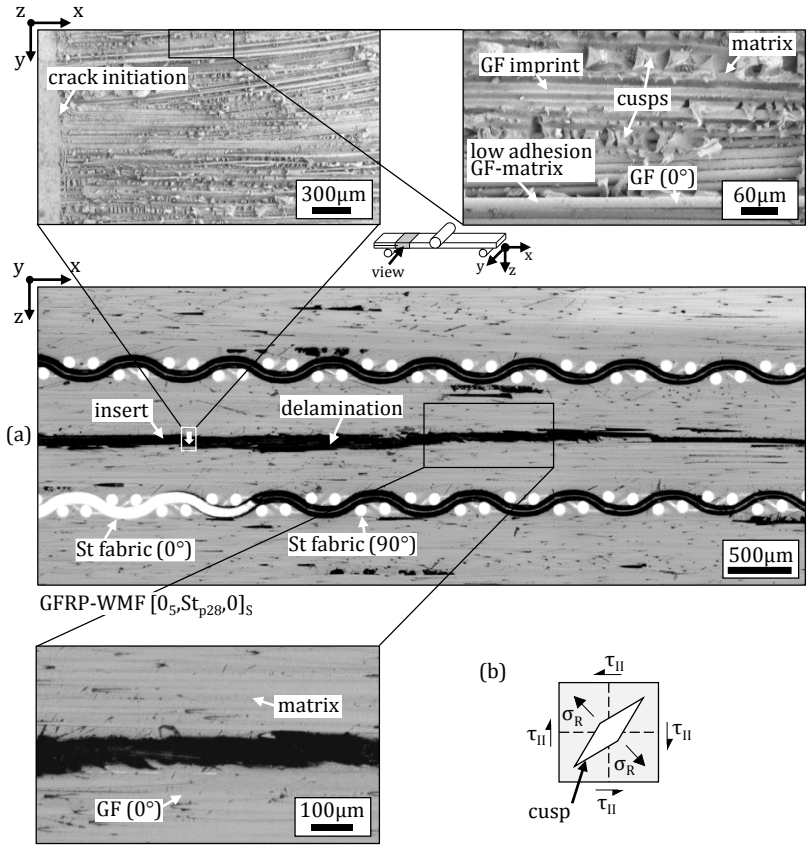

Figure 5.34: (a) Optical microscopic edge view and SEM images of a representative GFRP-WMF specimen under ENF testing according to [38]; (b) Mechanisms cusp formation according to [132] .

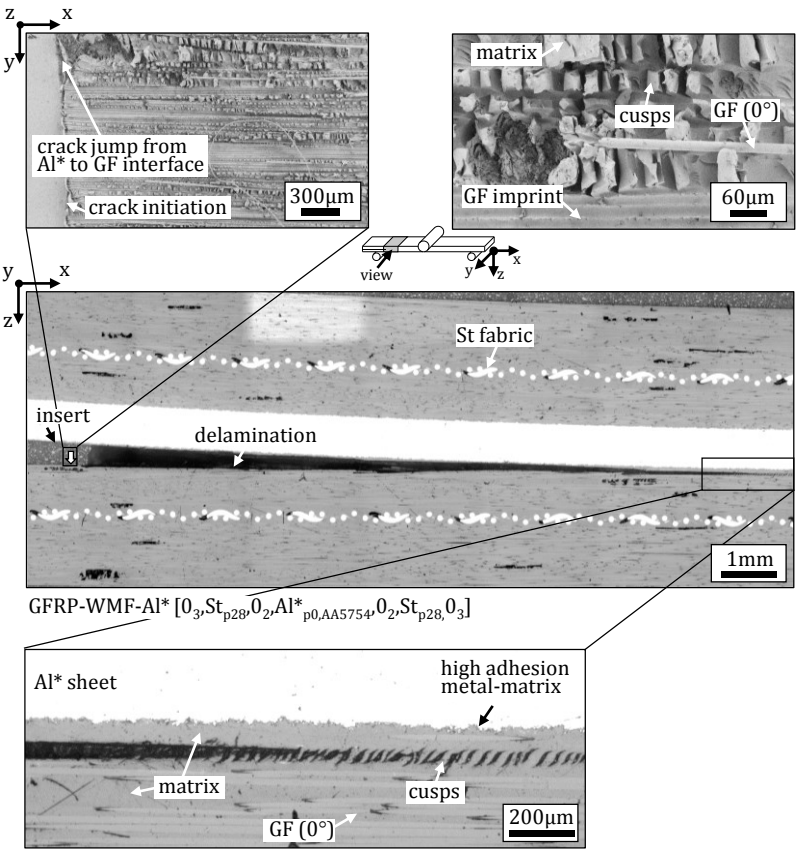

Figure 5.35: Optical microscopic edge view and SEM images of representative GFRP-WMF-Al* specimens under ENF testing according to [38].

The average value of the energy release rate of the GFRP-WMF laminates is G_{ENF}^{total} = 1952±181 J/m². The GFRP-WMF-Al* laminates show similar results with G_{ENF}^{total} = 1963±52 J/m². Due to the slight asymmetric lay-up of the GFRP-WMF-Al* laminates the inter-laminar fracture toughness leads to a mode-mixity at the initial crack tip with insignificant contribution of G_I/G. The thermal influence of residual stresses [134] due to the different material properties is considered leading to negligible contribution to the test values.

5.6.3 Tension of GFRP with stepped lap metal sheets

Figure 5.36 shows the tensile stress (σ)-strain (ε) response, corresponding cumulative AE energy (E_{AE}) and normalised capacitance (C/C_0) of a representative GFRP specimen with stepped lap metal sheets under tension. The cumulative AE energy increases in the beginning to $E_{AE} \approx 2.2$ µJ due to first IFFs. Afterwards, the cumulative AE energy increases slowly. At about $\varepsilon \approx 1.5$ % the AE energy starts to rise exponentially until the AE energy hits $E_{AE} \approx 18.1$ µJ at final failure due to IFFs, fibre fractures, and delamination. The capacitance shows a slightly increase during tension due to the transverse contraction of the components, which decreases the specimen thickness and thus the distance between the Al* sheets. Shortly before final failure (at about $\varepsilon \approx 1.85$ %, $\sigma \approx 460$ MPa) delamination occurs on the FRP side (illustration in Figure 5.36) as well as between the outer Al* sheets and the composite on the FMLs side (Figure 5.37a). However, the optical microscopic edge views shortly before and after final failure show a high adhesion of the Al*-matrix interface resulting in fibre-matrix debonding (Figure 5.37a,b). The capacitance decreases drastically after final failure.

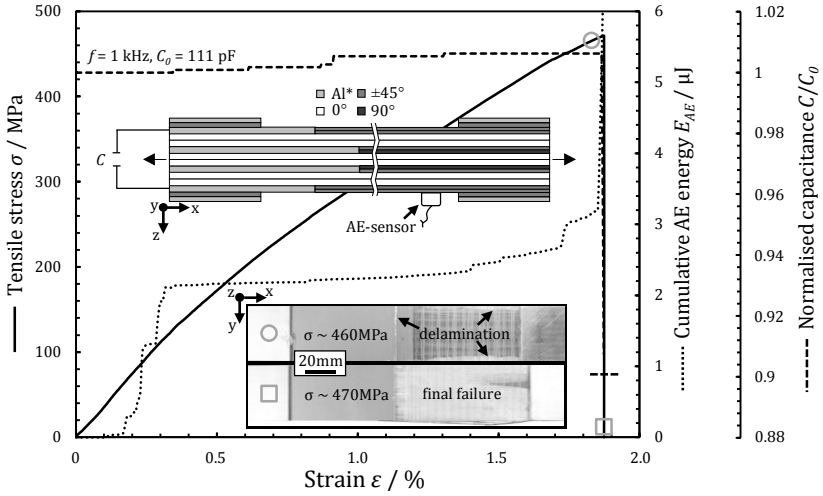

Figure 5.36: Tensile stress-strain response, corresponding cumulative AE energy and normalised capacitance of a representative GFRP specimen with stepped lap metal sheets under tension.

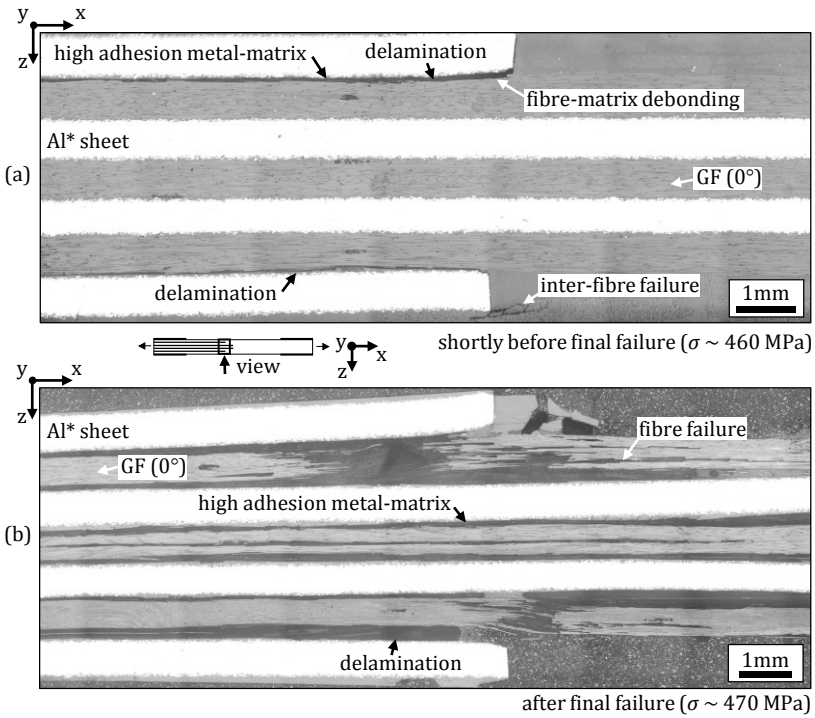

Figure 5.37: Optical microscopic edge view of representative GFRP specimen with stepped lap metal sheets under tension: (a) Shortly before final failure ($\sigma \sim 460$ MPa); (b) Final failure ($\sigma \sim 470$ MPa).

5.6.4 Low-velocity impact

The fracture pattern is obtained after the low-velocity impact as described in chapter 5.4.1. The capacitance measurement allows to estimate the approximate damage size after an impact (Figure 5.38). Delamination and IFFs cause the distance between the metal sheets to increase and the relative static permittivity (ε_r) to decrease, due to air in between the layers ($\varepsilon_{r,air} \approx 1$, $\varepsilon_{r,GFRP} \approx 5\text{-}8$), which reduces the total capacitance (~ 2 % on the non-impacted side, ~ 1.5 % in the mid plane, and ~ 0.9 % on the impacted side). These results correlate perfectly with the damage pattern obtained from the optical microscopic edge view.

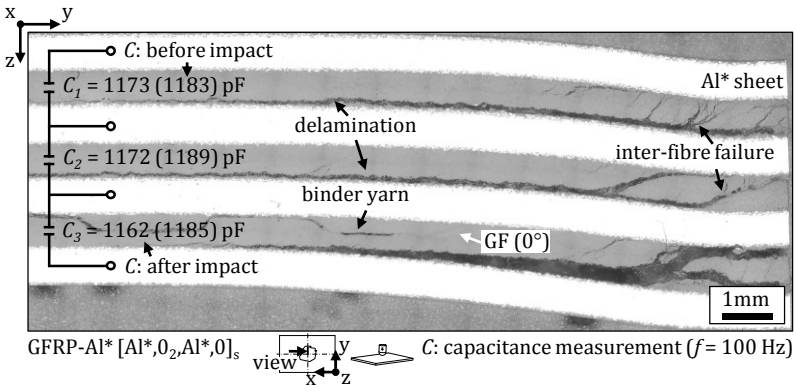

Figure 5.38: Optical microscopic edge view of a representative GFRP-Al* specimen under low-velocity impact loading considering capacitance measurment according to [40].

The slight differences in the measured capacitances C_1, C_2, C_3 between the three Al* sheets before impact is the sum of measuring deviations, manufacturing and material variations.

5.6.5 Compression after impact

Figure 5.39 depicts the compressive residual stress (σ^{CAI})-strain (ε^{CAI}) response, corresponding cumulative AE energy (E_{AE}) and normalised capacitance (C/C_0) of representative GFRP and GFRP-Al* specimens under CAI loading. The stress-strain responses are described in detail in chapter 5.4.2. As seen in Figure 5.39, the cumulative AE energy of the GFRP laminate increases rapidly (at about $\varepsilon^{CAI} \approx 1.1$ %) to $E_{AE} \approx 5089$ µJ (final failure) due to IFFs, fibre fractures, and delamination. The cumulative AE energy of the GFRP-Al* laminates increases slowly (at about $\varepsilon^{CAI} \approx 0.7$ %) as soon as the degradation begins. With further load increase the cumulative AE energy rises exponentially to $E_{AE} \approx 3105$ µJ (final failure) due to IFFs, fibre fractures, delamination, and plastic deformation of the metal sheets. The capacitance shows for both measurements, C_1 and C_3, significant increases during loading. As described in chapter 5.6.4, the metal sheets are slightly separated, and the relative static permittivity has changed after the impact (Figure 5.38).

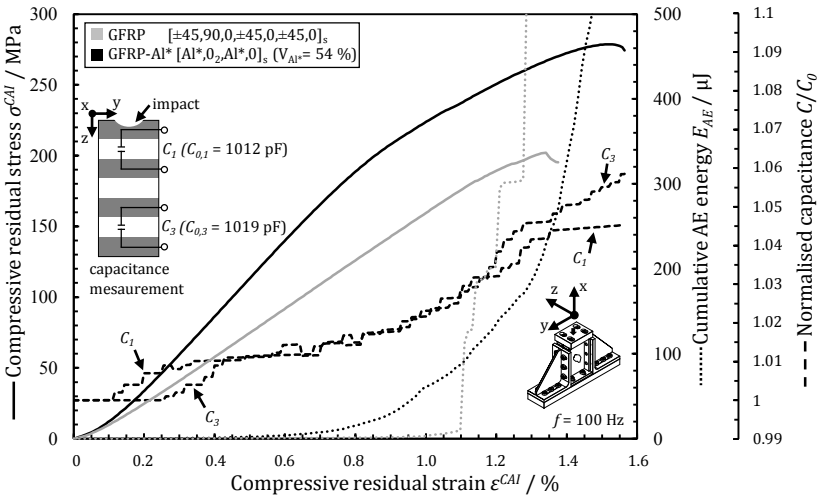

Figure 5.39: Compressive residual stress-strain response, corresponding cumulative AE energy and normalised capacitance of representative GFRP and GFRP-Al* specimens under CAI loading according to [40].

During CAI loading, the metal sheets are compressed again, which decreases the distance and increases the relative static permittivity resulting in an increase of the capacitance. After the sudden failure of the specimens and the resulting delamination, the copper wires are chipped, resulting in an interruption of the capacitance measurement. However, due to drastic delamination and failures of the FML (Chapter 5.4.2, Figure 5.18), it is expected that the capacitance will rapidly decrease after final failure.

5.6.6 Static pin-loaded bearing

The bearing stress (σ^{br})-strain (ε^{br}) response, corresponding cumulative AE energy (E_{AE}) and normalised capacitance (C/C_0) of a representative GFRP-Al_{p23} [Al_{p23},0_2,Al_{p23},0]$_s$ specimen with untreated stepped lap perforated Al_{p23} sheets under static pin-loaded bearing is shown in Figure 5.40. Due to the occurrence of different failure mechanism, such as kink-band formation of the 0°-GFs, delamination, and plastic deformation of the Al sheets, the cumulative AE energy increases rapidly and the capacitance

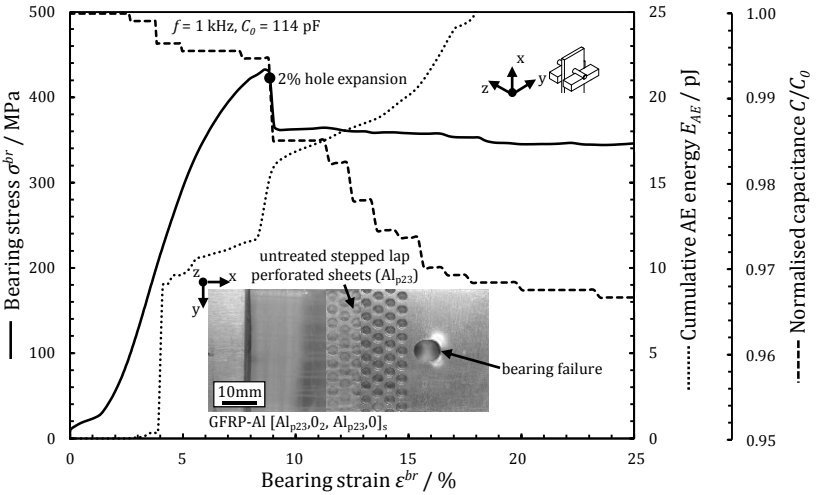

Figure 5.40: Bearing stress-strain response, corresponding cumulative AE energy and normalised capacitance of a representative GFRP-Al_{p23} specimen with untreated stepped lap perforated Al_{p23} sheets under static pin-loaded bearing.

decreases slightly (at about $\varepsilon^{CAI} \approx 4$ %). By reaching 2 % hole expansion (at about $\varepsilon^{CAI} \approx 9$ %) the cumulative AE energy increases to $E_{AE} \approx 15$ pJ. At this point the capacitance decrease rapidly mostly due to delamination, which changes the distance between the Al sheets as well as the relative static permittivity. With further load increase the cumulative AE energy rises to $E_{AE} \approx 490$ pJ at about $\varepsilon \approx 25$ %.

The optical microscopic edge view (Figure 5.41a) shows delamination between the Al sheets resulting in adhesive failure of the metal-matrix interface. This result indicates the extremely low interfacial bonding between the untreated Al sheets and matrix. After cut-out the microscopic sample the Al sheets are completely separated with a large distance to each other and therefore do not demonstrate a representative damage after the bearing loading. Static pin-loaded bearing tests with nanoscale sculptured Al* sheets lead to extremely small capacitance changes due to the low delamination within the FML (Figure 5.41b).

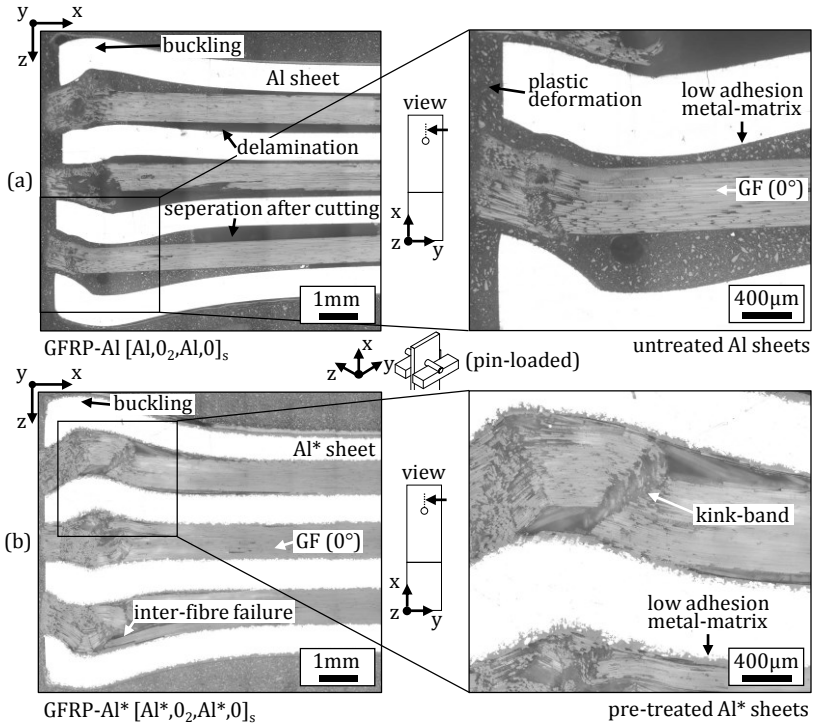

Figure 5.41: Optical microscopic edge view of representative specimens under static pin-loaded bearing: (a) FML with untreated Al sheets; (b) FML with pre-treated Al* sheets.

6 Conclusions

In this work, multifunctional fibre metal laminates to improve the mechanical performance and bolted joint fatigue lifetime compared to conventional GF reinforced polymers are being investigated. Furthermore, a new approach for in-situ health monitoring of FMLs is being examined. Different metal ply architectures with untreated as well as pre-treated surfaces including permeable metal plies, such as woven metallic fabrics and perforated ones, as well as solid metal sheets are characterised to obtain the most potential metal ply for structural applications. From the results obtained the following conclusions can be drawn.

The pre-treated metal sheets by nanoscale sculpturing demonstrate promising results for designing tough composites for structural applications. The FMLs show drastically increased mechanical performance compared to conventional GFRP laminates, achieving values for static pin-bearing up to 21 %, static bolt-bearing up to 2 %, resistance under fatigue pin-bearing up to 100 times, resistance under fatigue bolt-bearing up to 28 times and CAI up to 9 %.

The fracture surfaces of the nanoscale sculptured metal plies demonstrate high inter-laminar properties due to the three-dimensional mechanical interlocking surface structure, which is strong enough to withstand the normal and shear stresses in the interface during different loading conditions. The result is that delamination appears on the one hand at the GF-matrix interface due to the lower interfacial strength between the fibre and the matrix compared to the nanoscale sculptured Al*-matrix bond. On the other hand, delamination occurs due to cohesive matrix failure. This means that the inter-laminar properties of the FMLs are now entirely limited by the fibre-matrix bond of the base GFRP material and the matrix properties. Thus, without these limitations, the mechanical properties could be even higher.

Due to this high inter-laminar Al*-matrix bond it is expected that the stepped lap bonded hybridised zone of the surface structured Al* sheets-GFRP layers can be smaller reducing weight. Furthermore, it is expected that under fatigue bearing loading the edge and width distance to diameter ratios can be reduced as well.

The health monitoring methods demonstrate, that damages and their approximate size in the FMLs can be detected by standard capacitance measurements between the single Al plies, without the need of additional sensors. The capacitance significantly decreases due to damages between the metal plies. It can be seen that even small crack growth is detectable using this method. Hence, SHM of large structural components could be possible at low costs.

The permeable metal plies lead to the formation of matrix bridges (mechanical adhesion). These matrix bridges increase the resistance against delamination resulting in higher inter-laminar properties. In addition, the permeability of these metal plies allows the matrix flow through the thickness direction during the resin transfer moulding process, reducing the injection process time several minutes.

7 References

[1] Collings TA. The strength of bolted joints in multi-directional cfrp laminates. Composites. 1977; 8(1):43–55.

[2] Godwin EW, Matthews FL. A review of the strength of joints in fibre-reinforced plastics: Part 1. Mechanically fastened joints. Composites. 1980; 11(3):155–160.

[3] Caprino G, Squillace A, Giorleo G, Nele L, Rossi L. Pin and bolt bearing strength of fibreglass/aluminium laminates. Composites Part A: Applied Science and Manufacturing. 2005; 36(9):1307–1315.

[4] Slagter WJ. On the bearing strength of fibre metal laminates. Journal of composite materials. 1992; 26(17):2542–2566.

[5] Fink A, Camanho PP, Andrés JM, Pfeiffer E, Obst A. Hybrid CFRP/titanium bolted joints: Performance assessment and application to a spacecraft payload adaptor. Composites Science and Technology. 2010; 70(2):305–317.

[6] Wu G, Yang J. The mechanical behavior of GLARE laminates for aircraft structures. Jom. 2005; 57(1):72–79.

[7] Hirai Y, Hamada H, Kim J. Impact response of woven glass-fabric composites—I.: Effect of fibre surface treatment. Composites Science and Technology. 1998; 58(1):91–104.

[8] Vlot A. Low-velocity impact loading: on fibre reinforced aluminium laminates (ARALL and GLARE) and other aircraft sheet materials: Delft University of Technology; 1993.

[9] Sadighi M, Alderliesten RC, Benedictus R. Impact resistance of fiber-metal laminates: A review. International Journal of Impact Engineering. 2012; 49:77–90.

[10] Cantwell WJ, Morton J. The impact resistance of composite materials — a review. Composites. 1991; 22(5):347–362.

[11] Vogelesang L, Vlot A. Development of fibre metal laminates for advanced aerospace structures. Journal of Materials Processing Technology. 2000; 103(1):1–5.

[12] Schulte K, Baron C. Load and failure analyses of CFRP laminates by means of electrical resistivity measurements. Composites Science and Technology. 1989; 36(1):63–76.

[13] Ciang CC, Lee J, Bang H. Structural health monitoring for a wind turbine system: a review of damage detection methods. Measurement Science and Technology. 2008; 19(12):122001.

[14] Diamanti K, Soutis C. Structural health monitoring techniques for aircraft composite structures. Progress in Aerospace Sciences. 2010; 46(8):342–352.

[15] Kessler SS, Spearing SM, Soutis C. Damage detection in composite materials using Lamb wave methods. Smart Materials and Structures. 2002; 11(2):269.

[16] Majumder M, Gangopadhyay TK, Chakraborty AK, Dasgupta K, Bhattacharya DK. Fibre Bragg gratings in structural health monitoring—Present status and applications. Sensors and Actuators A: Physical. 2008; 147(1):150–164.

[17] Böger L, Wichmann MH, Meyer LO, Schulte K. Load and health monitoring in glass fibre reinforced composites with an electrically conductive nanocomposite epoxy matrix. Composites Science and Technology. 2008; 68(7–8):1886–1894.

[18] Schliekelmann RJ. Non-destructive testing of adhesive bonded metal-to-metal joints 1. Non-Destructive Testing. 1972; 5(2):79–86.

[19] Schliekelmann RJ. Non-destructive testing of adhesive bonded metal-to-metal joints 2. Non-Destructive Testing. 1972; 5(3):144–153.

[20] Kolesnikov B, Herbeck L, Fink A. CFRP/titanium hybrid material for improving composite bolted joints. Composite Structures. 2008; 83(4):368–380.

[21] Remmers JJC. Discontinuities in materials and structures: a unifying computational approach: TU Delft, Delft University of Technology; 2006.
[22] Fredell R, van Barneveld W, Vogelesang LB. Design and testing of bonded GLARE patches in the repair of fuselage fatigue cracks in large transport aircraft. International Journal of Fatigue. 1995; 3(17):230.
[23] Guo Y, Wu X. Bridging stress distribution in center-cracked fiber reinforced metal laminates: modeling and experiment. Engineering Fracture Mechanics. 1999; 63(2):147–163.
[24] Vlot A. Impact loading on fibre metal laminates. International Journal of Impact Engineering. 1996; 18(3):291–307.
[25] Chai GB, Manikandan P. Low velocity impact response of fibre-metal laminates – A review. Composite Structures. 2014; 107:363–381.
[26] Vlot A. Glare: history of the development of a new aircraft material: Springer Science & Business Media; 2001.
[27] Gagné M, Therriault D. Lightning strike protection of composites. Progress in Aerospace Sciences. 2014; 64(Supplement C):1–16.
[28] Both J, Wedekind M, Baier H. Simulation and experimental characterization of the bearing behavior of CFRP-metal laminates. 15th European Conference on Composite Materials (ECCM15). 2012.
[29] Ferrante L, Sarasini F, Tirillò J, Lampani L, Valente T, Gaudenzi P. Low velocity impact response of basalt-aluminium fibre metal laminates. Materials & Design. 2016; 98:98–107.
[30] Sharma AP, Khan SH, Kitey R, Parameswaran V. Effect of through thickness metal layer distribution on the low velocity impact response of fiber metal laminates. Polymer Testing. 2018; 65:301–312.
[31] Frizzell RM, McCarthy CT, McCarthy MA. An experimental investigation into the progression of damage in pin-loaded fibre metal laminates. Composites Part B: Engineering. 2008; 39(6):907–925.
[32] Yeh P, Chang P, Wang J, Yang J, Wu PH, Liu MC. Bearing strength of commingled boron/glass fiber reinforced aluminum laminates. Composite Structures. 2012; 94(11):3160–3173.
[33] Bosbach B, Liebig VW, Fiedler B. Characterisation of intrinsic hybrid-composites consisting of fibre-reinforced polymer and permeable metal plies. Workshop on Aircraft System Technologies (AST). 2015.
[34] Bosbach B, Liebig VW, Fiedler B. Bearing response of fibre metal laminates consisting of GFRP and woven metallic fabrics. 20th International Conference on Composite Materials (ICCM20. 2015.
[35] Bosbach B, Meeuw H, Fiedler B. Characterisation of fibre-metal-laminates under bearing loading. 17th European Conference on Composite Materials (ECCM17). 2016.
[36] Bosbach B, Stange D, Fiedler B. Interlaminar fracture toughness of fibre metal laminates. Workshop on Aircraft System Technologies (AST). 2017.
[37] Bosbach B, Ohle C, Fiedler B. Structural Health Monitoring of Multifunctional Fibre Metal Laminates under Mode I Loading. Structural Health Monitoring. 2017:1976–1983.
[38] Bosbach B, Ohle C, Fiedler B. Structural health monitoring of fibre metal laminates under mode I and II loading. Composites Part A: Applied Science and Manufacturing. 2018; 107:471–478.
[39] Bosbach B, Baytekin-Gerngross M, Heyden E, Gerngross MD, Carstensen J, Adelung R, Fiedler B. Reaching maximum inter-laminar properties in GFRP/nanoscale sculptured aluminium ply laminates. Composites Science and Technology. 2018; 167:32–41.
[40] Bosbach B, Baytekin-Gerngross M, Sprecher E, Wegner J, Gerngross MD, Carstensen J, Adelung R, Fiedler B. Maximizing bearing fatigue lifetime and CAI capability of fibre metal laminates by nanoscale sculptured Al plies. Composites Part A: Applied Science and Manufacturing. 2019; 117:144–155.
[41] Astrom BT. Manufacturing of polymer composites: CRC press; 1997.
[42] Schürmann H. Konstruieren mit Faser-Kunststoff-Verbunden: Springer-Verlag GmbH; 2005.

[43] Schulte K, Fiedler B. Structure and Properties of Composite Materials. 2nd ed. Hamburg: TUHH-TuTech Innovation GmbH; 2010.
[44] AVK – Industrievereinigung Verstärkte Kunststoffe e. V. Handbuch Faserverbundkunststoffe - Grundlagen, Verarbeitung, Anwendungen. 3rd ed.: Vieweg+Teubner; 2010.
[45] Bergmann W. Werkstofftechnik 1: Struktureller Aufbau von Werkstoffen-Metallische Werkstoffe-Polymerwerkstoffe-Nichtmetallisch-anorganische Werkstoffe: Carl Hanser Verlag GmbH & Co KG; 2013.
[46] Vlot A, Gunnink JW. Fibre metal laminates: an introduction: Kluwer Academic Publishers; 2011.
[47] Tjerk Johan dV. Blunt and sharp notch behaviour of Glare laminates: DUP Science; 2001.
[48] Weißbach W, Dahms M, Jaroschek C. Werkstoffkunde: Strukturen, Eigenschaften, Prüfung: Springer Science & Business Media; 2015.
[49] Roos E, Maile K, Seidenfuß M. Werkstoffkunde für Ingenieure: Grundlagen, Anwendung, Prüfung: Springer-Verlag GmbH; 2017.
[50] Seidel WW, Hahn F. Werkstofftechnik: Werkstoffe - Eigenschaften - Prüfung - Anwendung: Carl Hanser Verlag München; 2014.
[51] Liu Y, Liaw B. Effects of constituents and lay-up configuration on drop-weight tests of fiber-metal laminates. Applied Composite Materials. 2010; 17(1):43–62.
[52] Ehrenstein GW. Faserverbund-Kunststoffe: Werkstoffe, Verarbeitung, Eigenschaften: Carl Hanser Verlag GmbH & Co KG; 2006.
[53] Wu HF, Dwight DW, Huff NT. Effects of silane coupling agents on the interphase and performance of glass-fiber-reinforced polymer composites. 6th International Conference On Composite Interfaces. 1997; 57(8):975–983.
[54] Allaer K, Baere I de, Lava P, van Paepegem W, Degrieck J. On the in-plane mechanical properties of stainless steel fibre reinforced ductile composites. Composites Science and Technology. 2014; 100:34–43.
[55] Callens MG, Gorbatikh L, Bertels E, Goderis B, Smet M, Verpoest I. Tensile behaviour of stainless steel fibre/epoxy composites with modified adhesion. Composites Part A: Applied Science and Manufacturing. 2015; 69:208–218.
[56] Lunder O, Olsen B, Nisancioglu K. Pre-treatment of AA6060 aluminium alloy for adhesive bonding. International Journal of Adhesion and Adhesives. 2002; 22(2):143–150.
[57] Zhang X, Ma Q, Dai Y, Hu F, Liu G, Xu Z, Wei G, Xu T, Zeng Q, Xie W. Effects of surface treatments and bonding types on the interfacial behavior of fiber metal laminate based on magnesium alloy. Applied Surface Science. 2018; 427:897–906.
[58] Park SY, Choi WJ, Choi HS, Kwon H. Effects of surface pre-treatment and void content on GLARE laminate process characteristics. Journal of Materials Processing Technology. 2010; 210(8):1008–1016.
[59] Davis JR. Aluminum and aluminum alloys: ASM international; 1993.
[60] Venables JD. Adhesion and durability of metal-polymer bonds. Journal of Materials Science. 1984; 19(8):2431–2453.
[61] Goueffon Y, Arurault L, Mabru C, Tonon C, Guigue P. Black anodic coatings for space applications: Study of the process parameters, characteristics and mechanical properties. Journal of Materials Processing Technology. 2009; 209(11):5145–5151.
[62] Critchlow GW, Brewis DM. Review of surface pretreatments for aluminium alloys. International Journal of Adhesion and Adhesives. 1996; 16(4):255–275.
[63] Puck A. Festigkeitsanalyse von Faser-Matrix-Laminaten: Modelle für die Praxis: Carl Hanser Verlag München; 1996.
[64] Greszczuk LB. On failure modes of unidirectional composites under compressive loading: Fracture of Composite Materials; 1982.

[65] Jenckel E, Rumbach B. Über die Adsorption von hochmolekularen Stoffen aus der Lösung. Berichte der Bunsengesellschaft für physikalische Chemie. 1951; 55(7):612–618.
[66] Habenicht G. Kleben: Grundlagen,Technologien, Anwendungen. 6th ed.: Springer Science & Business Media; 2009.
[67] Li M, Matsuyama R, Sakai M. Interlaminar shear strength of C/C-composites: the dependence on test methods. Carbon. 1999; 37(11):1749–1757.
[68] ASTM D2344-00. Standard Test Method for Short-Beam Strength of Polymer Matrix Composite Materials and Their Laminates. ASTM International. 2000.
[69] ASTM D3846-08. Standard Test Method for In-Plane Shear Strength of Reinforced Plastics. ASTM International. 2008.
[70] Chiao CC, Moore RL, Chiao TT. Measurement of shear properties of fibre composites. Composites. 1977; 8(3):161–169.
[71] Shokrieh MM, Lessard LB. An assessment of the double-notch shear test for interlaminar shear characterization of a unidirectional graphite/epoxy under static and fatigue loading. Applied Composite Materials. 1998; 5(5):289–304.
[72] Sørensen BF, Jacobsen TK. Large-scale bridging in composites: R-curves and bridging laws. Composites Part A: Applied Science and Manufacturing. 1998; 29(11):1443–1451.
[73] Jacobsen TK, Sørensen BF. Mode I intra-laminar crack growth in composites — modelling of R-curves from measured bridging laws. Composites Part A: Applied Science and Manufacturing. 2001; 32(1):1–11.
[74] Shokrieh MM, Heidari-Rarani M. Effect of stacking sequence on R-curve behavior of glass/epoxy DCB laminates with 0°//0° crack interface. Materials Science and Engineering: A. 2011; 529:265–269.
[75] Shokrieh MM, Heidari-Rarani M, Ayatollahi MR. Delamination R-curve as a material property of unidirectional glass/epoxy composites. Materials & Design. 2012; 34:211–218.
[76] Andersons J, König M. Dependence of fracture toughness of composite laminates on interface ply orientations and delamination growth direction. Composites Science and Technology. 2004; 64(13–14):2139–2152.
[77] Sebaey TA, Blanco N, Costa J, Lopes CS. Characterization of crack propagation in mode I delamination of multidirectional CFRP laminates. Composites Science and Technology. 2012; 72(11):1251–1256.
[78] Kim BW, Mayer AH. Influence of fiber direction and mixed-mode ratio on delamination fracture toughness of carbon/epoxy laminates. Composites Science and Technology. 2003; 63(5):695–713.
[79] Nicholls DJ, Gallagher JP. Determination of GIC in angle-ply composites using cantilever beam test method. Reinforced Plastics and Composites. 1983(2).
[80] Robinson P, Song DQ. A modified DCB specimen for mode I testing of multidirectional laminates. Composite Material. 1992(26):1554–1577.
[81] Suo Z, Bao G, Fan B. Delamination R-curve phenomena due to damage. Journal of the Mechanics and Physics of Solids. 1992; 40(1):1–16.
[82] Anderson TL. Fracture mechanics: fundamentals and applications: CRC press; 2005.
[83] Hutchinson JW, Suo Z. Mixed mode cracking in layered materials. Advances in applied mechanics. 1991; 29:63–191.
[84] Mollón V, Bonhomme J, Viña J, Argüelles A. Theoretical and experimental analysis of carbon epoxy asymmetric dcb specimens to characterize mixed mode fracture toughness. Polymer Testing. 2010; 29(6):766–770.
[85] Ducept F, Gamby D, Davies P. A mixed-mode failure criterion derived from tests on symmetric and asymmetric specimens. Composites Science and Technology. 1999; 59(4):609–619.
[86] Valvo PS. On the calculation of energy release rate and mode mixity in delaminated laminated beams. Engineering Fracture Mechanics. 2016; 165(Supplement C):114–139.

[87] Bieniaś J, Dadej K, Surowska B. Interlaminar fracture toughness of glass and carbon reinforced multidirectional fiber metal laminates. Engineering Fracture Mechanics. 2017; 175(Supplement C):127–145.
[88] ASTM D7905-14. Standard Test Method for Determination of the Mode II Interlaminar Fracture Toughness of Unidirectional Fiber-Reinforced Polymer Matrix Composites. ASTM International. 2014.
[89] Nairn JA. Energy release rate analysis for adhesive and laminate double cantilever beam specimens emphasizing the effect of residual stresses. International Journal of Adhesion and Adhesives. 2000; 20(1):59–70.
[90] ASTM D5961-13. Standard Test Method for Bearing Response of Polymer Matrix Composte Laminates. ASTM International. 2013.
[91] Jarfall LE. Optimum design of joints: the stress severity factor concept: Elsevier; 1972.
[92] Kraft H, Schelling H. Statische Festigkeitsversuche an zweischnittigen gebolzten Fügungen aus CFK zur Ermittlung der Lochleibungsfestigkeit: DGLR-Bericht; 1984.
[93] Kiral BG. Effect of the clearance and interference-fit on failure of the pin-loaded composites. Materials & Design. 2010; 31(1):85–93.
[94] Cooper C, Turvey GJ. Effects of joint geometry and bolt torque on the structural performance of single bolt tension joints in pultruded GRP sheet material. Eighth International Conference on Composite Structures. 1995; 32(1):217–226.
[95] Wu HF, Slagter WJ. Parametric studies of bearing strength for fiber/metal laminates. Journal of aircraft. 1994; 31(4):936–945.
[96] Kretsis G, Matthews FL. The strength of bolted joints in glass fibre/epoxy laminates. Composites. 1985; 16(2):92–102.
[97] Stockdale JH, Matthews FL. The effect of clamping pressure on bolt bearing loads in glass fibre-reinforced plastics. Composites. 1976; 7(1):34–38.
[98] Irisarri F, Vandellos T, Paulmier P, Laurin F. Experiments and modeling of clamping effects on the the bearing strength of mechanically fastened joint in CFRP laminates. 16th European Conference on Composite Materials (ECCM16). 2014.
[99] Kingston-Lee DM, Rogers KF. A preliminary evaluation of proprietory rivets as fasteners for carbon fibre laminates'. RAE Technical Memorandum Materials. 1976; 243.
[100] Feo L, Marra G, Mosallam AS. Stress analysis of multi-bolted joints for FRP pultruded composite structures. Composite Structures. 2012; 94(12):3769–3780.
[101] Tagliaferri V, Caprino G, Diterlizzi A. Effect of drilling parameters on the finish and mechanical properties of GFRP composites. International Journal of Machine Tools and Manufacture. 1990; 30(1):77–84.
[102] Kavad BV, Pandey AB, Tadavi MV, Jakharia HC. A Review Paper on Effects of Drilling on Glass Fiber Reinforced Plastic. 2nd International Conference on Innovations in Automation and Mechatronics Engineering. 2014; 14:457–464.
[103] Caprino G, Tagliaferri V. Damage development in drilling glass fibre reinforced plastics. International Journal of Machine Tools and Manufacture. 1995; 35(6):817–829.
[104] Merino-Pérez JL, Royer R, Merson E, Lockwood A, Ayvar-Soberanis S, Marshall MB. Influence of workpiece constituents and cutting speed on the cutting forces developed in the conventional drilling of CFRP composites. Composite Structures. 2016; 140:621–629.
[105] Khashaba UA, El-Sonbaty IA, Selmy AI, Megahed AA. Machinability analysis in drilling woven GFR/epoxy composites: Part I – Effect of machining parameters. Composites Part A: Applied Science and Manufacturing. 2010; 41(3):391–400.
[106] Khashaba UA, El-Keran AA. Drilling analysis of thin woven glass-fiber reinforced epoxy composites. Journal of Materials Processing Technology. 2017; 249:415–425.

[107] Tsao CC, Hocheng H, Chen YC. Delamination reduction in drilling composite materials by active backup force. CIRP Annals. 2012; 61(1):91–94.
[108] Stone R, Krishnamurthy K. A neural network thrust force controller to minimize delamination during drilling of graphite-epoxy laminates. International Journal of Machine Tools and Manufacture. 1996; 36(9):985–1003.
[109] Paulo Davim J, Reis P, Conceição António C. Drilling fiber reinforced plastics (FRPs) manufactured by hand lay-up: influence of matrix (Viapal VUP 9731 and ATLAC 382-05). Proceedings of the International Conference on Advances in Materials and Processing Technologies: Part 2. 2004; 155-156:1828–1833.
[110] Hollmann K. Failure analysis of bolted composite joints exhibiting in-plane failure modes. Journal of composite materials. 1996; 30(3):358–383.
[111] Camanho PP, Fink A, Obst A, Pimenta S. Hybrid titanium–CFRP laminates for high-performance bolted joints. Special Issue: CompTest 2008. 2009; 40(12):1826–1837.
[112] Matsuzaki R, Shibata M, Todoroki A. Improving performance of GFRP/aluminum single lap joints using bolted/co-cured hybrid method. Composites Part A: Applied Science and Manufacturing. 2008; 39(2):154–163.
[113] Both JC. Tragfähigkeit von CFK-Metall-Laminaten unter mechanischer und thermischer Belastung. Technische Universität München. Lehrstuhl für Leichtbau. 2014.
[114] Kelly G. Quasi-static strength and fatigue life of hybrid (bonded/bolted) composite single-lap joints. Composite Structures. 2006; 72(1):119–129.
[115] Grosse CU, Ohtsu M. Acoustic emission testing: Springer Science & Business Media; 2008.
[116] Gungor S, Bakis CE. Indentation damage detection in glass/epoxy composite laminates with electrically tailored conductive nanofiller. Journal of Intelligent Material Systems and Structures. 2016; 27(5):679–688.
[117] Todoroki A, Kobayashi H, Matuura K. Application of electric potential method to smart composite structures for detecting delamination. JSME international journal. Ser. A, Mechanics and material engineering. 1995; 38(4):524–530.
[118] Peairs DM, Park G, Inman DJ. Improving accessibility of the impedance-based structural health monitoring method. Journal of Intelligent Material Systems and Structures. 2004; 15(2):129–139.
[119] Todoroki A, Miyatani S, Shimamura Y. Wireless strain monitoring using electrical capacitance change of tire: part I—with oscillating circuit. Smart Materials and Structures. 2003; 12(3):403.
[120] Baytekin-Gerngross M, Gerngross MD, Carstensen J, Adelung R. Making metal surfaces strong, resistant, and multifunctional by nanoscale-sculpturing. Nanoscale Horizons. 2016; 1(6):467–472.
[121] Gerngross MD, Baytekin-Gerngross M, Carstensen J, Adelung R. Self-Organized Growth of Crystallographic Macropores in Multicrystalline Zn by Nanoscale Sculpturing. Journal of The Electrochemical Society. 2018; 165(4):H3099-H3106.
[122] ASTM D5528-02. Standard Test Method for Mode I Interlaminar Fracture Toughness of Unidirectional Fiber-Reinforced Polymer Matrix Composites. ASTM International. 2002.
[123] ASTM D3039-00. Standard Test method for Tensile Properties of Polymer Matrix Composite Materials. ASTM International. 2000.
[124] ASTM D3410-03. Standard Test Method forCompressive Properties of Polymer Matrix Composite Materials with Unsupported Gage Section by Shear Loading. ASTM International. 2003.
[125] DIN EN ISO 6892-1. Metallische Werkstoffe – Zugversuch – Teil 1: Prüfverfahren bei Raumtemperatur2016.
[126] ASTM D7136-05. Standard Test Method for Measuring the Damage Resistance of a Fiber-Reinforced Polymer Matrix Composite to a Drop-Weight Impact Event. ASTM International. 2005.
[127] ASTM D7137-05. Standard Test Method for Compressive Residual Strength Properties of Damaged Polymer Matrix Composite Plates. ASTM International. 2005.

[128] ASTM D3479-96. Standard Test Method for Tension-Tension Fatigue of Polymer Matrix Composite Materials. ASTM International. 2002.
[129] Postec M, Deletombe E, Delsart D, Coutellier D. Study of the influence of the number of inter-ply interfaces on the bearing rupture of riveted composite assemblies. Composite Structures. 2008; 84(2):99–113.
[130] Greenhalgh E. Failure analysis and fractography of polymer composites: Elsevier; 2009.
[131] Purslow D. Some fundamental aspects of composites fractography. Composites. 1981; 12(4):241–247.
[132] Greenhalgh ES. Characterisation of mixed-mode delamination growth in carbon-fibre composites: Imperial College London (University of London); 1998.
[133] Purslow D. Matrix fractography of fibre-reinforced epoxy composites. Composites. 1986; 17(4):289–303.
[134] Yokozeki T, Ogasawara T, Aoki T. Correction method for evaluation of interfacial fracture toughness of DCB, ENF and MMB specimens with residual thermal stresses. Composites Science and Technology. 2008; 68(3):760–767.
[135] Liebig WV, Leopold C, Hobbiebrunken T, Fiedler B. New test approach to determine the transverse tensile strength of CFRP with regard to the size effect. Composites Communications. 2016; 1:54–59.
[136] Luftfahrttechnisches Handbuch. Handbuch Strukturberechnung (HSB): herausgegeben vom Industrieausschuss Strukturberechnungsunterlagen (IASB).
[137] Macherauch E, Zoch H. Praktikum in Werkstoffkunde: 91 ausführliche Versuche aus wichtigen Gebieten der Werkstofftechnik: Springer-Verlag GmbH; 2011.
[138] Lee J, Soutis C. A study on the compressive strength of thick carbon fibre–epoxy laminates. Composites Science and Technology. 2007; 67(10):2015–2026.

Supervised student theses and research projects

Eike Sprecher. Numerische und Experimentelle Untersuchung von Bolzenverbindungen bei hybriden Verbundwerkstoffen.Master thesis. Hamburg University of Technology. 2018.

Johann Wegner. Experimentelle Betrachtung von faserverstärkten Hybridlaminaten mit integrierten Metallschichten auf die Restdruckfestigkeit nach einem Schlagschaden. Research project. Hamburg University of Technology. 2018.

Eike. Sprecher. Detektion und Analyse des Versagensverhaltens von Faser-Metall-Laminaten unter Lochleibung. Research project. Hamburg University of Technology. 2017.

Batur Heidari. Implementierung eines tri-linearen Kohäsivzonenmodells zur Untersuchung des Delaminationsverhaltens von Faser-Metall-Laminaten in einer FEM-Simulation. Research project. Hamburg University of Technology. 2017.

Emil Heyden. Numerische Simulation des inter- und intralaminaren Versagens eines faserverstärkten Hybrid-Laminates während eines Impacts. Master thesis. Hamburg University of Technology. 2017.

Ole Lippke. Experimentelle Untersuchung glasfaserverstärkter Kunststoffe und Metalllagen unter Zug-, Druck- und Schubbelastung. Bachelor thesis. Hamburg University of Technology. 2017.

Christoph Ohle. Detektion und Analyse von Delamination in Hybridverbunden bestehend aus faserverstärkten Kunststoffen und Metallschichten. Bachelor thesis. Hamburg University of Technology. 2017.

Josef Koord. Numerische Betrachtung der interlaminaren Bruchzähigkeit von Faser-Metall-Laminaten. Master thesis. Hamburg University of Technology. 2016.

Henrik Werner. Numerische Betrachtung der Tragfähigkeit von Faser-Metall-Laminaten in Hinblick auf deren Lochleibungseigenschaften. Master thesis. Hamburg University of Technology. 2016.

Eike Sprecher. Untersuchung der interlaminaren Scherfestigkeit von faserverstärkten Hybridlaminaten mit permeablen Metallschichten. Bachelor thesis. Hamburg University of Technology. 2016.

Tobias Müller. Charakterisierung von Faser-Metall-Laminaten aus faser-verstärktem Kunststoff und permeablen Metalleinlegern. Master thesis. Hamburg University of Technology. 2016.

Hendrik Beecken. Charakterisierung von intrinsischen Hybridverbunden aus faserverstärkten Kunststoffen und Metallschichten unter Lochleibung. Bachelor thesis. Hamburg University of Technology. 2016.

Emil Heyden. Untersuchung der interlaminaren Scherfestigkeit von faserverstärkten Hybridlaminaten mit integrierten Metallschichten. Research project. Hamburg University of Technology. 2016.

Danny Stange. Betrachtung der Energiefreisetzungsraten in Mode I und II und den damit verbundenen Schadensmechanismen von Faser-Metall-Laminaten. Bachelor thesis. Hamburg University of Technology. 2015.

Marcel Heller. Betrachtung des Verhaltens hybrider Faser-Metall-Laminate im Hinblick auf deren Lochleibungseigenschaften. Master thesis. Hamburg University of Technology. 2015.

Mathias Koch. Untersuchung der Energiefreisetzungsraten G_{IC} und G_{IIC} von faserverstärkten Hybridlaminaten mit integrierten Metallschichten. Research project. Hamburg University of Technology. 2015.

Hauke Meeuw. Evaluierung von neuartigen Hybridverbunden in Hinblick auf deren Lochleibungseigenschaften. Master thesis. Hamburg University of Technology. 2015.

Publications

Bosbach B, Baytekin-Gerngross M, Sprecher E, Wegner J, Gerngross MD, Carstensen J, Adelung R, Fiedler B. Maximizing bearing fatigue lifetime and CAI capability of fibre metal laminates by nanoscale sculptured Al plies. Composites Part A: Applied Science and Manufacturing. 2019; 117:144–155.

Bosbach B, Baytekin-Gerngross M, Heyden E, Gerngross MD, Carstensen J, Adelung R, Fiedler B. Reaching maximum inter-laminar properties in GFRP/nanoscale sculptured aluminium ply laminates. Composites Science and Technology. 2018; 167:32–41.

Bosbach B, Ohle C, Fiedler B. Structural health monitoring of fibre metal laminates under mode I and II loading. Composites Part A: Applied Science and Manufacturing. 2018; 107:471–478.